Components and Circuits for Tunneling Diode based High Frequency Sources

Afesomeh Ofiare

School of Engineering

University of Glasgow

A thesis submitted in fulfilment of the requirements for the degree of

Doctor of Philosophy

January 2016

This thesis is dedicated to Ogbaji Ofiare, Ruth Ofiare and Wendy Smith

Acknowledgements

First, I would like to express gratitude to my supervisor, Dr. Edward Wasige, for offering me the opportunity to do this research and for his advice and guidance throughout the course of my PhD. I would also like to thank him for his inexhaustible patience through the difficult and challenging times during my research.

I would also like to thank Dr. Ata Khalid and Dr. Jue Wang. Their experiences, advice, ideas and help with fabrication and measurements were invaluable and helped greatly towards the completion of my research. Also thanks to my colleague Khalid Alharbi for his help with fabrication of the antennas characterised in this thesis and support.

I wish to thank all the technical staff in the Electronics and Nanoscale Engineering division, in particular Tom O'Hara, Allan Yuill and Peter McKenna for all their help and assistance. Also thanks to all the staff in the IT support for their help along the way.

I would also like to thank my colleagues and office mates: Salah Sharabi, Raphael Brown, Monageng Kgwadi, Clement Vourch, Francesco Mirando, Ivonne Carannza, Lourdes Ferre Llin, etc, for sharing the experiences of doing a PhD.

Lastly, I wish to especially thank my parents Ogbaji and Ruth Ofiare, my siblings and friends for their consistent support.

Abstract

Terahertz (THz) technology has been generating a lot of interest because of the potential applications for systems working in this frequency range. However, to fully achieve this potential, effective and efficient ways of generating controlled signals in the terahertz range are required. Devices that exhibit negative differential resistance (NDR) in a region of their current-voltage $(I - V)$ characteristics have been used in circuits for the generation of radio frequency signals. Of all of these NDR devices, resonant tunneling diode (RTD) oscillators, with their ability to oscillate in the THz range are considered as one of the most promising solid-state sources for terahertz signal generation at room temperature. There are however limitations and challenges with these devices, from inherent low output power usually in the range of micro-watts (μW) for RTD oscillators when milli-watts (mW) are desired. At device level, parasitic oscillations caused by the biasing line inductances when the device is biased in the NDR region prevent accurate device characterisation, which in turn prevents device modelling for computer simulations.

This thesis describes work on $I - V$ characterisation of tunnel diode (TD) and RTD (fabricated by Dr. Jue Wang) devices, and the radio frequency (RF) characterisation and small signal modelling of RTDs. The thesis also describes the design and measurement of hybrid TD

oscillators for higher output power and the design and measurement of a planar Yagi antenna (fabricated by Khalid Alharbi) for THz applications.

To enable oscillation free current-voltage characterisation of tunnel diodes, a commonly employed method is the use of a suitable resistor connected across the device to make the total differential resistance in the NDR region positive. However, this approach is not without problems as the value of the resistor has to satisfy certain conditions or else bias oscillations would still be present in the NDR region of the measured $I - V$ characteristics. This method is difficult to use for RTDs which are fabricated on wafer due to the discrepancies in designed and actual resistance values of fabricated resistors using thin film technology. In this work, using pulsed DC rather than static DC measurements during device characterisation were shown to give accurate characteristics in the NDR region without the need for a stabilisation resistor. This approach allows for direct oscillation free characterisation for devices. Experimental results show that the $I - V$ characterisation of tunnel diodes and RTD devices free of bias oscillations in the NDR region can be made.

In this work, a new power-combining topology to address the limitations of low output power of TD and RTD oscillators is presented. The design employs the use of two oscillators biased separately, but with the combined output power from both collected at a single load. Compared to previous approcahes, this method keeps the frequency of oscillation of the combined oscillators the same as for one of the oscillators. Experimental results with a hybrid circuit using two tun-

nel diode oscillators compared with a single oscillator design with similar values shows that the coupled oscillators produce double the output RF power of the single oscillator. This topology can be scaled for higher (up to terahertz) frequencies in the future by using RTD oscillators.

Finally, a broadband Yagi antenna suitable for wireless communication at terahertz frequencies is presented in this thesis. The return loss of the antenna showed that the bandwidth is larger than the measured range (140-220 GHz). A new method was used to characterise the radiation pattern of the antenna in the $E-$plane. This was carried out on-wafer and the measured radiation pattern showed good agreement with the simulated pattern.

In summary, this work makes important contributions to the accurate characterisation and modelling of TDs and RTDs, circuit-based techniques for power combining of high frequency TD or RTD oscillators, and to antennas suitable for on chip integration with high frequency oscillators.

Publications

[1] **A. Ofiare**, J. Wang, K. Alharbi, A. Khalid, E. Wasige and L. Wang, "Novel Tunnel Diode Oscillator Power Combining Circuit Topology based on Synchronisation," *Asia Pacific Microwave Conference (APMC)*, December 2015.

[2] **A. Ofiare**, A. Khalid, J. Wang and E. Wasige, "Pulsed I-V and Small Signal Characterisation and Modelling of Resonant Tunneling Diodes," *IEEE PhD Research in Microelectronics and Electronics (PRIME) Conference*, 29 June - 2 July 2015.

[3] **A. Ofiare**, R. Brown, K. Alharbi, J. Wang, A. Khalid, D. Cumming and E. Wasige, "Accurate Pulsed I-V Measurement of the NDR Region of Tunnel Diodes and Resonant Tunneling Diodes," *UK Semiconductor Conference*, Sheffield Hallam University, July 2015.

[4] **A. Ofiare**, K. Alharbi, J. Wang, A. Khalid, D. Cumming and E. Wasige, "Wideband Planar Yagi Antenna for Millimetre-Wave Frequency Applications" *7th European/UK-China Workshop on Millimeter Waves and Terahertz Technologies (UCMMT)*, October 2014.

[5] J. Wang, K. Alharbi, **A. Ofiare**, H. Zhou, A. Khalid, D. Cumming and E. Wasige, "High Performance Resonant Tunneling Diode Oscillators for THz applications," *IEEE Compound Semiconductor IC Symposium*, USA, October 2015.

[6] K. Alharbi, **A. Ofiare**, J. Wang, M. Kgwadi, A. Khalid, D. Cumming and E. Wasige, "Broadband Slotted Bow-tie Antennas for Terahertz Resonant Tunnelling Diode Based Oscillators," *Progress in Electromagnetics Research Symposium*, pp. 1847-1852, 6-9 July 2015.

[7] K. Alharbi, **A. Ofiare**, J. Wang, M. Kgwadi, A. Khalid, D. Cumming and E. Wasige, "On-wafer 2D Characterization Technique for Quasi-Yagi Antenna for G-band Applications," *Progress in Electromagnetics Research Symposium*, 6-9 July 2015.

[8] J. Wang, K. Alharbi, **A. Ofiare**, R. Brown, A. Khalid, D. Cumming and E. Wasige, "D-band Resonant Tunnelling Diode Oscillator with High Output Power," *UK Semiconductor Conference*, Sheffield Hallam University, July 2015.

[9] J. Wang, **A. Ofiare**, K. Alharbi, R. Brown, A. Khalid, D. Cumming and E. Wasige "MMIC Resonant Tunneling Diode Oscillators for THz applications," *IEEE PhD Research in Microelectronics and Electronics (PRIME) Conference*, 29 June - 2 July 2015.

[10] K. Alharbi, **A. Ofiare**, J. Wang, A. Khalid, D. Cumming and E. Wasige, "Radiation pattern characterisation setup for G-band planar Yagi antennas," *2nd IET Annual Seminar in Active and Passive RF Devices*, pp.1-3, 29 October 2014.

Contents

List of Figures

List of Tables

List of Acronyms, Symbols and Constants

Acronyms

AC Alternating Current

ADS Advanced Design System

AUT Antenna Under Test

BWO Backward Wave Oscillator

CMOS Complementary Metal Oxide Semiconductor

CPW Co-planar Waveguide

DBQW Double Barrier Quantum Well

DC Direct Current

DUT Device Under Test

FIR Far Infrared

GSG Ground-Signal-Ground

HBT Heterojunction Bipolar Transistor

HEMT High Electron Mobility Transistor

HFSS High Frequency Structural Simulator

IF Intermediate Frequency

IMPATT Impact Ionisation Transit Time

LO Local Oscillator

MBE Molecular Beam Epitaxy

NDR Negative Differential Resistance

PDR Positive Differential Resistance

PMMA Polymethyl Methacrylate

PVCR Peak-to-Valley Current Ratio

QCL Quantum Cascade Laser

RF Radio Frequency

RSU Remote Sensing Unit

RTD Resonant Tunneling Diode

SIS Superconductor Insulating Superconductor

SMA Sub Miniature Version A

SOLT Short-Open-Load-Thru

TD Tunnel Diode

TED Transfer Electron Device

THz Terahertz

TUNNET Tunnel Injection Transit Time

VNA Vector Network Analyser

WGFMU Waveform Generator/Fast Measurement Unit

Symbols

ϵ_r Dielectric constant

ΔE_c Conduction band offset

E_g Band gap

f_{max} Unity power cut-off frequency

f_T Unity current gain cut-off frequency

J Current density

m^* Electron effective mass

λ Wavelength

Constants

$c = 3 \times 10^8 m/s$ Velocity of light in free space

$e = 1.60 \times 10^{-19} C$ Elementary charge

$h = 4.136 \times 10^{-15} eVs$ Planck's constant

$\hbar = 6.582 \times 10^{16} eVs$ Reduced Planck's constant

$\kappa = 8.617 \times 10^5 eV/K$ Boltzmann constant

$m_0 = 9.11 \times 10^{-31} kg$ Electron rest mass

Chemical Symbols

Al Aluminium

AlAs Aluminium Arsenide

AlSb Aluminium Antimonide

As Arsenic

Ga Gallium

GaAs Gallium Arsenide

Ge Germanium

In Indium

InAs Indium Arsenide

InAlAs Indium Aluminium Arsenide

InGaAs Indium Gallium Arsenide

InP Indium Phosphide

P Phosphorus

Si Silicon

SiGe Silicon Germanium

Chapter 1

Introduction

1.1 Introduction

Terahertz Radiation

Electromagnetic waves at frequencies from 300 Gigahertz (GHz) up to 3 Terahertz (THz), having wavelengths, λ, between 1 mm and 100 μm are usually referred to as terahertz radiation. This definition places the THz frequency band between the edge of the millimetre-wave frequency band and the infrared frequency range which is in the optical domain as seen in the diagram of the electromagnetic spectrum shown in Figure 1.1 [1].

Terahertz emissions occur in the universe mainly from black body radiations from anything with temperature greater than 10 Kelvin (K) with wavelengths below 1 mm [1] [2]. Some of the earliest uses of the term terahertz were by spectroscopy enthusiasts to describe the electromagnetic emissions that were below the frequencies and wavelengths of the far infrared [3] [4]. Until recently, THz radiation has mainly been used for high-resolution spectroscopy and remote sensing by
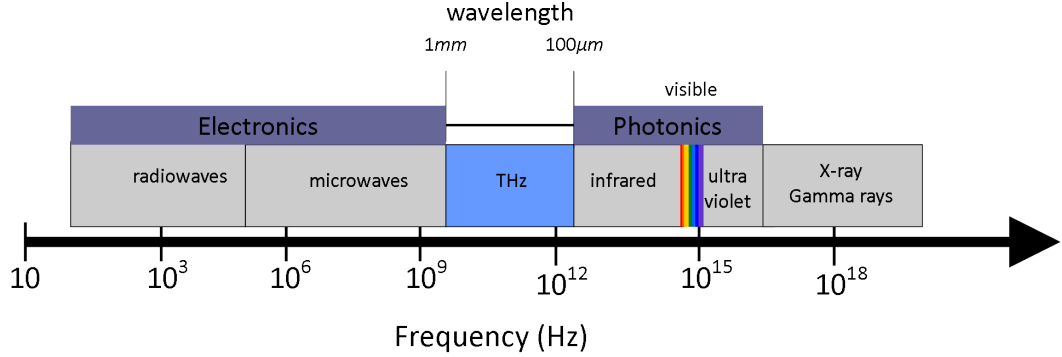
Figure 1.1: *Electromagnetic spectrum showing terahertz wavelength and frequency range between radio frequency range and infrared spectrum.*

astronomers and planetary scientists to map thermal emissions in planetary atmospheres [1]. The photon energy of THz radiation can be calculated from the relationship between the energy of the photon and the inverse of its wavelength using Equation 1.1.

$$E = \frac{hc}{\lambda} \tag{1.1}$$

where h is Planks constant, c is the speed of light and λ is the wavelength of the radiation. For the frequencies range 300 GHz - 3 THz [1][2] having wavelength range between 1 mm - 100 μm, the corresponding photon energy level is from 1.2 meV - 12.4 meV. This makes THz signals in this range non-ionising as they do not contain the amount of energy needed to displace an electron from an atom or molecule. Although the effect of exposure to THz radiation has not been studied, guidelines to exposure are covered under the IEEE safety standards [4]. The non-ionizing photon energy levels in the THz range seemingly make it a lot safer than X-rays and its uses are widely studied in the medical and scientific community [5][6].

Terahertz radiation has been observed to be easily absorbed by water[1][3]. The earth's atmosphere due to the presence of water vapour absorbs THz radiation. This makes THz signals unsuitable for long distance transmission. The absorption rate is seen to peak between 1 THz and 10 THz as can be seen in Figure 1.2 [3].
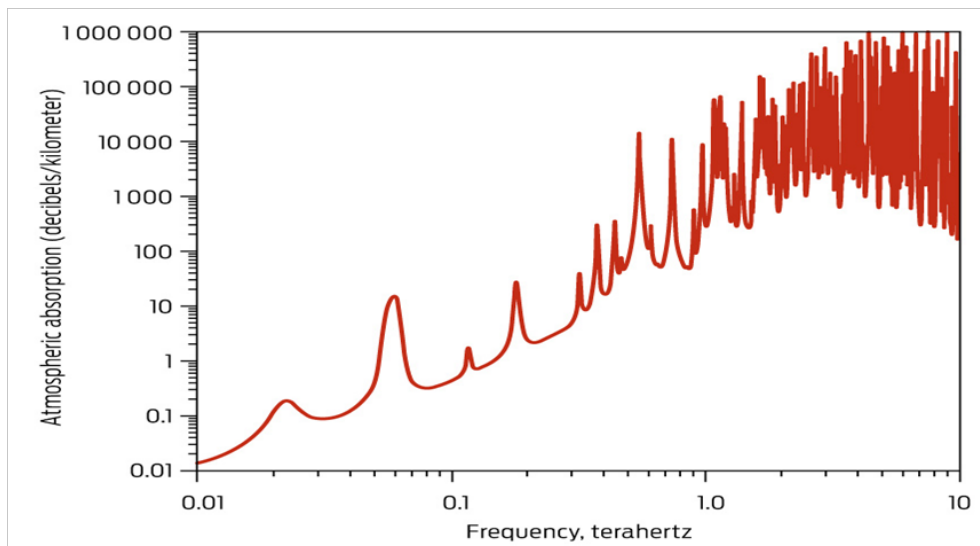
Figure 1.2: *Atmospheric absorption of THz signals [3].*

Knowing the absorption rate of THz signals by water coupled with the non-ionising property of THz radiation and its ability to penetrate through some materials such as paper, clothing and cardboard makes it of great interest to the scientific and medical research community [6]. These properties would allow THz radiation to be used for non-invasive security screening, scientific imaging, quality control and medical imaging. The THz frequencies are also suitable for high data rate short distance wireless communication. Since THz radiation cannot penetrate water, its use for deep detection inside the human body is limited. Overall, commercial use of THz technology is growing as it allows for new measurement systems and broader applications.

Despite the on-going extensive research, the effective generation and detection

of terahertz signals especially using solid-state electronics is still a significant challenge. Parts of the THz frequency range used to be referred to as the THz-Gap because there had been no effective way of generating and detecting the THz signals [7] [8]. Also, the operating frequencies of semiconductor devices in the electronics domain (e.g. transistors) and in the photonics domain (e.g. lasers) do not overlap because in both electronics semiconductor materials and photonics semiconductor materials, the output power decreases when approaching the THz range [9]. This is illustrated in the output power versus frequency graphs of some electronic and photonic semiconductor devices in Figure 1.3 [9]. At the low frequencies of the THz range which is in the electronics domain, the semiconductor devices are limited by their low unity current gain cut-off frequency $(f_T) = 1/(2\pi\tau)$ because of the carrier transit time τ, which equals the transistor gate length divided by the drift velocity and their unity power gain frequency which is the maximum frequency of oscillation (f_{max}).

Some of the highest reported f_T for high electron mobility transistors (HEMTs) are 660 GHz and 644 GHz realised using the III-V semiconductor technology with 20 nm and 30 nm gate lengths respectively [10] [11]. The 30 nm gate InAs pHEMT transistor had an (f_{max}) of 681 GHz. For heterojunction bipolar transistors (HBTs), one of the highest f_T reported was for a 130 nm InP double HBT device at 520 GHz [12] with f_{max} around 1.1 THz [13] [14]. In designing with these transistor technologies, there is a frequency limitation as most circuits realised have to be under one-quarter of the cut-off frequency to achieve reasonable output power. At the higher frequencies of the optical domain, high output power is easily achieved using lasers, but size, high power supply requirements, (cryogenic) cooling and high cost makes them undesirable or unsuitable as solid state THz sources [15].
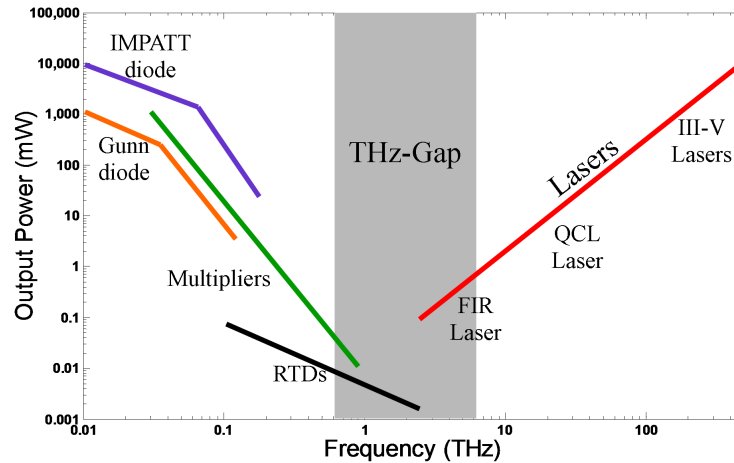
Figure 1.3: *Various semiconductor devices showing power output decreasing toward the THz-Gap (adapted from [9]).*

1.2 Sources

As mentioned in the preceding section, terahertz signals occur naturally in the universe emitted as parts of non-ionising black-body radiations greater than 10 Kelvin. This has helped greatly in understanding the universe through radio astronomy. But as these naturally occurring THz radiations are not controlled, potential applications outside the field of astronomy are limited. On the other hand, artificial generation of THz radiations has been difficult.

Most successful ways of generating terahertz signals have been either through up-conversion from millimetre range frequencies or down-conversion from optical range frequencies [15]. Up-conversion has been implemented in the past using Schottky diodes, Gunn diodes and Impact Ionization Avalanche Transit-Time (IMPATT) diodes, with power-combining techniques sometimes employed to achieve the desired output power levels [16]-[18]. For down-conversion sources, terahertz vacuum tubes and pumped gas lasers has been used to generate THz signals [19]-[22].

1.2.1   Lasers

The most commercially viable technique involves using sources such as lasers (stimulated emission of electromagnetic radiation), to generate THz radiation [15]. Since the frequencies of most lasers are at the high end of the THz range, some down-conversion through optical photo-mixing of two lasers is usually required to generate continuous wave (CW) THz signal. A simple illustration of optical photo-mixing to generate is shown in Figure 1.4. Here, two diode lasers which are slightly detuned in frequency are transmitted together using fibre optic cables. This is used to illuminate a photo-conductive emitter typically realised on gallium arsenide (GaAs) material. The photonic absorption and the photo-generated carrier lifetime results in a beat signal in the terahertz range [23]-[26].
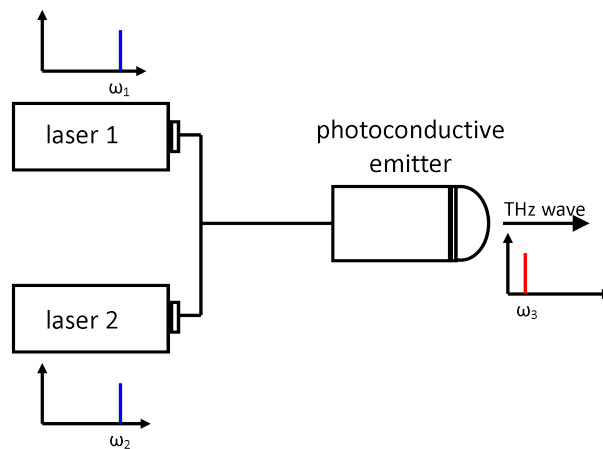
Figure 1.4: *Simple optical photomixing setup used to generate continous wave (CW) THz signal (adapted from [23]).*

This method of generating THz signals is mostly used in optical time-domain spectroscopy illustrated in Figure 1.5 [27]. In this time-domain spectroscopy system, a diode laser source which produces optical pulses in femtoseconds is seperated into two optical paths where one path travels through a time delay stage and hits the THz emitter while the other is delivered directly to the detector

which measures the amplitude of electromagnetic wave to calculate the change in waveform due to the sample. Changing the delay time between the two makes it possible to construct the electric field of the THz pulse in time domain and the frequency spectrum is then obtained through Fourier transform. Comparing the waveforms from the delayed pulse and the direct pulse with and without the sample, it is possible to estimate the complex refractive index of the sample and from this determine other related parameters [27]. The bulky nature and complexity of this set-up prevent use in applications outside a lab. Also, the output power from photomixing is in the very low micro-watt range [26].
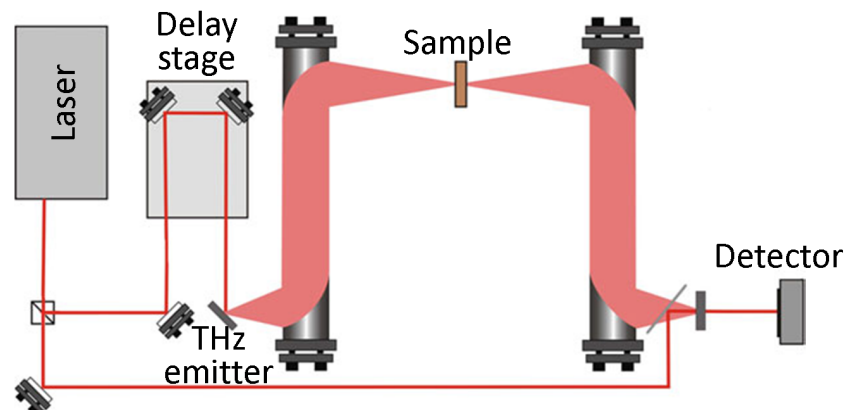
Figure 1.5: *Simple optical down-conversion used for terahertz time domain spectroscopy [27].*

Laser sources that emit at the low THz range such as quantum cascade lasers (QCL) can be used directly as THz sources. QCL lasers are solid-state semiconductor layers consisting of multiple quantum well heterostructure. QCL lasers have been reported to have a lowest frequency of 2.1 THz, providing up to 1.2 mW of power [20]. These lasers however require cryogenic cooling to operate, and the output power decreases dramatically with increasing temperature [27].

1.2.2 Frequency Multiplication

Frequency up-conversion and multiplication is achieved by using nonlinear devices which can generate harmonics from an input signal. Up-conversion is usually implemented using Schottky diode multipliers in complementary metal oxide semiconductor (CMOS) [16] and III-V semiconductor technologies [17][28]. Schottky diodes on 130 nm CMOS technology was used to realise circuits operating up to 860 GHz [16]. In III-V technology, GaAs Schottky diodes multiplier circuits were reported to generate 1.8 THz signals with 0.5 μW output power with future predictions of up to 1 μW at 2.5 THz [17]. Some disadvantages though are frequency up-conversion usually requires an RF input source and power combination, where the output from several sources are combined into one single-ended output to achieve desired power levels in the THz range. High noise levels and low power efficiency are also some of the limitations of this method of THz signal generation.

1.2.3 Vacuum Electronic Devices

Vacuum electronic devices such as terahertz vacuum tubes which operates based on thermionic emission, and other free electron sources such as backward wave oscillators (BWO) [29] and gyrotons [21], which operate based on stimulated cyclotron radiation of electrons in a magnetic field, can be used to generate up to kilo-watts (kW) of high-power THz radiations. The free electron devices could be slow-wave devices, i.e. BWO, where the dimensions of the interaction structures are the order of wavelength of the generated radiation or fast-wave devices (gyrotons) where the dimensions of the interaction structures are larger compared to the radiation wavelength [30]. The magnetic fields to accelerate the electrons are

usually provided by a superconducting magnet. Despite the high power output and long lifetime of the fast-wave devices, disadvantages of these sources are their large size and requirements for generating the required high magnetic field [15].

1.2.4 Negative Differential Resistance (NDR) Device based Oscillators

Negative (differential) resistance at single transistor ports when the other ports are appropriately terminated or devices with current-voltage $(I - V)$ characteristics that exhibit a negative differential resistance (NDR) region can be used to generate high frequencies, even THz signals [31]. Figure 1.6 shows a typical circuit diagram for a one port negative resistance device oscillator. Here, the device admittance Y_{source} is represented by $Y_{source} = -G_{source} + jB_{source}$ where $-G_{source}$ is the device conductance and B_{source} the susceptance. The load admittance Y_{load} is represented by $Y_{load} = G_{load} + jB_{load}$. Oscillations occur in the circuit when the total circuit conductance is negative, i.e.[31].

$$G_{load} - G_{source} < 0 \tag{1.2}$$

Some common devices that exhibit NDR region are Gunn diode, impact ionization avalanche transit-time (IMPATT) diode, tunnel injection transit time (TUNNETT) diode and resonant tunnelling diode (RTD). Unlike in the case of frequency up-conversion, NDR devices only require a DC input signal (and a suitable external passive circuit) to produce a RF output signal.

The Gunn diode which is a transferred electron device (TED) is fabricated on an N-type semiconductor material unlike regular $p - n$ junction diode. It is a two terminal device with three energy band levels; valence, conduction and a third
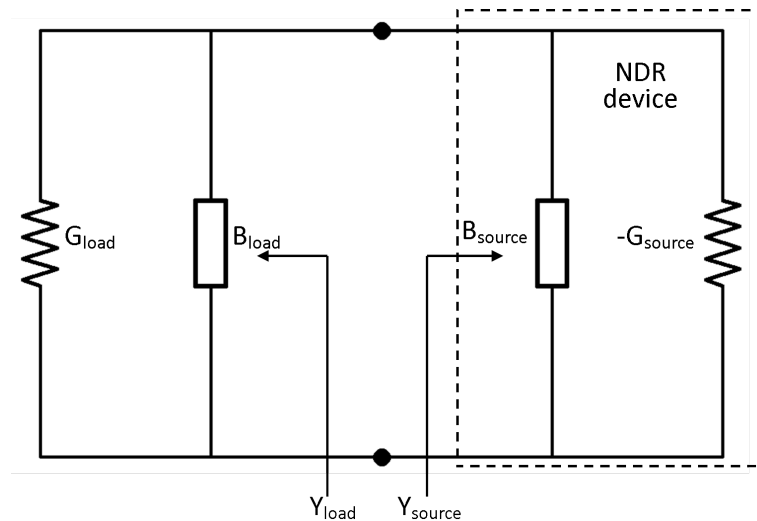
Figure 1.6: *Circuit for one port negative resistance device oscillator.*

band which has less mobility [32] [33]. The NDR is formed when the effective mass of the electrons reaching this band is increased and their drift velocity decreases. Frequencies up to 162 GHz with 25 mW output power was reported with induim phosphide (InP)-based Gunn diode oscillators mounted on diamond heat sink [34]. Planar Gunn diode-based oscillators have been reported with fundamental frequency of 164 GHz realised on indium gallium arsenide (InGaAs) material with 98 μW output power [35].

The IMPATT diode, unlike Gunn diode, is a $p-n$ junction device that utilizes avalanche breakdown under reverse bias conditions combined with charge-carrier transit time to produce negative differential resistance. IMPATT diode oscillators have been reported with fundamental frequencies up to 217 GHz in continuous wave mode with combined output power of 1 W [36]. Simulated models have also reported the possibility of 60 W RF power at 330 GHz from IMPATT oscillators [37], but realising this would require improvements in the growth of high quality 3C-SiC substrate [38]. One disadvantage of the IMPATT diode is that the nature of the avalanche breakdown is quite noisy, making IMPATT diodes susceptible

to high phase noise [39].

TUNNETT diode was introduced from analysis of high frequency performance of IMPATT diodes. They can be used to generate higher frequencies (100 GHz - 1 THz). At high frequency, the electron tunneling effect becomes more dominant than the avalanche process [40]. TUNNETT diodes have lower phase noise and can be used to achieve frequencies higher than IMPATT diodes, but with lower output power -61 dBm (0.8 nW) at 655 GHz and -67 dBm (0.2 nW) at 701 GHz [41] [42].

Resonant tunneling diodes which operate on the principle of quantum tunneling of particles through barriers [43] are capable of very fast operation with the double barrier structured RTD being the fastest electronic device to date. Oscillators based on resonant tunnelling diodes show the greatest potential among the NDR devices in bridging the THz-Gap. RTD-based oscillators have been reported operating at 1.1, 1.46 and 1.55 THz but are limited by their low output power of 0.2, 0.36 and 0.4 μW respectively [44]-[46]. For RTDs to be useful, their RF output power need to be increased to milli-watt levels in the 0.1 THz to 1 THz frequencies range [47].

1.3   THz Detectors

Methods of terahertz signal detection have generated a lot of interest because of the use of THz time domain spectroscopy in the study of various materials. THz detection is difficult because the low photon energy levels are usually dominated by ambient background thermal noise. Detection of THz radiations is mainly done using two main methods; coherent detection and incoherent (direct) detection [48].

- Coherent detection is usually done using heterodyne detectors with superconductor-insulator-superconductor (SIS) mixers [49][50]. This has mostly been used for high-resolution spectroscopy. Heterodyning is done to reduce signal to noise ratio by reducing the bandwidth. Heterodyne detection uses a nonlinear device to multiply a local oscillator (LO) signal with a received signal from an antenna. The signal is down-converted to the intermediate frequency (IF) signal which is detected, usually after amplification, using digital fast Fourier transform spectrometers. The phase and amplitude of the received signal is preserved for signal processing.

- Direct detectors are based on the principles of power absorption and square law detection. They are operated either at room temperature or cooled and are used for applications that do not require very high spectral resolution due to sensitivity issues. Examples of direct detectors are the conventional bolometer, which is based on direct thermal absorption and change in resistivity, antenna coupled micro-bolometer [51], Golay cell which is based on thermal absorption in a gas chamber [52], and antenna-coupled Schottky diodes based on square-law detection [49] [53] [54].

1.4   THz Antennas

To fully realise the potential of THz radiation including high data-rate wireless communication, antennas capable of efficient transmission and receiving of THz signals are needed to help overcome the limitations of low-power and other constraints mainly atmospheric loss. Because a vast majority of antennas function as resonators and the ideal resonant length is half the wavelength at the operating frequency, most of the antenna designs at the THz frequency range are very small

in physical size. This leads to a smaller effective aperture. Also, the skin effect at such high frequencies leads to increased resistance and losses.

To address the problem of low power in the THz range, high directivity antennas are required to radiate most of the power in the desired direction. Some conventional antennas such as the Yagi Uda antenna and the horn antenna are directive, but some research suggests that adding lenses can improve directivity and gain [55]-[57]. Modified conventional antennas would work at THz frequencies, and some have been demonstrated up to 0.34 THz [58]-[60].

1.5 Thesis Aim and Organisation

The aim of this PhD project was to realise and characterise various components required for the realisation of a solid-state THz technology. The work includes characterising tunnel diodes and RTD devices (for eventual use as solid-state THz sources) as well as the design, realisation and characterisation of a broadband THz planar Yagi antenna. A new circuit based on power-combining technique for tunnel diode (TD)-based oscillators will also be described.

This thesis is organised as follows: Chapter 1 (this chapter) introduces and reviews THz radiation and its characteristics including wavelength, safety and limits. Common THz sources are described in this chapter, while methods of detection of THz signals are also briefly discussed including a section on THz antennas.

Chapter 2 describes the operating principles of two negative differential resistance (NDR) devices: Tunnel diodes and RTDs including the quantum tunneling effect and the formation of the NDR region with applied bias voltage.

Chapter 3 reviews and presents a method of accurate DC current-voltage $(I - V)$ characterisation in the NDR region of TDs and RTDs (fabricated with help by Dr. Jue Wang) using pulsed DC. The device characteristics are modelled using a physics-based current density-voltage $(J - V)$ model using fitting/optimisation.

Chapter 4 describes and presents microwave frequency characterisation of the RTD at various bias conditions. An extracted small-signal equivalent circuit model from the scattering parameter measurements is presented in this chapter.

Chapter 5 describes a novel design procedure for tunnel diode or resonant tunneling diode oscillators. The circuit based power combining topology is for two oscillators with a single load. The proposed circuit was designed and realised in microstrip technology using tunnel diodes as the active elements. The design approach and experimental results are presented in this chapter.

Chapter 6 discusses antenna theory and presents an ultra-wideband Yagi-Uda antenna (fabricated by Khalid Alharbi) with experimental results. The design is based on a conventional antenna but scaled to work at 200 GHz. A new on-wafer radiation pattern characterisation method of this antenna is also presented and the measured radiation pattern is compared with simulated radiation pattern.

Conclusions and future work are discussed in Chapter 7.

Chapter 2

Tunnel Diodes and Resonant Tunneling Diodes

2.1   Introduction

Devices with negative differential resistance (NDR) region, where the ratio of the change in voltage (ΔV) and current (ΔI) is less than 0, $\Delta V/\Delta I < 0$, can generate (high frequency) power from the applied bias voltage as opposed to positive differential resistance which dissipates such applied power. This makes it possible for devices with NDR regions to produce AC power from a DC input. One of the most commonly known device that exhibits a negative differential resistance is the tunnel diode, which was developed by Leo Esaki in 1957 after noticing a new phenomenon in a heavily doped germanium $p - n$ junction diode [61]. Later in 1973 together with Raphael Tsu, they observed resonant energies in multi-barrier tunneling on experimental GaAs/AlGaAs super-lattice structures [62]. In 1974, Chang, Esaki and Tsu observed the tunnelling of electrons in a thin GaAs structure sandwiched between two AlGaAs barriers with the I-V characteristics showing current peaks at resonant energies [63]. Since then, resonant tunnelling

diodes have been developed and realised on various III-V semiconductor materials. They can also be realised in the silicon-germanium (Si/SiGe) material system [64] which has the potential of easy integration with the existing silicon (Si) technologies.

Figure 2.1 shows the typical forward characteristic of a tunnel diode or resonant tunneling diode (solid line) along with the characteristic of a conventional $p - n$ junction diode (dashed line) showing the peak and valley current points, I_p and I_v, the peak and valley voltage points, V_p and V_v, and the negative differential resistance region. An important figure of merit of NDR devices is the peak-to-valley current ratio (PVCR), I_p/I_v which can be determined from the current voltage characteristics of the device [65]-[67].
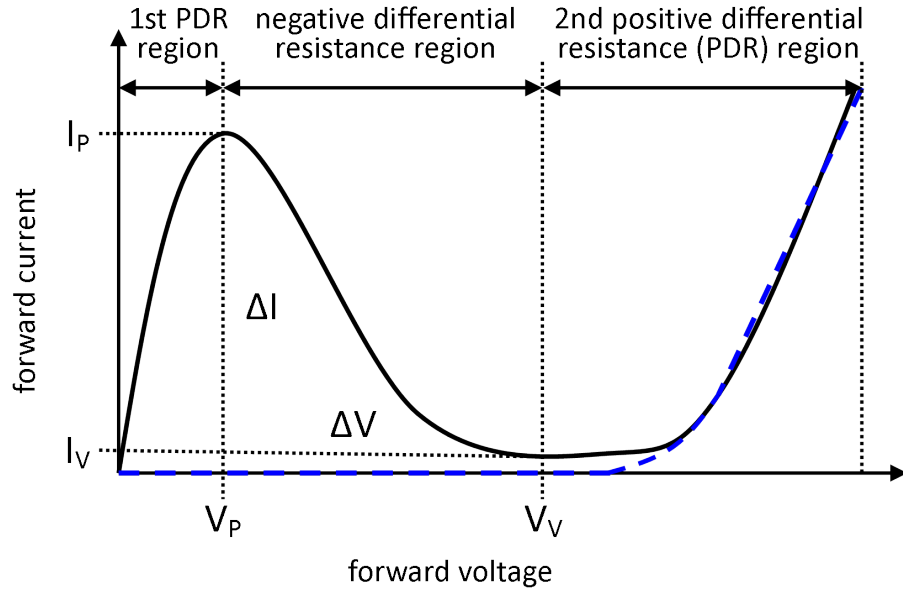
Figure 2.1: *Typical forward current-voltage characteristic of a resonant tunnel diode or tunnel diode (solid-line) showing peak voltage point V_p, valley voltage point V_v, peak current point I_p, valley current point I_v and the negative differntial resistance (NDR) region with that of a conventional p-n junction diode (dashed-line).*

The peak-to-valley current and voltage differences are denoted by ΔI and ΔV,

respectively. The maximum absolute value of the small-signal negative conductance, $G_{n(max)}$, can be expressed in terms of ΔI and ΔV [68], [69]-[71].

2.2   TD/RTD Maximum Negative Differential Conductance, $-G_{n(max)}$

Figure 2.2a shows the large signal model of a TD/RTD can be represented by a voltage controlled current source $I(V)$, with self-capacitance of the device C_n. The voltage controlled current source can be represented by a cubic polynomial in Equation 2.1 [69] where the origin is shifted to the middle of the NDR region for convenience as shown in Figure 2.2b and expressed mathematically by

$$I(V) = -aV + bV^3 \tag{2.1}$$

where a and b are both positive constant coefficients.

Equating the gradients at the peak and valley points of the curve to zero, the constants a and b can be expressed as

$$\frac{dI(V)}{dV} = -a + 3bV^2 = 0 \tag{2.2}$$

The bias voltages at the peak and valley points V_p and V_v respectively can then be derived from Equation 2.2 as,

$$V_p = -\sqrt{\frac{a}{3b}} \tag{2.3}$$

Figure 2.2: *(a) TD/RTD device large signal model showing self-capacitance C_n in parallel with voltage controlled current source I(V) [69]. (b) Voltage controlled current source model from cubic polynomial.*

$$V_v = \sqrt{\frac{a}{3b}} \tag{2.4}$$

and the currents at the peak and valley points I_p and I_v respectively, can be derived by

$$I_p = -aV_p + bV_p^3 \tag{2.5}$$

$$I_v = -aV_v + bV_v^3 \tag{2.6}$$

From Equations 2.3 to 2.6, the difference in peak to valley current, ΔI, and voltage, ΔV, can be expressed as

$$I_p = a\sqrt{\frac{a}{3b}} - b\left(\sqrt{\frac{a}{3b}}\right)^3 \tag{2.7}$$

18

$$I_v = -a\sqrt{\frac{a}{3b}} + b\left(\sqrt{\frac{a}{3b}}\right)^3 \tag{2.8}$$

$$\Delta I = I_p - I_v = \frac{4a}{3}\sqrt{\frac{a}{3b}} \tag{2.9}$$

$$\Delta V = V_p - V_v = 2\sqrt{\frac{a}{3b}} \tag{2.10}$$

The constants a and b can be expressed as $a = (3\Delta I)/(2\Delta V)$ and $b = (2\Delta I)/(\Delta V)^3$. The maximum value of the negative conductance $-G_{n(max)}$ located at the middle of the NDR region, which is represented in Figure 2.2b as the origin. It is equal to $a = (3\Delta I)/(2\Delta V)$ [69][70]. This analysis helps determine the optimum load conductance value for maximum power to be delivered to the load as will be described in Chapter 5.

$$G_{n(max)} = \frac{3\Delta I}{2\Delta V} \tag{2.11}$$

The next section describes electron tunneling effect in tunnel diodes and RTDs and briefly describes structures of RTDs in III-V technologies.

2.3 Principles of Operation

2.3.1 Tunnel Diode

A tunnel diode is a highly doped $p-$ and $n-$type junction semiconductor device e.g. galluim arsenide (GaAs) typically with doping concentrations around $10^{19}cm^{-3}$ to $10^{20}cm^{-3}$ [72] [73]. This creates a very thin depletion region as the

$p-n$ junction becomes abrupt. The Fermi-level is moved towards the conduction band or the valence band depending on the concentration of donors or acceptors, respectively [73]. Current flow in the tunnel diode is mainly due to the quantum mechanical principle of electron tunneling. This is as a result of matter behaving as both a wave and a particle.

Traditionally, an electron can only surmount a barrier if it possesses energy exceeding that of the barrier height, but in quantum theory, it can tunnel through (some distance of) the barrier with less energy than that required to cross it. In the case of tunnel diodes, the barrier formed at the junction is thin enough to allow successful electron tunneling to the other side of the barrier. Figure 2.3 shows the cross sections of highly doped $p-n$ junction structures with the Fermi-level in the conduction and valence bands. E_c, E_v and E_f are the conduction band, valence band and Fermi-level, respectively, while V, V_p and V_v are forward voltage, peak voltage and valley voltage, respectively.

In Figure 2.3(a), when there is no applied bias voltage V, there is no current flow. When V is applied and slowly increases as seen in Figure 2.3(b), electrons from the conduction band begin to tunnel through the thin barrier to the valence band in the $p-$region as the region between the Fermi-level, E_f, and the conduction band, E_c, in the n region of the semiconductor increases and the electrons move to empty states in the p region thereby causing a forward tunnel current. As the applied voltage V slowly approaches peak voltage point V_p, the energy in the $n-$region equals the holes in the $p-$region causing maximum tunnelling current as shown in Figure 2.3(c). Above this voltage level, there are less empty states in the $p-$region for electrons to tunnel into leading to a decrease in the forward tunnelling current hence creating a negative differential resistance region seen in Figure 2.3(d). This decrease continues with increasing forward voltage until there

are almost no available states in the $p-$region for electrons to tunnel through the barrier to occupy. This is when the valence band in the $p-$region lines up with the $n-$region conduction band, and this point is known as the valley region.
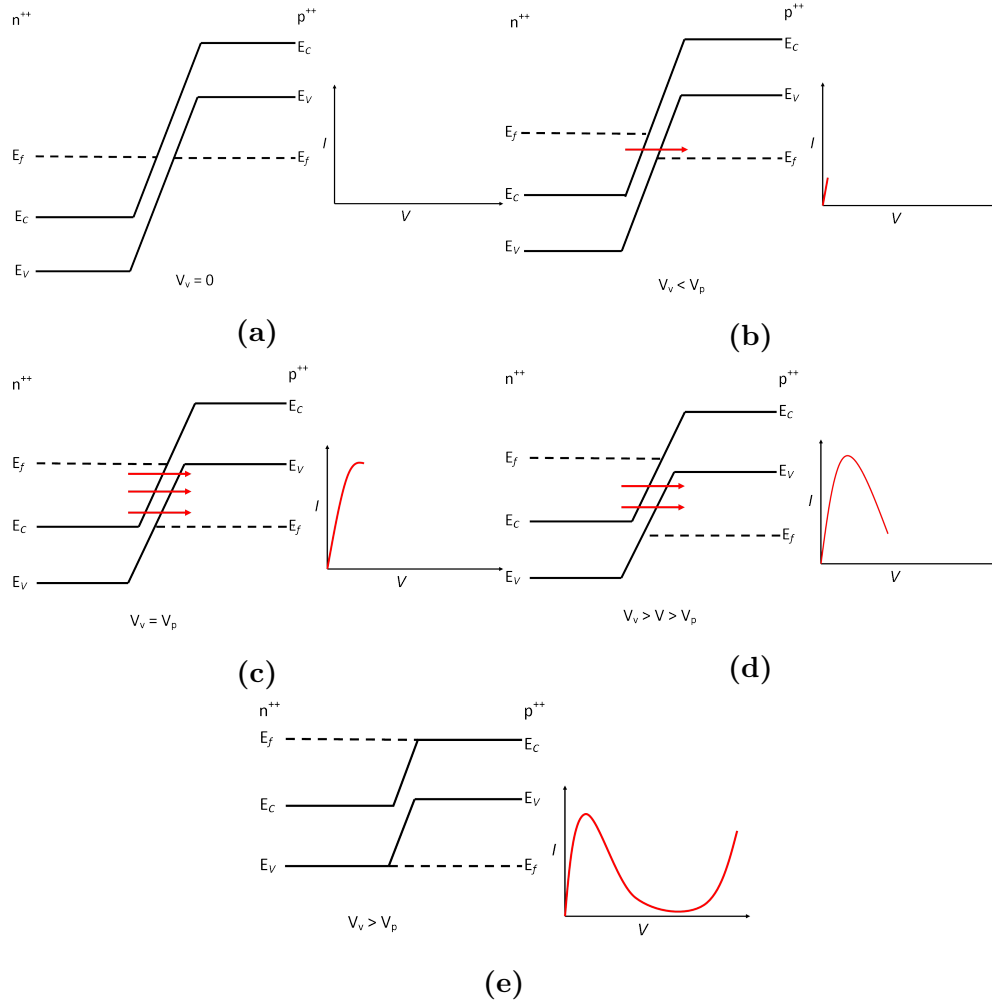
Figure 2.3: *Cross section of highly doped p and n junction which forms the tunnel diode with corresponding band diagram and tunnelling current at various forward bias conditions [74] (a) no forward bias voltage, (b) small forward bias voltage applied and tunneling starts to occur, (c) bias voltage at peak voltage point showing peak tunneling current (d) bias voltage above peak voltage point showing the negative differential region and (e) Thermal excitation when bias voltage exceeds valley voltage point.*

With further voltage increase above the valley voltage, V_v, point in Figure 2.3(e), forward current starts to increase again due to lower potential barrier as observed in the classic $p-n$ junction diode current-voltage characteristic due to the diffusion of majority carriers.

The tunneling current-voltage $(I-V)$ characteristic of the tunnel diode can be estimated by [74][75],

$$I_{tunnel} = I_p \left(\frac{V}{V_p} \right) exp \left(1 - \frac{V}{V_p} \right) \qquad (2.12)$$

where I_{tunnel} is the tunneling current and I_p is the peak current. Tunnel diodes are usually fabricated using the ball alloy method where an alloy with the right doping is brought in contact with a heavily doped substrate or pulsed electroplating where an appropriately doped metal is deposited to a highly doped substrate using interrupted direct current [74].

2.3.2   Resonant Tunneling Diode (RTD)

The resonant tunneling diode is a two terminal device which operates on the principle of electron tunnelling. It is a heterostructure. A heterostructure is a device having a combination of heterojunctions, and the heterojunction is a junction formed between two dissimilar layers having unequal energy band gaps. It is usually manufactured using molecular beam epitaxy (MBE). The RTD in its most common form, is a double barrier structure which consists of an undoped narrow band gap material layer which forms the quantum well sandwiched between two undoped large band gap material layers which are the barriers [43][74][76].

The quantum well and barriers are located between two heavily-doped n-type materials with small band gaps which form the emitter and collector regions.

A typical layer structure of a resonant tunneling diode is shown in Figure 2.4 with the corresponding energy band diagram where $E_{C,E}/E_{C,C}$ represents the emitter/collector conduction layer, $E_{F,E}/E_{F,C}$ the emitter/collector Fermi-energy level and E_{r1} and E_{r2} the resonant energy levels. Because the dimensions of the double barrier structure are comparable to the electron wavelengths, the electron wave nature allows tunnelling through the double barrier quantum-well (DBQW) structure to occur with a bias voltage.
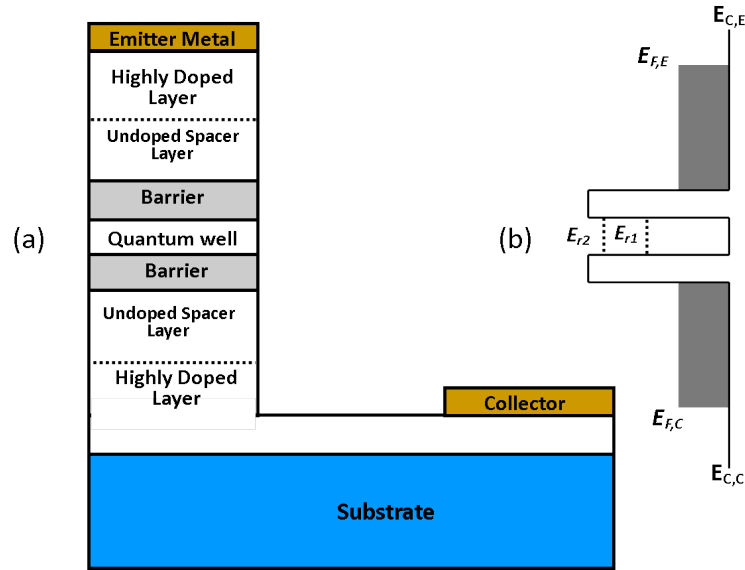
Figure 2.4: *(a)Typical layer structure of the resonant tunnelling diode double barrier quantum well structure, showing the quantum well which is formed between the two barriers made up of layers of undoped wider band gap semiconductor material. (b) Corresponding conduction band diagram showing the Fermi level of the emitter and conductor layers ($E_{F,E}$ and $E_{F,C}$), the conduction bands of the emitter and collector, ($E_{C,E}$ and $E_{C,C}$), and the resonant energy levels (E_{r1} and E_{r2}).*

The materials are chosen to achieve band gaps which improve electron mobility by reducing the electron effective mass [77]. The layers can also be optimised

to improve the performance of the RTD. Reducing the quantum well thickness increases the first resonant energy level which increases the tunneling current and the PVCR is increased. However, this shifts the peak bias voltage to a higher value [78]. Reducing the barrier thickness increases the transmission probability therefore increasing the current density [76]. The undoped spacer layers are used to prevent diffusuion of dopants to subsequent layers. Reducing the spacer layers improves the PVCR, but this leads to an increase in the self capacitance which reduces the high frequency performance of the device[77].

The conduction band diagram of the double barrier resonant tunneling diode structure at different states of forward bias is presented in Figure 2.5 showing the resonant energy states, E_{r1} and E_{r2}, the Fermi energy levels, $E_{F,E}$ and $E_{F,C}$, the conduction bands, $E_{C,E}$ and $E_{C,C}$.

At zero bias voltage, there is thermal equilibrium and no current flows as seen in Figure 2.5(a). When the positive bias voltage is applied to the collector and slowly increased, the chance of electrons tunneling through the barrier increases. The electrons form a layer at the emitter and tunneling starts to occur through the barrier and some current is produced. As the voltage continues to slowly increase, the first resonant energy level, E_{r1} is moved to the Fermi energy level $E_{F,E}$ in the conduction band as can be seen in Figure 2.5(b) and more electrons can tunnel through to the collector, leading to an increased current. The peak tunneling current is achieved when the energy level matches the conduction band at the energy level $E_{C,E}$ as seen in Figure 2.5(c). Here, the resonant energy state is reached and above this, fewer electrons can go through and the tunneling current starts to decrease creating a negative differential resistance as shown in Figure 2.5(d). In Figure 2.5(e), at larger forward voltages the electrons acquire high enough energy and thermal emission over the barrier starts to occur and the

current rises again with bias voltage [79].
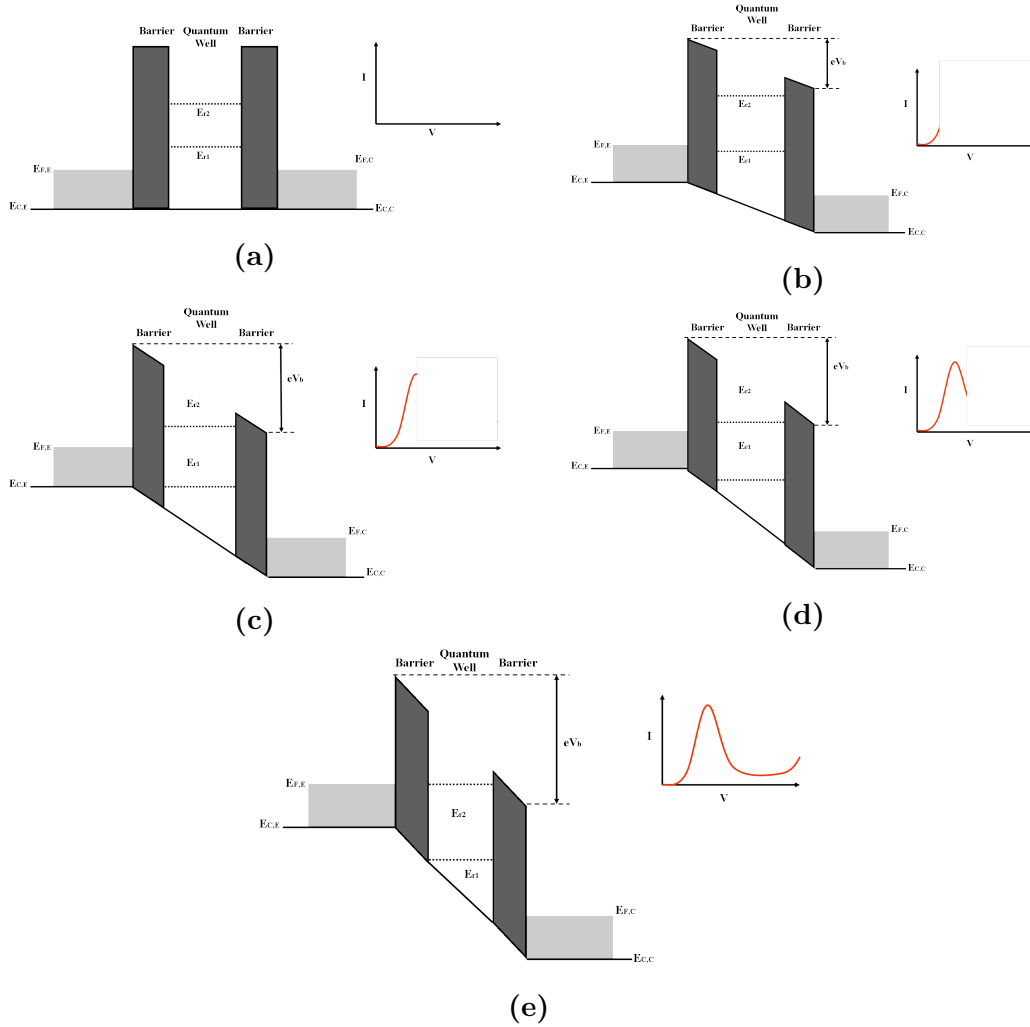
Figure 2.5: *Conduction band diagram of a double barrier quantum well structure forming the resonant tunnel diode at different forward bias (V_b) conditions: (a) no bias (b) positive bias applied to the emitter in forward bias condition at threshold voltage (c) forward bias at peak voltage (resonant tunneling) (d) NDR region showing decreasing tunneling current and (e) forward bias above valley voltage (non-resonant energy).*

The resonant tunneling diode is a much faster device than the tunnel diode,

and this and its structural simplicity makes it quite useful for high frequency oscillation circuits into the THz range. Compared to the tunnel diode, the RTD is faster because of its very low self-capacitance, C_n [80].

$$C_n = \frac{\varepsilon A}{d} \tag{2.13}$$

In Equation 2.13 for tunnel diodes, A is the junction area and it is the mesa size for RTDs, d is the depletion layer thickness for tunnel diodes and the quantum well width including the spacer layers for RTDs. ε is the dielectric constant of the material [76][80].

2.3.2.1   RTD Materials

RTD devices are usually realised using III-V semiconductor materials [81]-[83]. III-V materials possessing small effective electron mass (m^*) have high electron mobility, and these materials with high conduction band offset can improve the peak voltage-current ratio by supressing thermal electron current [84].

Some typical III-V materials used to realise RTDs are GaAs/AlGaAs [82], InAs/AlSb [85] and InGaAs/AlAs [68][86]. The RTD layer structure for InGaAs/AlAs RTD device characterised in this thesis is shown in Table 2.1 with layer thicknesses [68][83] [87] [88]. Attempts have also been made to realise RTDs in silicon-based materials such as silicon germanium, Si/SiGe [89]. This would allow for easy integration with existing complementary metal oxide semicondutor (CMOS) process used in logic circuit designs [37] [64]. However, Si-based RTDs are still an immature technology as few researchers spend time developing Si-based RTDs because they are predicted to be theoretically inferior to III-V RTDs. Si-based materials have lower peak current density and peak-to-valley current ratio due

Table 2.1: *InGaAs/AlAs material parameters layer structure for InGaAs/AlAs-based RTD device [68].*

InGaAs/AlAs Material Parameters				
m_0 is the electron mass at rest, $9.11 \times 10^{-31} kg$				
Material	Effective mass m^*	Band gap $E_g(eV)$	Dielectric constant ε_r	Conduction band offset $\Delta E_c(eV)$
In$_{0.53}$Ga$_{0.47}$As	$0.042m_0$	0.71	12.9	0.65
AlAs	$0.1m_0$	2.16	10.1	

RTD Layer structure (Dopant Si)				
Layer	Thickness (nm)	Composition	Doping level (cm^{-3})	Description
1	40	InGaAs	3×10^{19}	Contact
2	80	InGaAs	2×10^{18}	Emitter
3	50	InGaAs	2×10^{16}	Spacer Layer
4	1.4	AlAs	Undoped	Barrier
5	5.5	InGaAs	Undoped	Well
6	1.4	AlAs	Undoped	Barrier
7	50	InGaAs	2×10^{16}	Spacer Layer
8	80	InGaAs	2×10^{18}	Collector
9	10	InP	1×10^{19}	Etch Stop
10	400	InGaAs	3×10^{19}	Contact
11	200	InAlAs	Undoped	Buffer Layer
Substrate InP 635 μm				

to the smaller conduction band offset between Si and SiGe in the double barrier heterostructure when compared to III-V semiconductor materials [89][90].

2.4 Summary

In this chapter, the operating principles of tunnel diodes and resonant tunnel diodes have been explained including an explanation of the creation of the neg-

ative differential region (NDR) in their $I - V$ characteristics. The NDR region enables these devices to be used as active devices in high frequency oscillators. The DC and RF characterisation of TDs and RTDs is described in Chapters 3 and 4.

Chapter 3

DC characterisation of Tunnel Diodes and Resonant Tunneling Diodes

3.1   Introduction

Accurately measuring the current-voltage $(I - V)$ characteristics of devices with inherent negative differential resistance (NDR) regions is difficult to do directly without the aid of adding external components. This is due to the parasitic oscillations in the bias circuit [91]-[94]. In this chapter, the problem of unwanted parasitic bias oscillations in the negative differential region of tunneling diodes and resonant tunneling diodes is briefly discussed. Pulsed measurements as a direct way of DC characterisation of these devices in the NDR region is discussed and experimental results are presented for an indium phosphide-based RTD and a commercially available germanium 1N3712 tunnel diode. A physics-based analytical model is also used to describe the current density of the RTD with bias and shows an excellent fit with the data from the pulsed I-V characteristics.

3.2   Bias Oscillations in Tunneling Diodes

Figure 3.1a shows a typical TD/RTD device when biased and Figure 3.1b shows the corresponding current/voltage characteristics. In Figure 3.1a, L_b and R_b represent the inductance of the biasing line cables and the resistance respectively. In Figure 3.1b the difference in the peak-to-valley current and voltage in the NDR region is shown and is denoted by ΔI and ΔV, respectively.
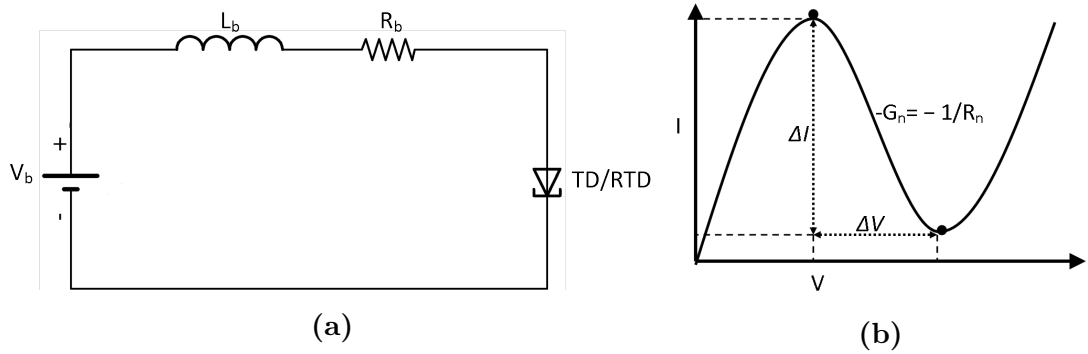
Figure 3.1: *TD/RTD with DC biasing showing biasing line modelled with inductance, L_b and resistance, R_b, (b)I-V characteristics showing voltage and current range ΔV and ΔI of the NDR region.*

When the device in Figure 3.1a is biased in the NDR region, the circuit has unwanted oscillations when the net resistance seen by the DC source is negative. Due to large equivalent inductance from the biasing lines, the frequency of these unwanted oscillations are low. These unwanted oscillations lead to a distortion of the measured I-V characteristics of an NDR device [71].

Figure 3.2 shows the AC or small-signal equivalent circuit of Figure 3.1a when biased in the NDR region. The DC supply is replaced by a short circuit and the device is represented here by its negative differential conductance, $-G_n$, in parallel its self-capacitance, C_n. The resistance of the biasing line is very small, so it is neglected in the RF equivalent circuit in Figure 3.2b
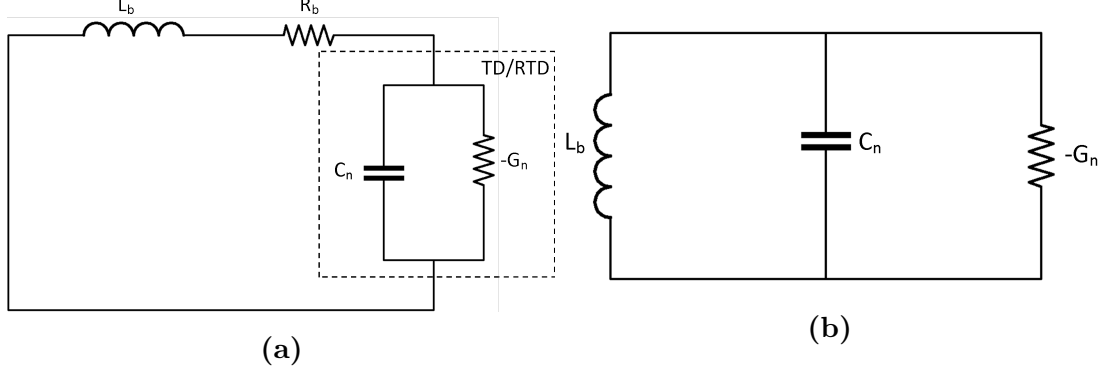
Figure 3.2: *(a)Small-signal equivalent circuit of a TD/RTD biased in the NDR region with the device represented by the self capacitance, C_n and negative conductance, $-G_n$. (b) RF equivalent circuit.*

The admittance of the circuit in Figure 3.2b is given by

$$Y = -G_n + j\omega C_n + \frac{1}{j\omega L_b} \tag{3.1}$$

Oscillations will exist in the circuit because the net conductance is negative, see Equation 1.2. The oscillation frequency is determined by C_n and L_b, and since L_b is large, the frequency tends to be low, in the MHz range. These oscillations distort the DC measurements in the NDR region. A commonly used but indirect method of determining the $I - V$ in the NDR region is to connect a stabilising resistor, R_{st} across the device shown in Figure 3.3a [95] [96] to ensure that the combined resistance is positive, and so effectively cancelling out the NDR region. Figure 3.3b shows the AC small-signal equivalent circuit showing the device and the resistor for stabilising, R_{st} and the biasing line inductance, L_b.

The admittance of the circuit in Figure 3.3b is given by

$$Y = -G_n + \frac{1}{R_{st}} + j\omega C_n + \frac{1}{j\omega L_b} \tag{3.2}$$

31
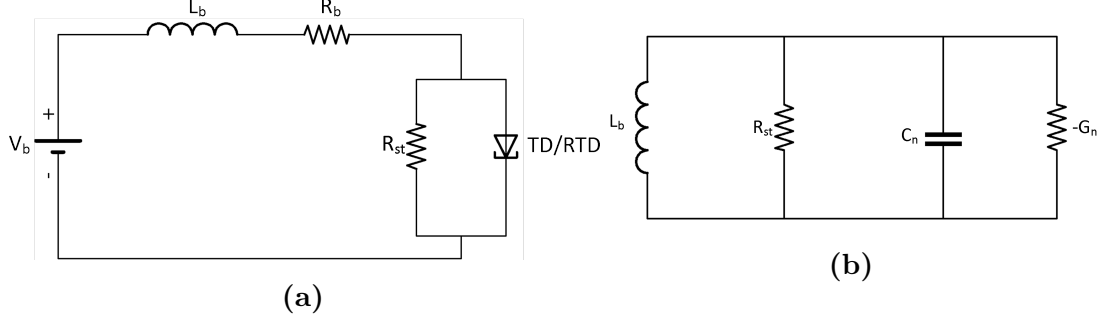
Figure 3.3: *(a)NDR device with shunt stabilising resistor R_{st} used for indirect I-V characterisation (b) Small-signal circuit with stabilising resistor showing parasitic inductance of biasing lines, L_b. The NDR device is represented here by the self capacitance C_n and the negative differential conductance $-G_n$.*

$$Y = -G_n + \frac{1}{R_{st}} + j\left(\omega C_n - \frac{1}{\omega L_b}\right) \qquad (3.3)$$

From Equation 1.2, the circuit would be stable if the real part of the admittance, Y_{real} is positive [31] [68] [97] [98], i.e.

$$\frac{1}{R_{st}} - G_n > 0 \qquad (3.4)$$

therefore at DC and low frequencies, the condition for stability is

$$R_{st} < \frac{1}{G_n} \qquad (3.5)$$

If the value of the R_{st} is chosen to satisfy Equation 3.5 above, the actual device I-V characteristics can then be determined indirectly [95] [99]. For devices realised on-wafer such as RTDs, the resistor for stabilising the circuit has to be added during fabrication making it a less robust method of accurately determining the device I-V characteristics. This is because of variations in measured actual resistance

values from the designed values for resistor fabrication using thin film technology [100]-[102].

Static DC measurements were made of a commercially available 1N3712 tunnel diode from American Micro Semiconductor, with peak current and valley current of 1 mA and 0.12 mA, respectively, and peak point voltage and valley point voltage of 65 mV and 350 mV respectively [103][104]. This was carried out using the Keysight Technology $B1500A$ semiconductor device analyzer without the addition of a stabilising resistor. Figure 3.4 shows a hump-shaped distortion in the NDR region of the measured $I - V$ plot between 60 mV and $270mV$ due to oscillations caused by the inductance of the bias cable.
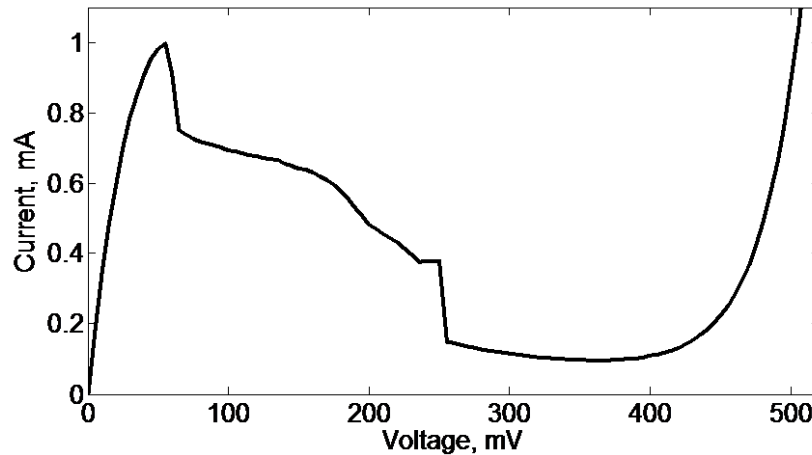
Figure 3.4: *TD I-V plot from static/standard DC showing effect of bias oscillations in the NDR region between 60 mV and 270 mV bias.*

3.3 Pulsed IV Measurements

Pulsed current-voltage (I-V) measurements where the DC bias voltage is applied in periodic pulses is an effective way of measuring active devices susceptible to temperature and charge trapping effects [105][106]. Unlike static DC method of

IV measurements, where increasing or decreasing voltage sweep is applied for the desired bias range, pulsed DC measurements are made from levels determined by the user to desired value for the chosen bias points throughout the voltage range [107].

Pulsed IV allows for the study of the dynamic properties and helps for the development of more accurate non-linear device models. Pulsed characterisation of TD and RTD in this thesis was done with the Keysight B1530A waveform generator/ fast measurement unit (WGFMU) module with its remote sensing unit (RSU). Figure 3.5 shows the WGFMU; it allows for ultra-high speed waveforms up to 10 ns resolution at 10 mA. It also allows measurements to be taken at any point in the pulse period [108].
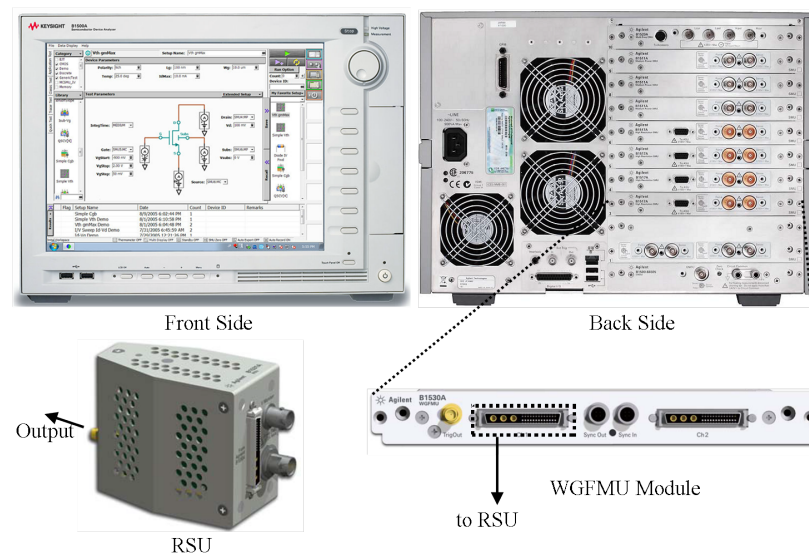
Figure 3.5: *Keysight B1530A waveform generator/ fast measurement unit (WGFMU) module with its remote sensing unit (RSU).*

3.3.1 Pulsed IV Characterisation of TDs and RTDs

Pulsed DC characterisation of TDs and RTDs was attempted for the first time on this project (to the best of the author's knowledge). Figure 3.6 shows a typical pulsed waveform where T_r and T_f are pulse rise times and fall time, respectively; the pulse duration is T_{on}; the pulse period is T_p; and the base voltage, is V_{base}. The pulse waveform was defined to allow the device under test (DUT) to attain settled maximum current reading at each corresponding bias voltage point. This is verified by outputting a single pulsed measurement of the current and voltage as a function of time.
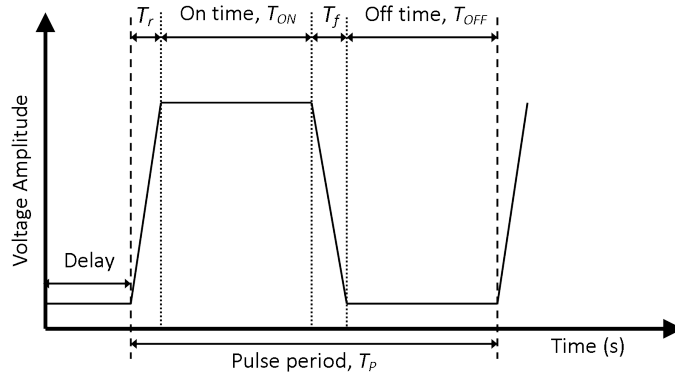
Figure 3.6: *A typical square pulse waveform*

As a benchmark, a 15 Ω metal film resistor was measured using static DC and pulsed DC with T_{on}, of 1 ms and rise/fall time of 1 μs and T_{on} of 10 ns with rise/fall times of 15 μs. The pulsed measured $I-V$ measurement was carried out on a test structure with sub miniature version A (SMA) coaxial connectors attached to the terminals of the device as shown in Figure 3.7, which is the same experimental measurement set-up used for characterising a tunnel diode.

Figure 3.8 shows the $I-V$ measurements of the 15 Ω resistor carried out using static DC and pulsed DC measurements. The measurements carried out using

35
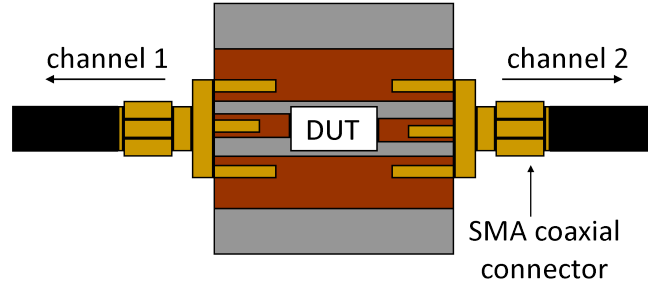
Figure 3.7: *Measurement set-up employed for experiment, voltage applied from channel 1 and current measured at channel 2. DUT is 15 Ω resistor for measurement verification, and tunnel diode for active device measurement.*

standard DC and pulses of widths, 10 *ns* and 1 *ms* are in agreement and display the accurate resistance value across the measured voltage range.
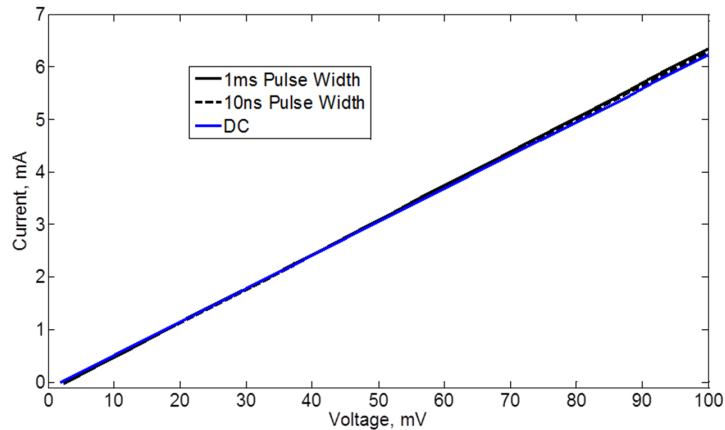
Figure 3.8: *I-V measurements of the 15 Ω resistor carried out using static DC and pulsed DC measurements*

A 1N3712 tunnel diode was then characterised using pulsed DC with the following parameters; T_{on} of 100 *ns* and T_r/T_f of 10 *ns*, this allows monitoring the presence/absence of oscillations at each bias point in the TD. Figures 3.9a shows the time domain measurements of the applied voltages and the current for the 1N3712 tunnel diode. Figure 3.9b shows a shorter time domain plot of the pulsed current measurement from peak current at the 7 *μs* to 14 *μs* time point which

36

shows the onset and the damping of unwanted bias oscillations in the NDR region.
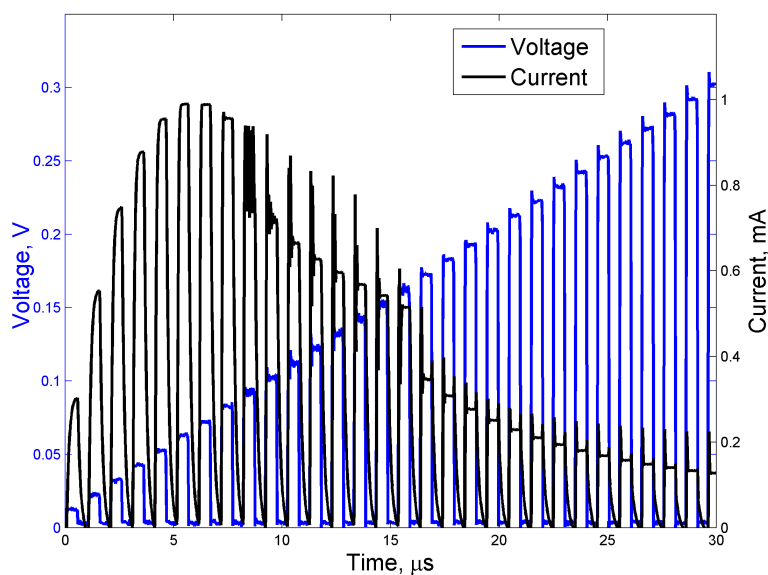
(a)
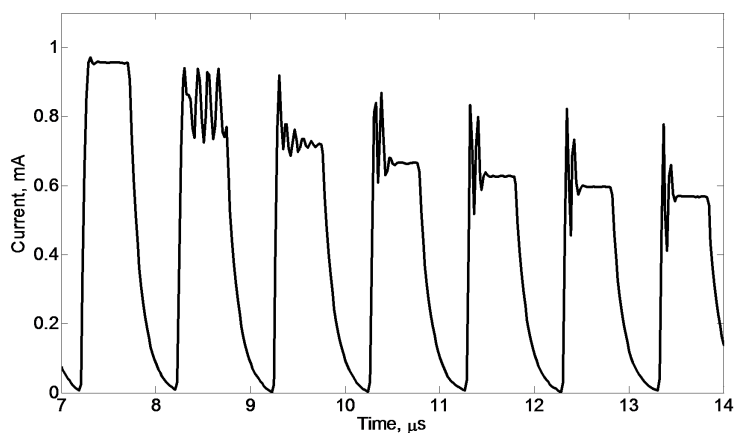
(b)

Figure 3.9: *(a) Applied voltage pulses and measured 1N3712 tunnel diode current pulses, (b) Measured current pulses from I_p at 7 μs showing the beginning and damping of the oscillations in the NDR region.*

The ability to measure $I - V$ with pulses allow monitoring the onset of oscillations and the regions in the traces where the current and voltage waveform both display

no oscillations. Since the pulsed measurement system allows measurements to be taken along any point of the pulsed waveform, measurements taken in the oscillation-free region can be used to accurately determine the I-V characteristics of the device in the NDR region.

To correctly characterise the TD/RTD in the NDR region, T_r, T_f, T_{on}, T_p and V_{base} have to be chosen carefully to allow enough time for damping of the oscillations therefore providing a stable window for measurements. This was achieved by observing the measured current waveform in the time domain. For the 1N3712 tunnel diode, a pulse voltage waveform of 100 ns with rise/fall times T_r/T_f of 20 ns in increasing $5mV$ steps for the bias range was applied to the anode from channel 1 and the corresponding current measured at the cathode from channel 2. Figure 3.10 shows the measured $I-V$ characteristic using DC pulses to be free from bias oscillations compared to the initial measurements done using standard DC [109].
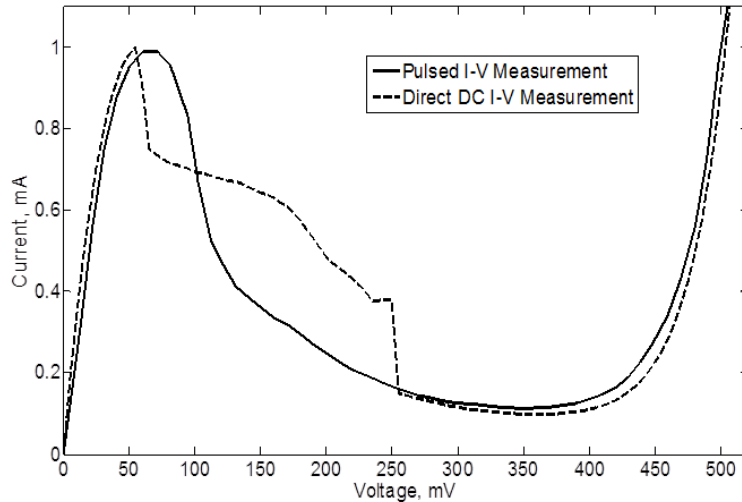
Figure 3.10: *1N3712 germanium (Ge) tunnel diode direct DC I-V measurement modified by oscillations in the NDR region and pulsed measured I-V showing no oscillations in the pulsed measurement NDR region [109].*

Pulsed DC characterisation of an InP-based RTD on-wafer was also carried out. The RTD was made from $In_{0.53}Ga_{0.47}As/AlAs$, with undoped $In_{0.53}Ga_{0.47}As$ quantum well and AlAs barrier layers of 5.5 nm and 1.4 nm respectively. The spacer layers were formed using slightly doped $In_{0.53}Ga_{0.47}As$ layers and the emitter and collector layers are made up of highly-doped $In_{0.53}Ga_{0.47}As$ layers [68]. During measurements, the device was contacted using two DC probes (from American Probe Technologies (APT) Inc.). Figure 3.11 shows a picture of the RTD being measured. Pulse voltage waveforms of 80 ns for T_{on} with rise/fall times T_r/T_f of 90 ns was applied. The increased rise time helped to minimise overshoot peaks in the applied voltage pulses caused by parasitic inductances of the biasing cables and sudden change in voltage state.
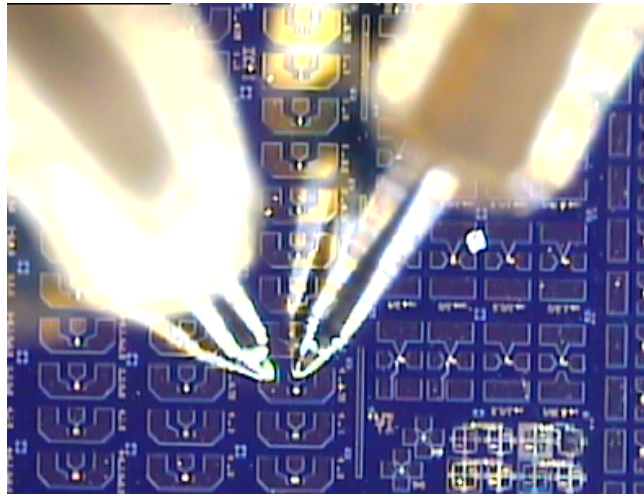
Figure 3.11: *Picture of RTD being measured with DC probes.*

Due to the higher peak current displayed by the InP RTD, a base voltage level V_{base} of 400 mV was used for the measurements. Figure 3.12 shows a close-up plot of a measured current and voltage pulse duration of the RTD in the NDR region [109]. The oscillations can be observed in the pulsed duration measurement in the NDR region and the stable window where measurement is taken can be seen

in the current plot. An identical voltage step of 5 mV was also used for the RTD and the measured $I - V$ characteristics are shown in Figure 3.13 for pulsed and standard DC [109].
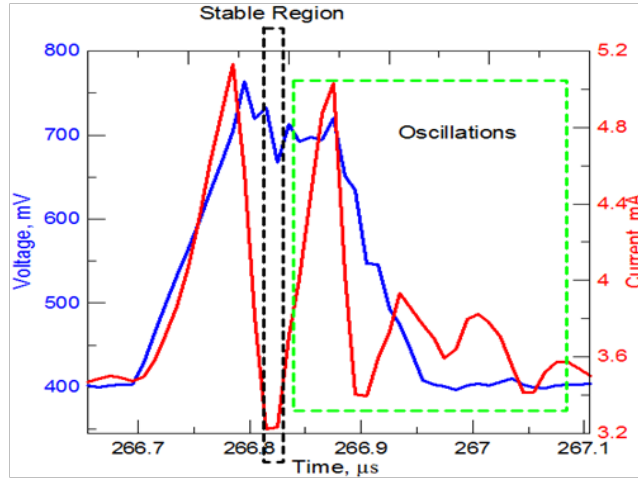
Figure 3.12: *Time domain plots from 266 μs to 267 μs of current and voltage pulse in the NDR region of an InP-based RTD showing oscillations and stable window for measurement [109].*
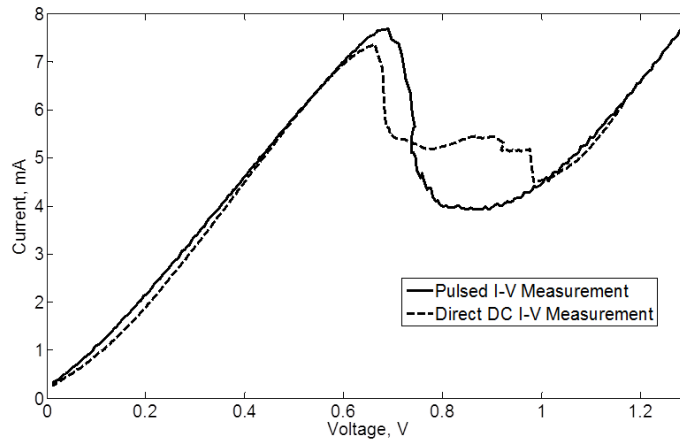
Figure 3.13: *RTD direct DC I-V measurement modified by oscillations in the NDR region and pulsed measured I-V showing no oscillations in the pulsed measurement NDR region [109].*

3.3.2   Discussion

The first and second derivatives of the measured current-voltage characteristics plots, $\frac{dI}{dV}$ and $\frac{d^2I}{dV^2}$, can be used to detect the presence or absence of parasitic oscillations in the measured $I-V$ characteristics [95] [96]. Figures 3.14 and 3.15 show the first and second derivative plots of the measured I-V curves of the 1N3712 tunnel diode. Figures 3.16 and Figure 3.17 shows the first and second derivative plots of the measured I-V curves of the InP-based RTD [109].
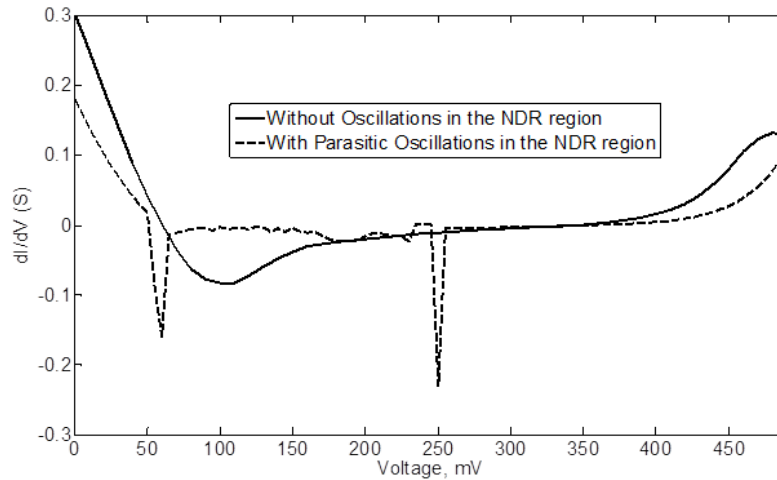
Figure 3.14: *First derivative of the I-V curves of the 1N3712 diode showing the presence of oscillations (valleys) on the direct DC measurement at 50 mV to 250 mV range [109].*

The measurement carried out using static DC shows effects of the parasitic oscillations in the NDR region between 50 mV to 250 mV bias for the tunnel diode and 0.69 V to 1.2 V for the RTD. The measurments carried out using DC pulses are seen to be free of parasitic bias oscillations. For the measurements showing oscillations, the sudden changes in current in the NDR region is seen as sharp valleys in the first derivative plots of the measured $I-V$ characteristics and in the second derivative plots and the effects of the bias oscillations can be seen as
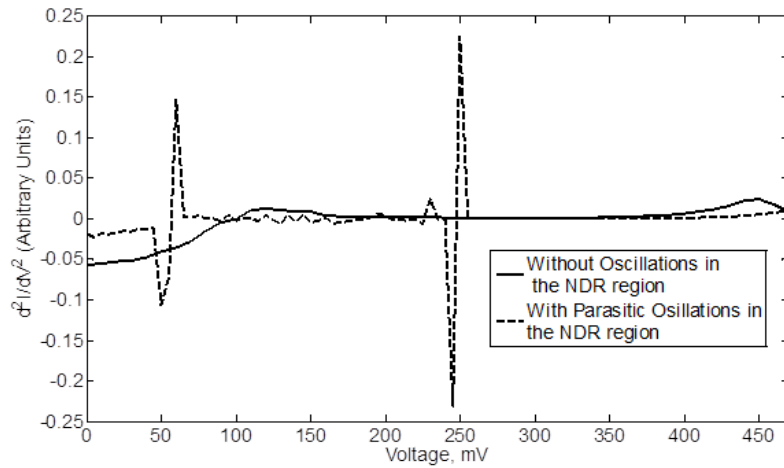
Figure 3.15: *Second derivative of the I-V curves of the 1N3712 diode showing the presence of oscillations (valleys followed by peaks) on the direct DC measurement in the 50 mV to 250 mV range of the NDR region [109].*
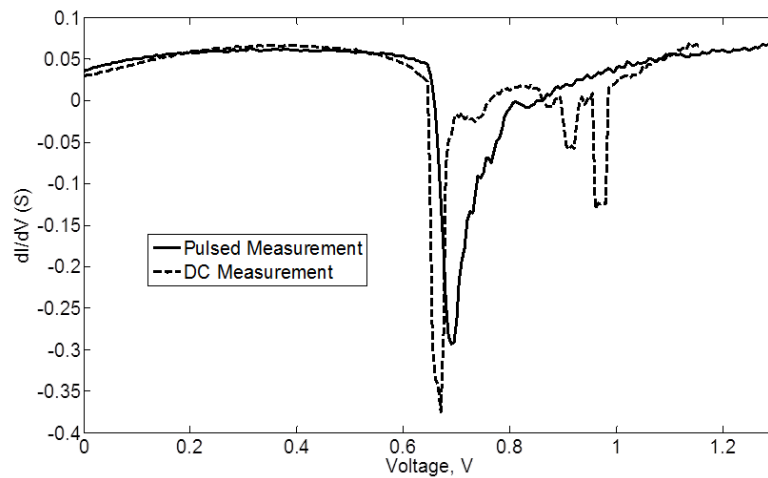
Figure 3.16: *First derivative of the I-V curves of the RTD showing the presence of oscillations (valleys) on the direct DC measurement in the 0.69 V to1.2 V range of the NDR region [109].*

sharp valleys immediately followed by sharp peaks.
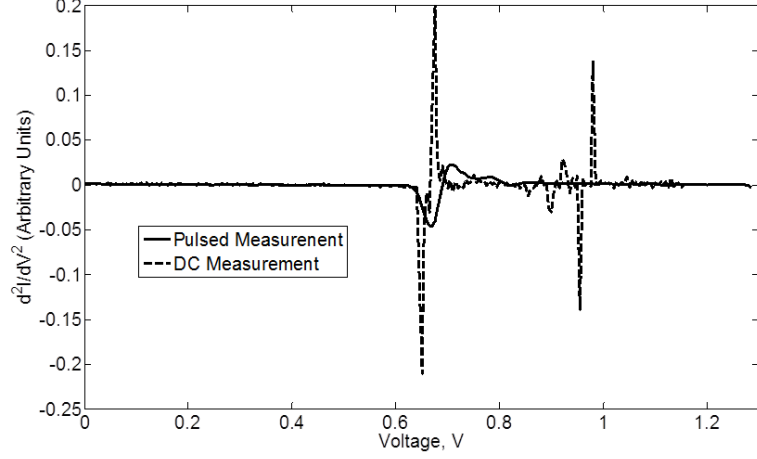
Figure 3.17: *Second derivative of the I-V curves of the RTD showing the presence of oscillations (valleys followed by peaks) on the direct DC measurement in the 0.69 V to 1.2 V range of the NDR region [109].*

3.4 Analytical TD/RTD Device Model

For the resonant tunnelling diodes, a physics-based analytical expression for the current-density voltage $(J - V)$ characteristic based on the Tsu-Esaki formula for the approximation of tunneling current through a super-lattice structure, obtained by summing the current density of each states over the occupied states multiplied by their transmission probability. It is expressed as [43] [62]

$$J = \frac{em^*\kappa T}{2\pi^2\hbar^3} \int_0^\infty T^*T \ln\left(\frac{1 + exp\left[(E_f - E_l)/\kappa T\right]}{1 + exp\left[(E_f - E_l - eV)/\kappa T\right]}\right) dE_l \qquad (3.6)$$

where J is the approximated current density, e is the electronic charge, m^* is the electron effective mass, $\hbar$ is the reduced Plancks constant, κ is Boltzmanns constant, T is the transmission amplitude, E_f is the Fermi energy and E_l the electron longitudinal energy which is parallel to the current flow. This equation can be used to create a current-density model for the device from the measured

43

data. The expression in physical quantities is represented in Equation 3.7 [110] as

$$J = \frac{em^*\kappa T\Gamma}{4\pi^2\hbar^3} \ln\left[\frac{1 + exp^{(E_F - E_r + eV/2)/\kappa T}}{1 + exp^{(E_F - E_r - eV/2)/\kappa T}}\right] \cdot \left[\frac{\pi}{2} + tan^{-1}\left(\frac{E_r - \frac{eV}{2}}{\frac{\Gamma}{2}}\right)\right] \quad (3.7)$$

where J is current density, V is voltage, e is the elementary charge, m^* is the electron effective mass, Γ is the resonance width which is the inverse lifetime of the resonance state , $\hbar$ is the reduced Plancks constant, κ is Boltzmanns constant, T is the transmission amplitude, E_F and E_r the Fermi band energy and the several resonant energy levels in the quantum well, respectively. Allowing the physical quantities to depart from their actual values to compensate for approximations gives

$$J_1(V) = A\ln\left[\frac{1 + exp^{(B - C + n_1 V)e/\kappa T}}{1 + exp^{(B - C - n_1 V)e/\kappa T}}\right] \cdot \left[\frac{\pi}{2} + tan^{-1}\left(\frac{C - n_1 V}{D}\right)\right] \quad (3.8)$$

Equation 3.8 models only the peak current density and the NDR region. To model the non-resonant current effect caused by thermal emission the current density expression for a diode in Equation 3.9 is used

$$J_2(V) = H\left(exp^{n_2 eV/\kappa T} - 1\right) \quad (3.9)$$

in Equations 3.8 and 3.9, A, B, C, D, H, n_1 and n_2 are unknown parameters in the non-linear equations. Thus, the total current density can be expressed as

$$J(V) = J_1(V) + J_2(V) \quad (3.10)$$

The measured RTD $I - V$ characteristics can be fitted to Equation 3.10 by an optimisation (fitting) process where the unknown parameters, A, B, C, D, H, n_1 and n_2 are determined. The parameters in the non-linear Equations 3.8 and 3.9 are used as unknowns in a custom equation in the curve fitting tool, $cftool$ in MATLAB. The start points for these parameters are chosen using values in Ref. [110], where a similar curve fitting analysis was performed for an InGaAs/AlAs based RTD and an InAs/AlSb/GaSb resonant inter-band tunneling diode. The curve fitting tool employs non-linear least squares method to create a fit between the measured and simulated current densities which requires successive iterative solutions to solve for the closest values of the unknowns (see Appendix A.1). Figure 3.18 shows the measured and modelled $I - V$ characteristics. Excellent agreement between the two has been achieved [109].
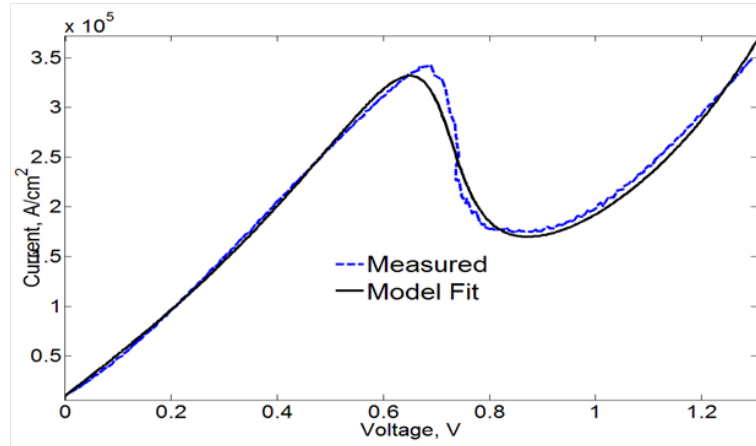
Figure 3.18: *Measured InP based RTD current density with non-linear least square fit from unknown parameters in Equations 3.8, 3.9 and 3.10 [109].*

The fitting parameters for the model of the InP based RTD are: $A = 104 A/m^2$, $B = 3.394 \times 10^{-3} eV$, $C = 6.108 \times 10^{-2} eV$, $D = 8.373 \times 10^{-3} eV$, $H = 2.151 \times 10^4 A/m^2$, $n_1 = 8.608 \times 10^{-2} eV$ and $n_2 = 7.274 \times 10^{-2} eV$.

3.5 Summary

Bias oscillation problems associated with static DC characterisation of tunneling devices such as RTDs and tunnel diodes have been described and the most common method of connecting a resistor in parallel to the device as a solution to this has also been described. Dynamic pulse current-voltage measurements have been used here as a new approach for measuring oscillation-free $I-V$ characteristics of tunnel diodes and RTDs. The technique involves monitoring the on-set of parasitic oscillations during measurement and taking the current-voltage values before the start of such oscillations. In addition, the measured $I-V$ characteristics of the RTD was modelled with a physics based analytical model through fitting.

In summary, accurate $I-V$ characterisation of a TD and RTD was demonstrated including the extraction of an analytical RTD model suitable for computer aided design. The next chapter considers the RF characterisation of RTDs.

Chapter 4

Microwave Frequency Characterisation of Resonant Tunneling Diodes

4.1 Introduction

Reliable and accurate small-signal equivalent circuit model of devices at high frequencies is needed for efficient microwave circuit designs such as amplifiers and oscillators. For resonant tunneling diodes and tunnel diodes, this is especially needed in the region of interest, the negative differential resistance (NDR) region. High frequency characterization of the NDR region of RTDs is however usually not possible due to parasitic bias oscillations. This section describes the high frequency measurements and microwave frequencies measurement set-up suitable for on-wafer characterisation of resonant tunnelling diodes. Also presented is an equivalent circuit model, extracted from the measured data for the RTD in the positive differential resistance (PDR) region. The values of the extracted parameters from the measurements can be used in the optimisation of the device

47

technology, e.g. the contact resistance should always be minimised, and in circuit design, the device capacitance can be used to estimate the oscillation frequency in an oscillator design.

4.2   High Frequency Measurements

As mentioned in section 4.1, high frequency characterisation of RTDs in the NDR region is quite difficult due to instability caused by parasitic oscillations. However, in a 50 Ω system such as in a vector network analyzer (VNA), and for differential conductance less than $0.02 = 1/50\ S$ (which is usually the case in small sized devices [111]), or in sections of the current-voltage characteristics of larger devices, these parasitic oscillations are usually absent because of the small negative conductance eliminates bias line instability and high frequency characterisation can be carried out [112][113].

The two basic circuit models used in the study of nonlinear oscillations in RTDs are the lead inductor model and the quantum-inductor model [113][114]. The lead inductor model is a variation of the Esaki tunnel diode model [115]. It has the nonlinear circuit element and the capacitance connected in parallel configuration and this is then arranged in series with the inductance and resistance. However, studies have shown that due to the correlation of the Fermi energy level at the source and the resonant energy levels due to self consistency of the potential the charge stored in the quantum well, the quantum-inductor model which has the inductive delay element in series with the nonlinear circuit element together in parallel with the capacitance is a better model for the study of nonlinear oscillations in RTDs [114][116][117].

Figure 4.1 shows the small signal equivalent circuit of the InP-based RTD made

from $In_{0.53}Ga_{0.47}As/AlAs$ which was characterised for DC in Chapter 3. The
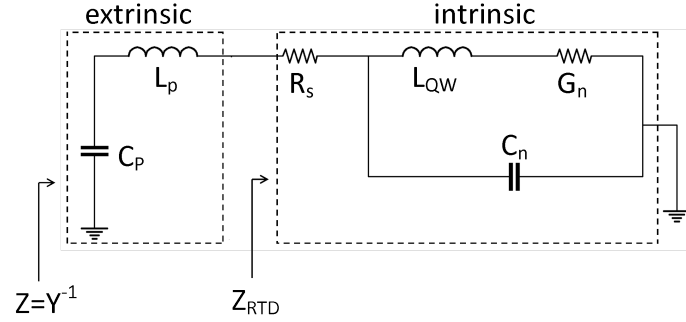
Figure 4.1: *Small-signal equivalent circuit of RTD, with the intrinsic and extrinsic parameters shown [116].*

equivalent circuit is made up of both the intrinsic (quantum-inductor model) and extrinsic parameters. The intrinsic parameters consist of the quantum well inductance, L_{QW}, with the differential conductance, G_n in series, and these parallel with the device capacitance, C_n. These are arranged in series with the device series resistance, R_s [116]. The extrinsic parasitic parameters results from the pad inductance, L_P and the pad capacitances, C_P. Z is the impedance of the RTD with the pads and Z_{RTD} is the impedance of the RTD without the pads. Figure 4.2 shows the cross-section of an RTD structure with the equivalent circuit elements in their locations.

4.2.1 Microwave Frequencies Characterisation

Characterisation was carried out in the microwave frequencies range at several bias points in the first and second positive differential resistance regions and the negative differential resistance region. In the NDR region, no device stabilization method was employed. A diagram of the measurement set up is shown in Figure 4.3 and it consists of the Keysight technology B1500 to supply bias voltage and a Keysight E8361A vector network analyzer (VNA) which was used to measure
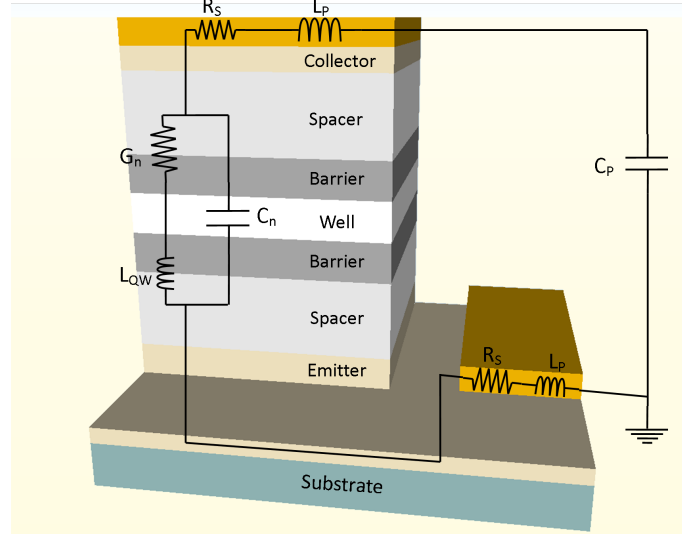
Figure 4.2: *Small-signal parameters shown in a simple RTD layer structure under bias condition.*

the one port scattering parameters, S_{11}, for the chosen frequency range and bias points. The bias-T is provided through the VNA. Figure 4.4 shows an image of the RTD device under test (DUT). The bias voltages for the PDR and NDR regions of the RTD $I - V$ are provided by the Keysight Technologies B1500A device parameter analyser. The signal from the VNA and the bias voltages are both fed to the device through a $100\mu m$ co-planar ground-signal-ground (GSG) probe using a bias tee.

The frequency span for the measurements was 10 MHz to 67 GHz, and port power was -17 dBm. On-wafer calibration was done by short-open-load-thru (SOLT) calibration technique to eliminate errors and move the measurement reference point to the tips of the probe [118]. The impedance standard substrate from Cascade Microtech provided the short standard, thru standard and the 50 Ω precision load standard. The open standard was achieved by raising the probes in air.
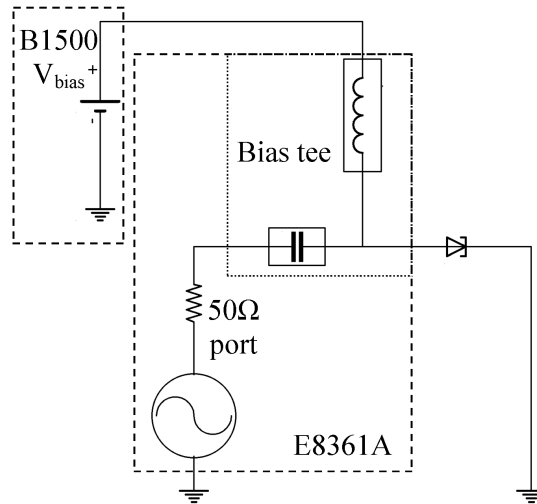
Figure 4.3: *Measurement set-up.*
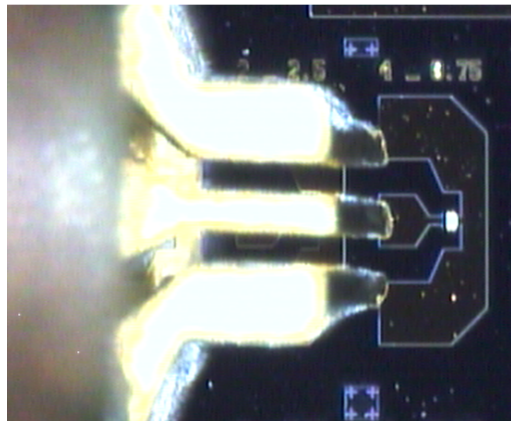
Figure 4.4: *Image of an RTD device under test.*

4.2.2 Extraction of the RTD Equivalent Circuit Elements

The effects of the parasitic extrinsic parameters, L_p and C_p in Figure 4.1 have to be excluded after measurements for accurate high frequency characterisation. This is achieved by including shorted and open dummy pad test structures on the wafer. The open dummy pad test structure is used to characterise the parallel parasitic component, C_p and the short dummy pad test structure is used to

characterise the series parasitic component, L_p [119]. Figure 4.5 shows a micrograph of the RTD device including open and short pad test structures used for de-embedding the effects of the pad inductance and capacitance.

(a)   **(b)**   **(c)**
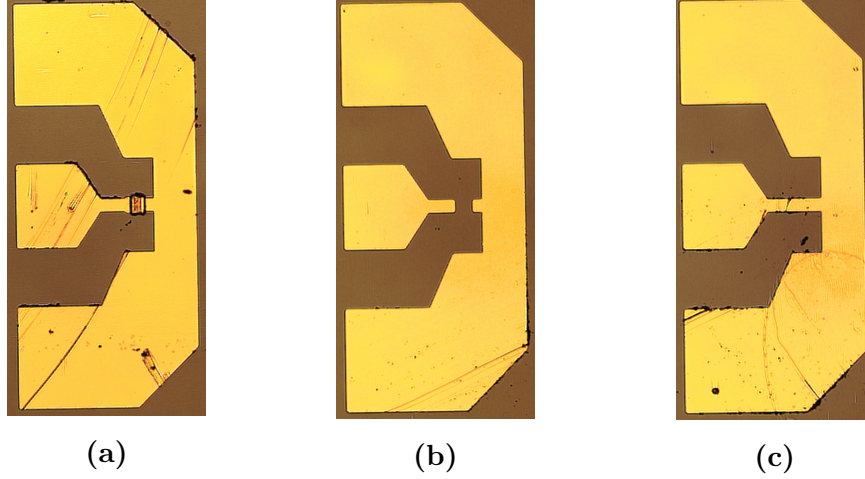
Figure 4.5: *Micrographs of (a) the RTD, (b) open dummy pad and (c) short dummy pad used for de-embedding.*

The measured S-parameters are first converted to Z-parameters from the relationship [31]

$$S_{11} = \Gamma = \frac{Z - Z_o}{Z + Z_o} \tag{4.1}$$

where Γ is the reflection coefficient and Z_o is the 50Ω characteristic impedance of the measurement system, by

$$Z = Z_o \cdot \frac{1 + S_{11}}{1 - S_{11}} \tag{4.2}$$

To remove the parallel parasitic component, C_p, shown in the small signal equivalent circuit in Figure 4.1, the Y-parameters, (Z^{-1}), of the measured open pad

test structure Y_{open}, is subtracted from the measured Y-parameters of the device, Y_{meas} by

$$Y_{parallel} = Y_{meas} - Y_{open} \qquad (4.3)$$

where $Y_{parallel}$ is the admittance without the parallel parasitic components. Since the series parasitic component, L_p is embedded along with parallel components in the measured short pad test structure, the impedance of the series component, Z_{series} is found by

$$Z_{series} = (Y_{short} - Y_{open})^{-1} \qquad (4.4)$$

where Y_{short} is the admittance of the measured short pad test structure. The actual RTD Z-parameters is then found from

$$Z_{RTD} = ((Y_{parallel}^{-1}) - Z_{series}) \qquad (4.5)$$

A schematic model of the intrinsic small-signal parameters, R_s, L_{QW}, G_n and C_n was created in the Keysight Advanced Design System (ADS) software for optimisation. The optimisation tool is used to extract the values of the small signal parameters by fitting the measured Z_{RTD} parameters over the entire frequency range. The ADS gradient optimiser was used which calculates the difference or error between the simulated and measured Z parameters [120]. The error function, EF determines the difference between the simulation and the measurement for all the frequencies. The difference is squared and multiplied by a weighting factor if required. This can be expressed in a generalised form as

$$EF = \sum_{frequency} W_i \times |simulated_i - measured_i|^2 \qquad (4.6)$$

where W_i is a weighting factor at each frequency increment. The least square error function at each point (frequency) is evaluated individually. The magnitude of these errors are squared, summed and averaged over the entire frequency range to determine the least square error function. The gradient information of the error function indicates the direction to move the set of parameter values, (R_s, G_n, C_n and L_{QW}) until the error function is minimised. The optimisation goals were set to match the real and imaginary parts of the measured Z_{RTD} over the measured frequency range. The initial values of R_s, C_n and L_{QW} used in the circuit simulation for optimisation were 15 Ω, 50 fF and 0.5 nH respectively. These were estimated from the device structure (C_n), the literature (L_{QW}) [121] and the IV characteristics (R_s). The values of the differential conductance $-G_n$ was fixed initially for each bias point using values derived in Figure 3.16 from the oscillation free InP based RTD $I - V$ measurements in Chapter 3.

4.3 Experimental Results

The S-parameters for the resonant tunneling diode were measured with bias voltages at 0.5 V and 1.1 V in the positive differential resistance (PDR) regions and 0.65 V and 0.7 V in the negative differential resistance (NDR) region. Figures 4.6 to 4.7 shows the real and imaginary parts of the de-embedded S-parameters at 0.5 V, 0.65 V, 0.7 V and 1.1 V, respectively [109]. The measurements of the RTD when biased in the PDR regions are shown in Figures 4.6 and 4.7. The real and imaginary impedance parts of the measured S_{11} parameters in Figures 4.6 and 4.7 are seen to be generally smooth, however, the real and imaginary impedances

becomes erratic when biased in the NDR region as seen in Figures 4.8 and 4.9 due to parasitic bias oscillations. It should be noted, that beyond 36 GHz, the traces are smooth and the data may have been good for extraction of the small signal equivalent circuit elements. This is because the oscillation period of the incident signal from the network analyser is quite shorter at higher frequencies than the oscillation period of the parasitic bias oscillations hence it has minimal or no effects on the measurements above 36 GHz [117][122]. However, the extraction of the small signal equivalent circuit was conducted only for the PDR region.
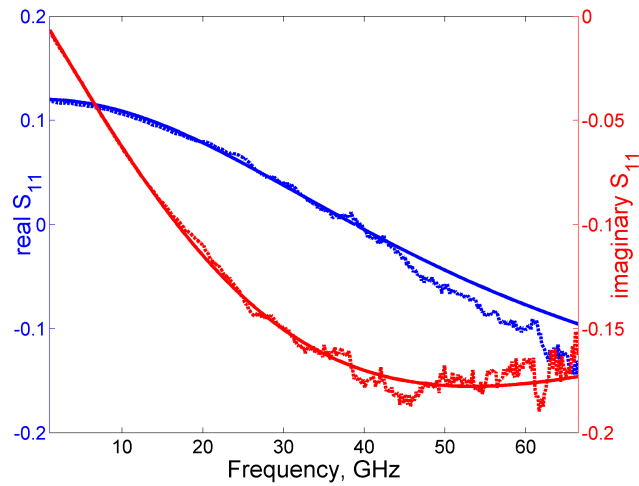
Figure 4.6: *Comparison of measured (dotted-lines) real and the imaginary parts and simulated (solid-line) real and the imaginary parts (from extracted parameters) of the S_{11} parameters at 0.5 V for the first PDR region [109].*

The simulated results from the extracted parameters show good agreement when compared with the measured data in the PDR region (Figures 4.6 and 4.7). The extracted small signal parameters, including the conductance, series resistance, inductance and capacitance of the RTD when biased at 0.5 V and 1.1 V are shown in Table 4.1.
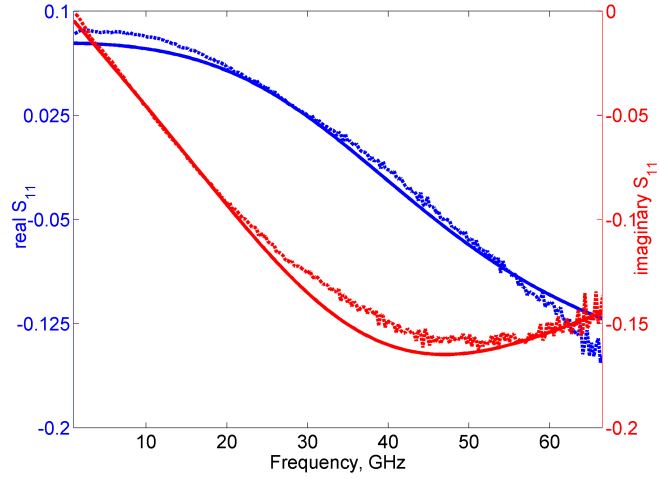
Figure 4.7: *Comparison of measured, (dotted-lines) real and the imaginary parts and simulated, (solid-line) real and the imaginary parts (from extracted parameters) of the S_{11} parameters at 1.1 V for the second PDR region [109].*
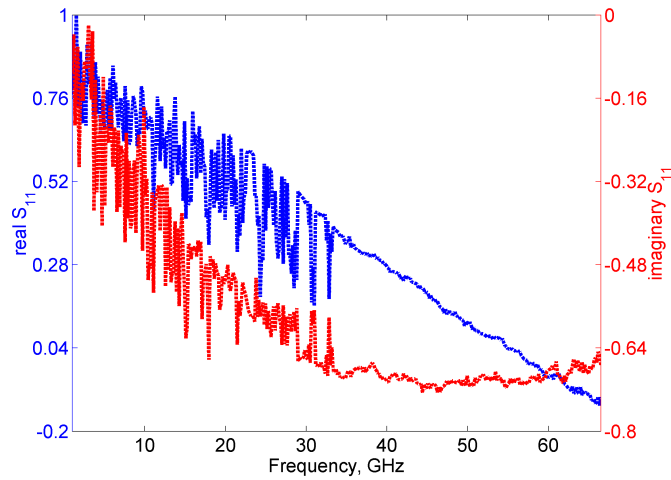
Figure 4.8: *Measured real and the imaginary parts of the S_{11} parameters at 0.65 V for the NDR region. Data beyond about 33 GHz seems smooth and may be useful for equivalent circuit extraction.*
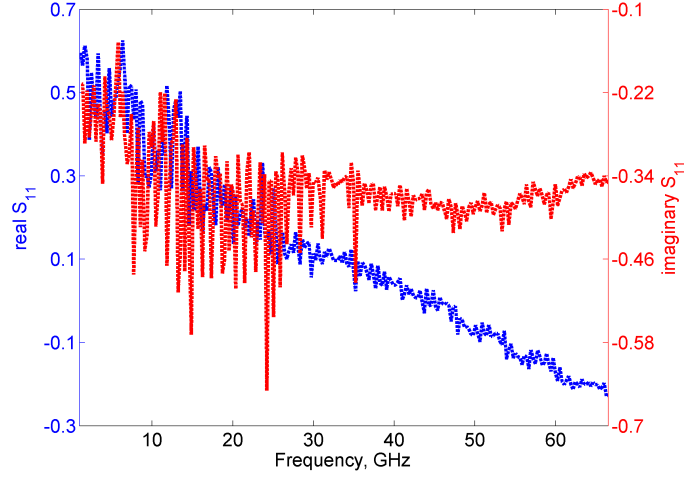
Figure 4.9: *Measured real and the imaginary parts of the S_{11} parameters at 0.7 V for the NDR region. Data beyond about 36 GHz seems smooth and may be useful for equivalent circuit extraction.*

Table 4.1: Extracted small-signal equivalent parameters in the PDR regions

Bias Voltage(V)	Series Resistance $R_s(\Omega)$	Inductance $L_{QW}(pH)$	Conductance $G_n(mS)$	Capacitance $C_n(fF)$
0.5	32	26	32	160
1.1	34	54.5	40	248

4.4 Summary

High frequency characterisation of the resonant tunneling diode has been presented with de-embedding carried out to remove the effects of the pad parasitics. A small signal model of the intrinsic parameters has also been provided at bias points in the PDR region. Accurate small-signal model extraction of the RTD when biased in the negative differential resistance region could not be carried out due to the effects of bias oscillations. Future work should devise methods of oscillation-free microwave characterisation of RTDs biased in the NDR region.

Chapter 5

Tunneling Diode Based Oscillator Design

5.1   Introduction

As described in Chapter 1, devices that exhibit negative differential resistance (NDR) can be used to realise RF sources. Tunnel diodes and resonant tunneling diodes (TD/RTD)-based oscillators can be used to provide compact solid-state RF sources operating at room temperature. This chapter describes and presents the tunnel diode based oscillator topology and a proposed novel power combining circuit topology to double the output power from a single oscillator circuit. The technique is a self-synchronized oscillator that combines the output powers from two coupled individual oscillators to a single load. Each of the oscillators is individually biased. The proposed circuit is realised in micro-strip hybrid circuit technology using tunnel diodes. The design method is applicable to RTDs for higher frequency oscillators.

5.2 DC Stability and Maximum Power

5.2.1 DC Stability and RF Oscillations

As described in Chapter 3, parasitic bias oscillations occur in the NDR region due to the inductance L_b of the biasing lines/cables. This places a constraint on the maximum output power that can be achieved using TD/RTD device-based oscillators as the output RF power is distributed between the bias oscillations and the design frequency [123]. The parasitic bias oscillations can be suppressed if the criteria in Equation 5.1 is satisfied [71][96][97].

$$R_{st} < \frac{1}{G_n} \tag{5.1}$$

Since $-G_{n(max)} = a = (3\Delta I)/(2\Delta V)$ (see chapter 2, section 2.2), R_{st} can also be expressed as

$$R_{st} < \frac{2\Delta V}{3\Delta I} \tag{5.2}$$

in terms of the device IV characteristics, namely the peak-to-valley voltage and current difference, ΔV and ΔI respectively.

5.2.2 Maximum RF Oscillator Output Power

In this section, the theoretical RF output power of a single device TD/RTD oscillator is derived [68][70][97][124]. Figure 5.1 shows the RF equivalent circuit of a TD/RTD device-based oscillator. The TD/RTD is represented as a large signal model with the device's self capacitance C_n and a voltage controlled current source $i = f(v)$, where $f(v) = -av + bv^3$. Assuming v is a sinusoidal signal, $v = V cos(\omega t)$

where V is the amplitude of the signal and ω is the angular frequency given by $\frac{1}{\sqrt{LC_n}}$.
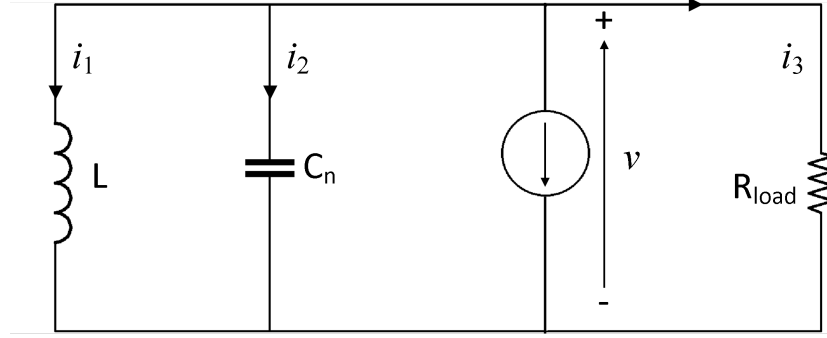
Figure 5.1: *RF equivalent circuit a TD/RTD based oscillator with the TD/RTD represented by self-capacitance C_n and voltage controlled current source $i = f(v)$. L represents the resonating inductor and R_{load} is load resistance.*

From Kirchhoff's current law, the currents in the circuit can be expressed as $i_1 + i_2 + i_3 + i = 0$, or

$$\frac{1}{L} \int v\,dt + C_n \frac{dv}{dt} + vG_{load} + (-av + bv^3) = 0 \tag{5.3}$$

where G_{load} is the load conductance $(G_{load} = 1/R_{load})$ [68][70]. Equation 5.3 can be re-arranged after differentiating with respect to time to give

$$LC_n \frac{d^2v}{dt} + L(G_{load} - a + 3bv^2)\frac{dv}{dt} + v = 0 \tag{5.4}$$

The instantaneous power dissipated by the load is given as

$$P_{load} = v^2 G_{load} = (V cos(\omega t))^2 G_{load} \tag{5.5}$$

The average power dissipated by the load is

$$P_{load}(Average) = G_{load}\frac{V^2}{2} \tag{5.6}$$

by integrating Equation 5.5 over one period, the power generated by the TD/RTD can be expressed as

$$P_{NDR\ device} = -iv = av^2 - bv^4 \tag{5.7}$$

which, on integrating over one period, results in the average power generated by the NDR device to be expressed as

$$P_{NDR\ device}(Average) = \frac{aV^2}{2} - \frac{3bV^4}{8} \tag{5.8}$$

As $P_{NDRdevice}$ equals P_{load}, V is given by

$$V = 2\sqrt{\frac{G_n - G_{load}}{3b}} \tag{5.9}$$

and the average power dissipated by the load, from substitution Equation 5.9 into $P_{load}(Average)$ is

$$P_{load} = 2(G_n - G_{load})\frac{G_{load}}{3b} \tag{5.10}$$

and when $G_{load} = 1/2(G_n)$, the maximum power to the load (obtained by differentiating Equation 5.10 and equating to zero) is given by

$$P_{Maximum} = \frac{G_n^2}{6b} = \frac{3}{16}\Delta I \Delta V \tag{5.11}$$

Equation 5.11 gives an estimate of the maximum RF power that can be delivered by a TD/RTD.

5.3 Hybrid Tunnel Diode (TD) Oscillator Designs

5.3.1 Single TD Oscillator Design

The schematic circuit of a single hybrid oscillator is shown in Figure 5.2a [125]. V_{bias} represents the bias voltage applied to the device with R_b and L_b representing the resistance and inductance of the biasing cables, respectively. R_{st} is connected in parallel to the TD to suppress low frequency bias oscillations and C_{st} is a decoupling capacitor which acts as an RF short to ground to avoid RF power been dissipated by R_{st}. C_{st} will act as a short circuit at the desired frequency if

$$\frac{1}{2\pi f_o C_{st}} < 0.1\Omega \tag{5.12}$$

where f_o is the desired oscillation frequency. R_{st} has to satisfy Equation 5.2 to suppress the bias oscillations. DC blocking capacitor C_{dc} is used to prevent DC bias voltage reaching the load R_{load} and is chosen to act as an RF short circuit at the oscillation frequency. Figure 5.2b shows a high frequency equivalent circuit of the single device oscillator with the TD represented by the negative differential conductance, $-G_n$ and the device self capacitance, C_n [125].

The frequency of oscillation f_o can be derived when the suspectance of the circuit in Figure 5.2b is set to zero, i.e.,

$$2\pi f_o C_n - \frac{1}{2\pi f_o L} = 0 \tag{5.13}$$

or

$$f_o = \frac{1}{2\pi\sqrt{LC_n}} \tag{5.14}$$

(a)

(b)
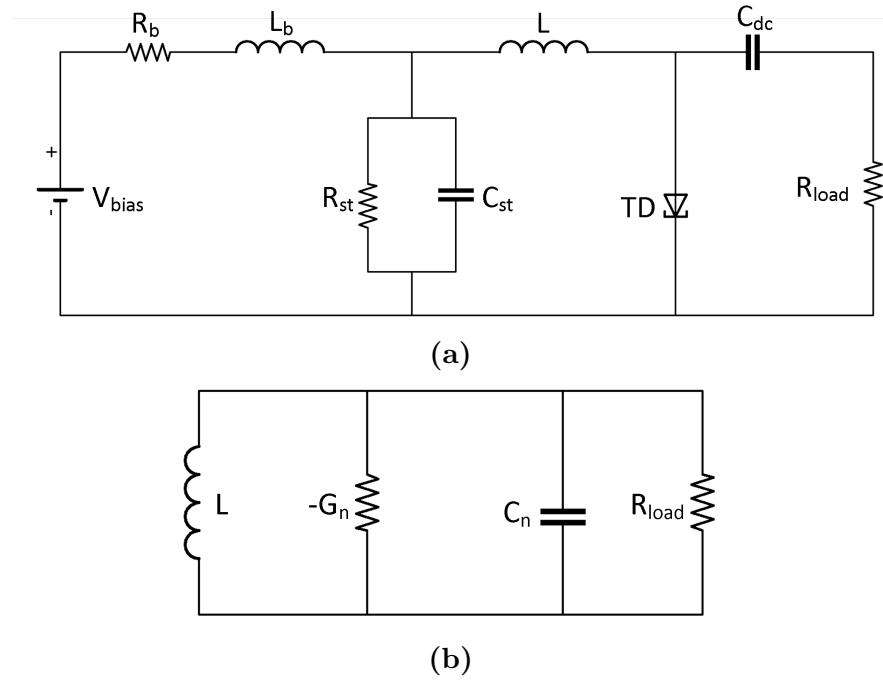
Figure 5.2: *(a) Single TD device oscillator topology biased with V_{bias}, R_b and L_b representing the bias cable inductance and resistance, respectively. Shunt resistor R_{st} is for suppressing bias oscillations. Decoupling capacitor is C_{st}. The load resistance is R_{load} and L is the resonating inductance. (b) Single TD device oscillator high frequency equivalent circuit. Here, the TD is represented by the device self-capacitance C_n and the negative conductance $-G_n$ [125].*

5.3.2   Coupled Tunnel Diode Oscillators

One of the ways of improving the output power of tunnel diode (TD) and resonant tunneling diode (RTD) oscillators is the use of two active devices rather than one [68][71]. Figure 5.3 shows an example of a circuit topology using this approach. The circuit contains two tunnel diodes, TD1 and TD2, individually biased and stablised with resistors R_{st1} and R_{st2}. The inductances and resistances of the biasing lines are represented by L_{b1}, L_{b2} and R_{b1} and R_{b2} respectively. C_{st1} and C_{st2} are the decoupling capacitors. R_{load} is the load resistance and L, is the resonating inductance. The frequency of oscillation of this circuit can be represented by

$$f_o = \frac{1}{2\pi\sqrt{(C_{n1} + C_{n2})L}} \tag{5.15}$$

Implementing this design for an oscillator with RTDs as the active devices, the output power of -0.7 dBm at 28.7 GHz was reported [68], and for TDs as the active devices, an output power of -7.83 dBm at 437 MHz was reported. This was 3 dB higher compared to a single TD active device oscillator design with measured output power of -10.17 dBm at 618 MHz [71]. However, the frequency of oscillation f_o, for the circuits using two TD or RTD devices is reduced compared to that of the single TD or RTD device based oscillator due to increased total device self-capacitances.

To keep the frequency of oscillation f_o high as for a single TD oscillator while increasing power, a new power combining approach is needed. Here two individual oscillators made up of single tunnel diodes are coupled to allow for the combining of their power into a single load. The coupled oscillator topology shown in Figure 5.4a employs the single TD oscillator design shown in Figure 5.2 [125].

(a)

(b)
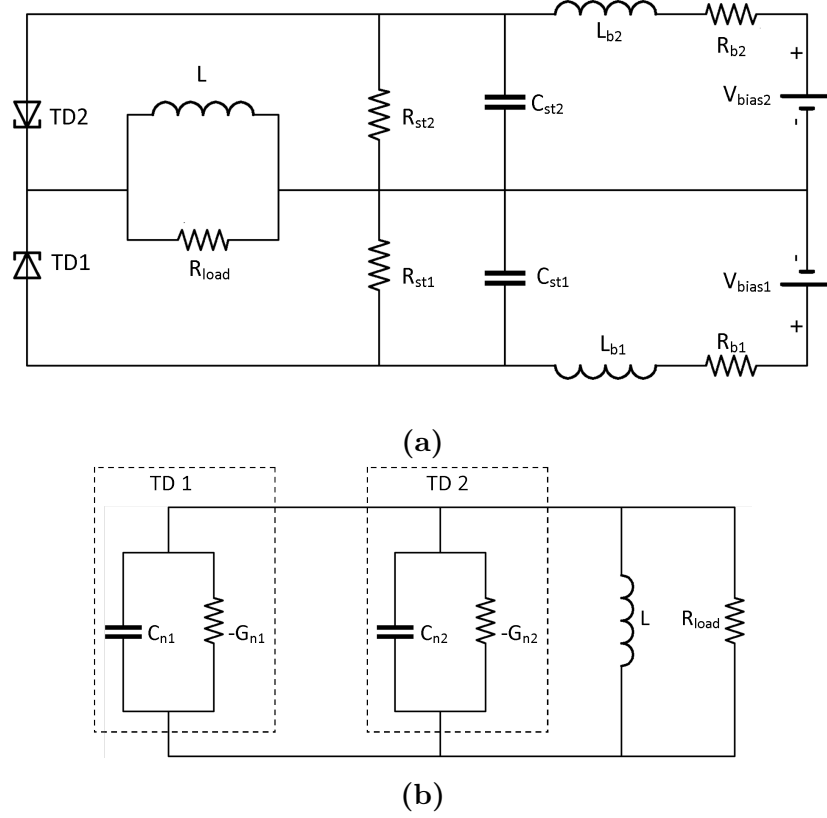
Figure 5.3: *(a)Double TD device oscillator topology, (b) High frequency equivalent circuit of double device oscillator topology where the TD devices are represented by the capacitances, C_{n1} and C_{n2} and the negative conductances, $-G_{n1}$ and $-G_{n2}$ [68].*

The individual oscillators are biased individually. Capacitive coupling of both oscillators through DC blocks C_{dc1} and C_{dc2} allows the individual oscillations to become synchronized and the output RF power delivered to the load R_{load}. The RF equivalent circuit of the synchronized oscillator is shown in Figure 5.4b, where TD1 and TD2 are replaced with the negative differential conductances, $-G_{n1}/-G_{n2}$ and the device self capacitances, C_{n1}/C_{n2} [125].

(a)

(b)
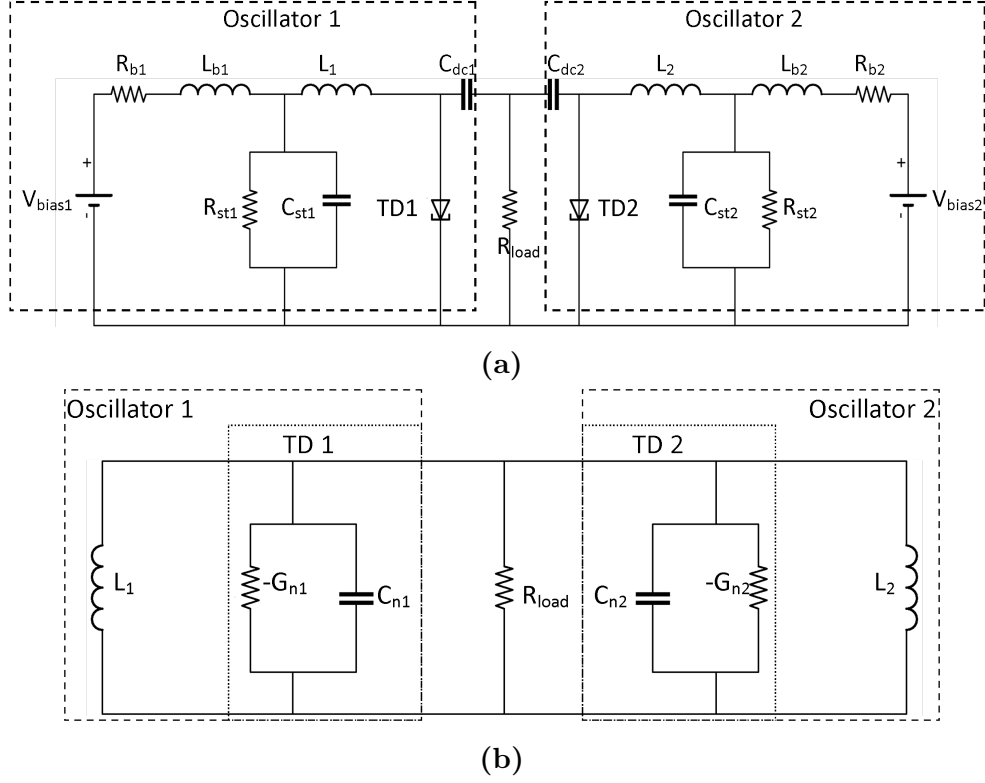
Figure 5.4: *(a) Power combining of two TD device oscillators biased and decoupled independently with the power collected at a single load R_{load}. (b) Small signal equivalent circuit of coupled tunnel diode oscillators with the devices represented by the self-capacitances C_{n1} and C_{n2} and the negative conductances $-G_{n1}$ and $-G_{n2}$ [125].*

The frequency of oscillation can be expressed as

$$f_o = \frac{1}{2\pi\sqrt{(C_{n1} + C_{n2})\left(\frac{1}{\frac{1}{L_1} + \frac{1}{L_2}}\right)}} \tag{5.16}$$

where C_{n1} and C_{n2} are the device self-capacitances which are in parallel and L_1 and L_2 are resonating inductances for oscillator 1 and oscillator 2 in parallel. This reduces to Equation 5.14 for $L_1 = L_2 = L$ and $C_{n1} = C_{n2} = C_n$. Thus the frequency of oscillation for the coupled oscillators is the same as for a single device oscillator.

5.4   Experimental Results

Both the single TD oscillator and the coupled oscillators were realised using commercially available $1N3717$ tunnel diodes. The $I - V$ characteristics of the $1N3717$ tunnel diode is shown in Figure 5.5. It has a difference in peak to valley current, ΔI and voltage ΔV of $4\ mA$ and $250\ mV$, respectively.
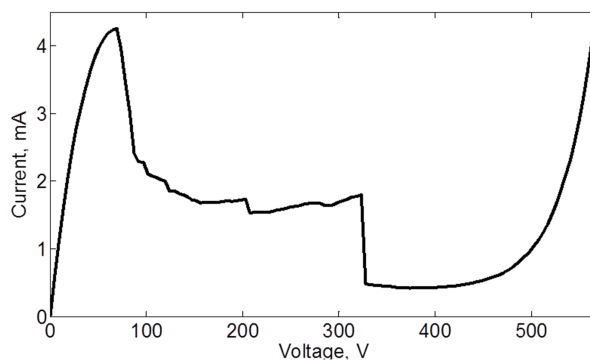
Figure 5.5: *I-V characteristics of 1N3717 tunnel diode.*

In this project, a micro-strip line was used to achieve the desired inductance. The procedure for designing an inductor using a short circuited micro-strip line is described here. The micro-strip line is a transmission line consisting of a strip of conductor and a ground plane separated by a substrate.

Figure 5.6 shows a cross-sectional diagram of a typical micro-strip transmission line. W, is the width of the conductor, t is the thickness of the conductor, l is the conductor length and h is the height of the substrate. The relationship between the ratio of the width of the conductor, W to the height of the substrate, h, the dielectric constant of the substrate, ε_r and the characteristic impedance of the line, Z_0, is given by [31][126]
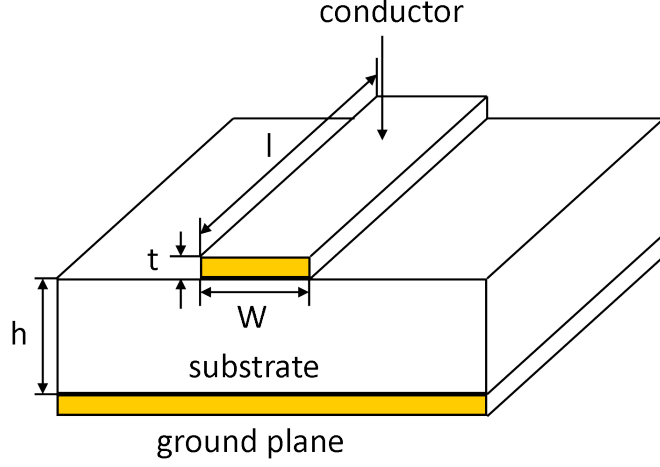
Figure 5.6: *Micro-strip transmission line structure showing ground plane and conductor separated by substrate.*

$$\frac{W}{h} = \frac{2}{\pi} \left\{ B - 1 - \ln(2B - 1) + \frac{\varepsilon_r - 1}{2\varepsilon_r} \left[\ln(B - 1) + 0.39 - \frac{0.61}{\varepsilon_r} \right] \right\} \qquad (5.17)$$

for $W/h \geq 2$

$$\frac{W}{h} = \frac{8e^A}{e^{2A} - 2} \qquad (5.18)$$

for $W/h \leq 2$. Where

$$A = \frac{Z_0}{60} \sqrt{\frac{\varepsilon_r + 1}{2}} + \frac{\varepsilon_r - 1}{\varepsilon_r + 1} \left(0.23 + \frac{0.11}{\varepsilon_r} \right) \qquad (5.19)$$

and

$$B = \frac{377\pi}{2Z_0\sqrt{\varepsilon_r}} \qquad (5.20)$$

for a transmission line of length l the input impedance Z_{in}, is expressed in terms of the characteristic impedance, Z_0 and the load impedance Z_L as [126].

$$Z_{in} = Z_0 \frac{Z_L + jZ_0 \tan(\beta l)}{Z_0 + jZ_L \tan(\beta l)} \qquad (5.21)$$

β is the propagation constant and it is $2\pi/\lambda$. λ is the wavelength on a micro-strip line and it is given by $\lambda = \dfrac{c}{f\sqrt{\varepsilon_{eff}}}$, where c is the speed of light, f is the frequency

and ε_{eff} is the effective dielectric constant and it is

$$\varepsilon_{eff} = \frac{\varepsilon_r + 1}{2} + \frac{\varepsilon_r - 1}{2} \left[\left(1 + 12\frac{h}{W} \right)^{-0.5} + 0.04 \left(1 - \frac{W}{h} \right)^2 \right] \tag{5.22}$$

for $W/h \leq 1$, and

$$\varepsilon_{eff} = \frac{\varepsilon_r + 1}{2} + \frac{\varepsilon_r - 1}{2} \left(1 + 12\frac{h}{W} \right)^{-0.5} \tag{5.23}$$

for $W/h \geq 1$. For a shorted circuited micro-strip line ($Z_L = 0$), Equation 5.21 is reduced to

$$Z_{in} = jZ_0 \tan \beta l \tag{5.24}$$

and the relationship between $Z_{in}(sc)$ and the inductance of the line, L is

$$Z_{in} = j\omega L \tag{5.25}$$

where ω is the angular frequency, $2\pi f$. Figure 5.7 shows a shorted transmission line
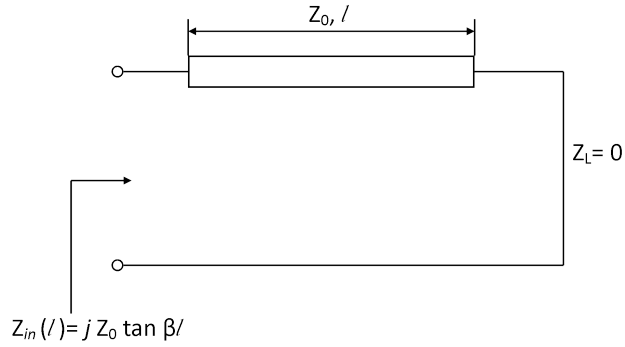
Figure 5.7: *Short-circuited transmission line.*

Capacitors, C_{st} for the single TD oscillator and for the coupled oscillators, C_{st1} and C_{st2} were used to provide short circuit load for the micro-strip lines. The inductances L, for the single TD oscillator and L_1 and L_2 for the coupled TD oscillators were realised using 11 *mm* long micro-strip lines of 1.8 *mm* width

and substrate height of 762 μm realised on a Rogers laminate substrate having dielectric constant, ε_r, of 3.48. This gives a total series inductance of $\sim 5nH$ (4.3nH from microstrip line and 0.5nH from the packaged 1N3717 tunnel diode [127]). This inductance value along with the 1N3717 self capacitance C_n of 13 pF forms the resonant circuits and these values keep the fundamental frequency of oscillation f_o around 600 MHz.

The decoupling circuits were implemented on the same substrate using 2 nF multi-layered ceramic capacitors based on Equation 5.12 for C_{st}, C_{st1} and C_{st2}. Using Equation 5.2, the value of the stabilising resistors was 10 Ω for R_{st}, R_{st1} and R_{st2}. Figure 5.8 shows a photograph of the coupled tunnel diode oscillators showing the DC blocking capacitors C_{dc1} and C_{dc2} with capacitance values of 3 nF each [125].
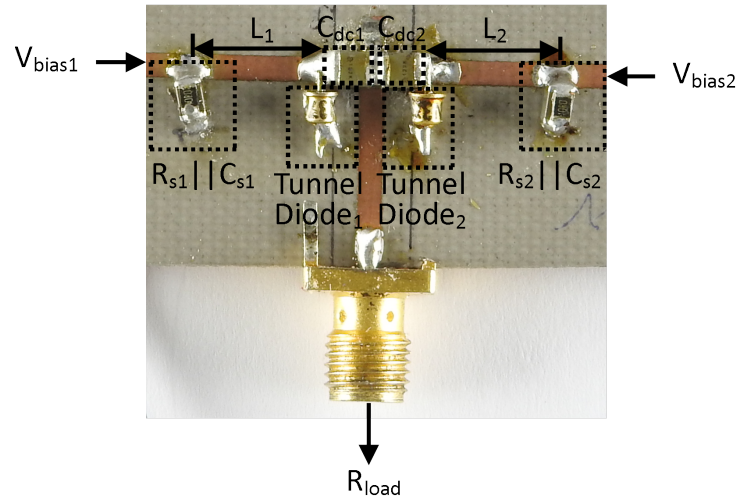
Figure 5.8: *Photograph of coupled tunnel diode oscillators realised in hybrid microstrip technology [125].*

To measure the RF output power and oscillation frequency of the oscillators, a spectrum analyser was used. The spectrum analyser used for the measurements was the Keysight E4448A spectrum analyser which has an upper frequency limit

of 50 GHz. For the results presented in Figures 5.9 and 5.10, the DC bias was provided to the circuits using a Keysight B2902A precision source/measure unit and the circuit was connected with a coaxial cable from the SMA connector to the spectrum analyser [125]. Figure 5.9 shows the measured output power of the single TD device oscillator at its fundamental frequency of oscillation, while Figure 5.10 shows the measured output power at the fundamental oscillation frequency for the coupled TD oscillator. The coupled tunnel diode oscillators has a highest measured RF output power of -6.42 dBm (0.23 mW) at 716.2 MHz at 265 mV bias voltage, which is roughly double the highest measured output power from the single oscillator of -9 dBm (0.13 mW) at 250 mV bias. The variation in the fundamental frequencies of oscillations of the single and coupled oscillators is attributed to slight variations in the inductance values of L, L_1 and L_2 realised using lengths of micro-strip lines.
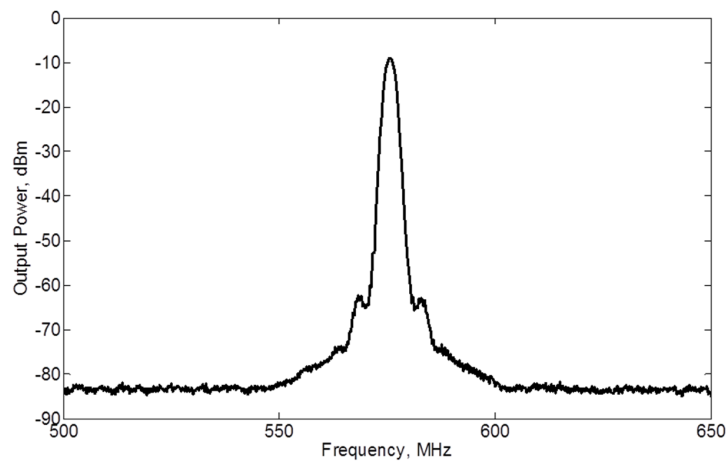
Figure 5.9: *Measured spectrum of the fundamental frequency of oscillation of the single 1N3717 tunnel diode oscillator biased at 250 mV with -9 dBm output power at 575.7 MHz [125].*

Figure 5.11 shows the oscillator output power as a function of bias. For the single tunnel diode oscillator, the lowest output power is between -23 dBm at 90 mV
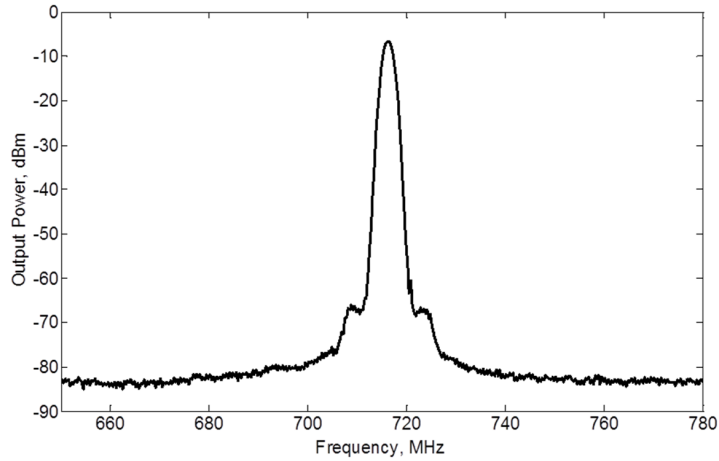
Figure 5.10: *Measured spectrum of the fundamental frequency of oscillation of the coupled 1N3717 tunnel diode oscillators biased at 265 mV with -6.42 dBm output power at 716.2 MHz [125].*

bias and the maximum output power is -9 *dBm* at 250 *mV*. For the coupled oscillators, the measured output power depended on the bias voltage and it was -17 *dBm* at 90 *mV* and the maximum measured power is -6.42 *dBm* when 265 *mV* bias is applied.
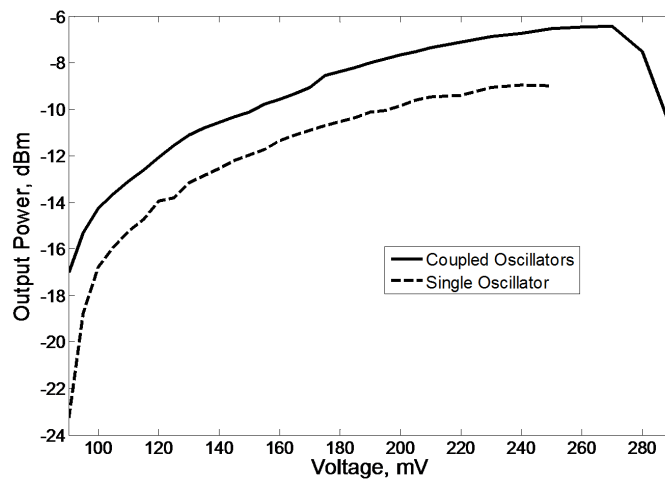
Figure 5.11: *Measured RF output power of single and coupled oscillators as a function of bias voltage.*

Figure 5.12 shows the fundamental oscillation frequency as a function of the applied bias voltage. For the single device oscillator, this is between 573 MHz and 590 MHz depending on the bias voltage and between 700 MHz and 720 MHz for the coupled oscillators.
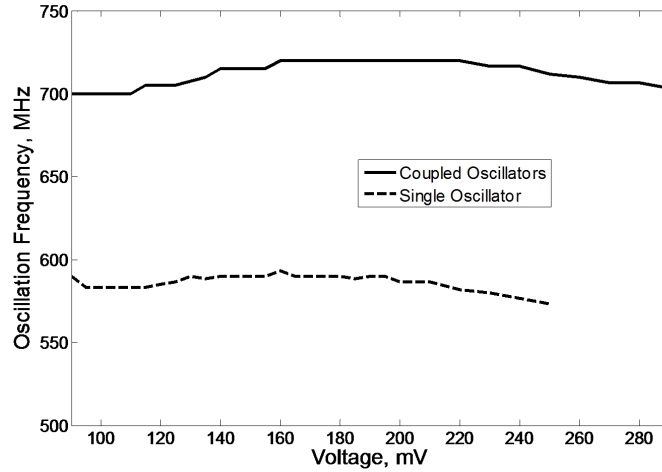
Figure 5.12: *Fundamental frequency of oscillation of single and coupled oscillators as a function of bias voltage.*

5.4.1   Phase Noise

Phase noise, which is the noise caused by short term variations or fluctuations that occur in a signal caused by time-domain instabilities, is an important parameter in oscillator design. An ideal signal in the frequency domain, can be expressed as [128] [129]

$$V(t) = A_o sin 2\pi f_o t \qquad (5.26)$$

where A_o is the signal amplitude and f_o the frequency of oscillation. In real oscillators, there are unwanted amplitude and frequency fluctuations present and the signal can be expressed as

$$V(t) = [A_o + \epsilon(t)] \, sin \, [2\pi f_o t + \Delta\phi(t)] \tag{5.27}$$

where $\epsilon(t)$ is the amplitude fluctuations and $\phi(t)$ is the phase fluctuations. The phase fluctuations are random in nature and are referred to as the phase noise. The phase noise is characterised by the ratio of the noise power in 1 Hz bandwidth at a frequency (offset) away from the carrier to the carrier signal power and it is expressed in decibels relative to the carrier per Hertz of bandwidth, dBc/Hz. It can be expressed as

$$\mathcal{L}(f) = \frac{P_{off/Hz}}{P_{carrier}} \tag{5.28}$$

where $\mathcal{L}(f)$ is the single sideband power referenced to the carrier, $P_{off/Hz}$ is the power in a 1 Hz bandwidth at a frequency away from the carrier and $P_{carrier}$, is the power of the carrier signal. Figure 5.13 shows the measured single side-band phase noise of both the single tunnel diode oscillator and the coupled oscillators, measured using the spectrum analyser from 100 kHz to 100 MHz offset frequency from the carrier.

The coupled synchronised oscillator was observed to have lower phase noise across the measured offset frequency range compared to the single device oscillator. The coupled oscillator design had a phase noise value of -124 dBc/Hz at 100 kHz offset from the carrier frequency and falling to -140 dBc/Hz at 10 MHz offset from the carrier. The phase noise of the single oscillator is -95 dBc/Hz at 100 kHz offset and -138 dBc/Hz at 10 MHz offset from the carrier.
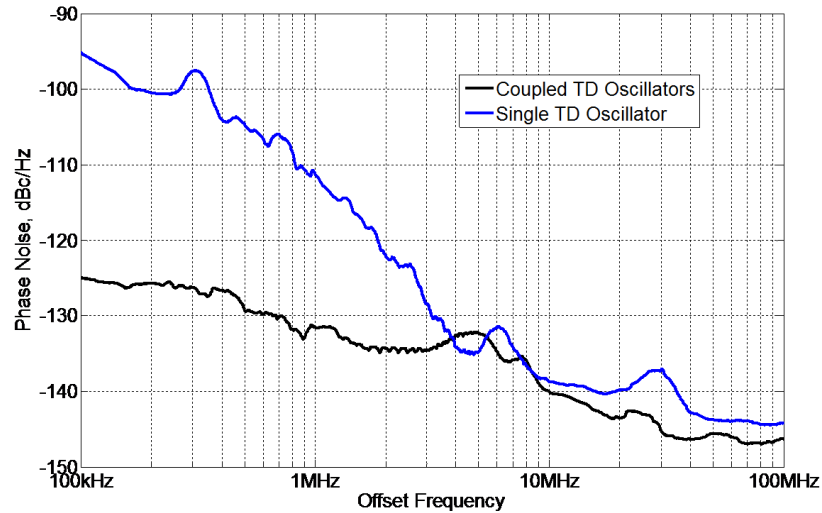
Figure 5.13: *Measured phase noise of single tunnel diode oscillator (blue line) and coupled tunnel diode oscillators (black line) at 100 kHz offset from carrier to 100 MHz offset from carrier.*

5.5   Summary

In this chapter, a novel self-synchronized NDR oscillator design using $1N3717$ tunnel diodes for improved power output was presented. The experimental results show that the output power for the synchronised oscillators was doubled compared to the single oscillator design topology. The results of single side-band phase noise for both oscillators were presented. The design can be scaled for higher frequencies by replacing the tunnel diodes in the designs with ultra-broadband resonant tunneling diodes, and realising the circuits in integrated circuit technology.

Chapter 6

A New Method for Antenna Radiation Pattern Characterisation in the Millimetre Wave and Terahertz Frequency Range

6.1   Introduction

To fully achieve the potential in the terahertz (THz) frequency range, suitable antennas are required to transmit and receive these signals. Due to the low power nature of solid-state integrated circuit THz sources, high gain and high directivity antennas are necessary for most applications. A highly directional antenna would allow most of the power from the source to be radiated in a specific or chosen direction, which could increase the range. Also for broadband THz sources such as resonant tunneling diode oscillators, antennas with broadband return loss are desirable because of the broad frequency range RTD-based oscillators can op-

erate. This makes RTDs coupled with broadband antennas a suitable choice for broadband wireless communication. To fully realise and implement a RTD coupled antenna design, the antenna radiation pattern has to be correctly characterised. Classic antenna radiation pattern characterisation set-up require an anechoic chamber, a receiving antenna (usually a horn antenna) and mechanical displacement of both the antenna under test and the receiving antenna [130]. This creates problems when working at frequencies where waveguide (rigid) connectors and probes rather than coaxial (flexible) connectors and probes are required to feed signal to the antenna.

This chapter discusses briefly antenna design theory and presents a very wideband planar quasi-Yagi antenna design for frequencies ranging from 140 GHz to 220 GHz. A proposed on-wafer two-dimensional radiation pattern characterisation method for air waveguide fed antenna is described and implemented.

6.2 Basic Antenna Theory

Antennas are structures associated with the region of transition between guided wave propagation and free space wave propagation or vice versa [131]. They essentially transform electromagnetic signals propagating in a wave-guide or transmission line into electro-magnetic (EM) waves propagating in free space and vice versa. To efficiently do this, the antenna dimensions have to be accurate for the frequency of operation. The optimal dimension for most antennas is half the wavelength, $\lambda/2$, of the operating frequency. Polarisation, which is the plane or orientation of the wave, is an important factor in choosing or designing antenna for specific applications. It is a property of the electric field vector that defines variations in direction and magnitude with time. It can be described as the locus

77

traced by the extremity of the time-varying electric field vector at a fixed observation point. Antennas are either linear, elliptical or circular polarised and the type of polarisation is determined by the orientation of the antenna elements.

The radiating field regions of an antenna can be classified into reactive near-field region, radiating near-field and the far-field region. The reactive near-field is the area in the immediate vicinity of the antenna where the reactive field is dominant and it is non-radiating. The boundary of the reactive near-field region is $\lambda/2\pi$ from the antenna aperture, where λ is the wavelength of the radiation [132]. The region next to this is the radiating near-field region also referred to as the $Fresnel$ zone. In this region radiating fields start to emerge and the reactive fields are not dominant. The boundary of this region is $2L^2/\lambda$, where L is the maximum dimension of the antenna. The far-field region often referred to as the $Fraunhofer$ region is furthest away from the antenna, and its boundary distance, $R > 2L^2/\lambda$, and the field distribution is completely independent of the distance from the radiating source. The far field region must also satisfy $R \gg L$ and $R \gg \lambda$. Figure 6.1 shows the example of a three dimensional field radiation pattern for a typical antenna.

The radiation pattern is a graphical representation of the antenna far-field properties. The principal two dimensional radiation pattern reference planes for linear polarised antennas are the electric field, E-plane, which contains the direction of maximum radiation in a plane parallel to the E vector and the magnetic field, H-plane which is orthogonal to the E-plane. The gain of an antenna G, is given by

$$G = \eta \times D \tag{6.1}$$

where D is directivity and η the radiation efficiency of the antenna. The antenna
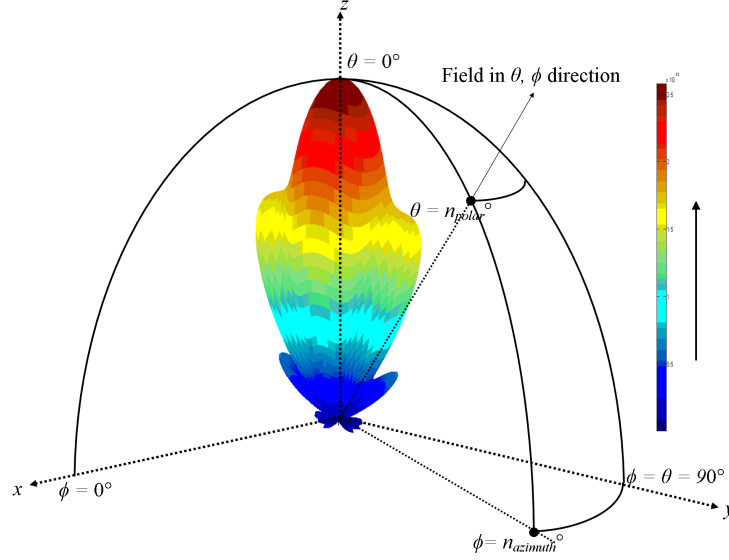
Figure 6.1: *Three dimensional far-field radiation pattern of a typical directive horn antenna showing maximum radiation in the z-direction at $\theta = 0$ and minor lobes. A point the radiation pattern is given by angles $\theta = n^\circ_{polar}$ and $\phi = n^\circ_{azimuth}$.*

radiation efficiency is the ratio of radiated power to the input power, i.e

$$\eta = \frac{P_{radiated}}{P_{input}} \tag{6.2}$$

Directivity of an antenna is the value of directive gain in the direction of maximum radiation (see Appendix A.2) [132]. The directive gain, D_g in any given direction is the ratio of the radiation intensity in that direction over the radiation intensity of an isotropic antenna (radiating evenly in all direction) and it can be expressed as

$$D_g = \frac{U}{U_{iso}} \tag{6.3}$$

where U is the radiation intensity given by the radiation density W_{rad} multiplied by the square of the distance r, $U = r^2 W_{rad}$ and U_{iso} the radiation intensity of an isotropic source. The directivity can then be expressed from Equation 6.3 as

$$D = \frac{U_{max}}{U_{iso}} \tag{6.4}$$

where U_{max} is the maximum radiation intensity. From Equation 6.4 it can be observed that the directivity of an isotropic antenna would be 1. The antenna directivity increases with reduced beam width area, Ω_A. The beam-width area is a solid angle through which all of the radiated power would go if the total field pattern, $F(\theta, \phi)$, is maximum over Ω_A and zero elsewhere. The radiated power can expressed in watts (W) as

$$P_{radiated} = F(\theta, \phi)\Omega_A \tag{6.5}$$

Figure 6.2 shows a typical radiation pattern showing half-power beam width. The beam-width area can be estimated by angles given at the half-power points of the main lobe in the two main planes, i.e.

$$\Omega_A \approx \theta_{halfpower}\phi_{halfpower} \tag{6.6}$$
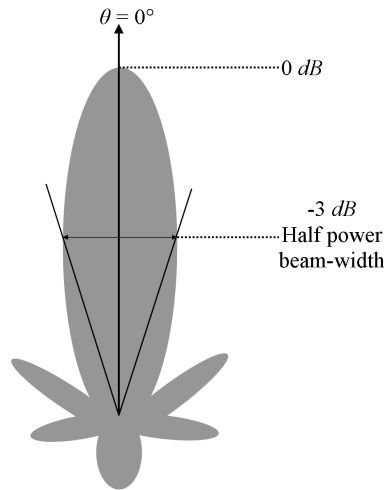
Figure 6.2: *Typical directive radiation pattern showing the half power beam width at the -3 dB beamwidth on the main lobe.*

6.3   Yagi Antenna

The Yagi-Uda antenna invented by Shintaro Uda and Hidetsugu Yagi in 1926 is a moderate gain linear polarised antenna most commonly used as terrestrial roof-top television antenna [133]. It is a highly directive antenna. The design of a Yagi antenna consists of a dipole as the driven element and parasitic elements which consists of the reflector and the director elements [134] [135]. The driven element is the only fed (power is applied) element and the dimension is usually in the order of half of the operating wavelength, $\lambda/2$. The Yagi antenna usually has just one reflector located behind the driven element and it is longer than half wavelength. The directors are located in front of the driven element in the direction of maximum sensitivity, and the dimension is usually shorter than $\lambda/2$, typically 0.45 λ. The number of directors can be increased to increase directivity and gain [132].

6.3.1   Planar Yagi Antenna

The Yagi antenna has been realised in planar form for the X-band frequency range, between 8 GHz to 12 GHz [136]-[138]. Figure 6.3 shows the design adopted in this thesis which is a coplanar waveguide (CPW) fed structure [136][139]. This was optimised for a design frequency of 200 GHz and it was realised on an indium phosphide (InP) substrate with a dielectric constant ε_r of 12.56. It consists of two director elements with lengths of 0.235 λ_{eff} and a driven element with length of 0.726 λ_{eff}. The reflector element is formed by the ground plane of the CPW feed line and the spacing between the directors and the driven element was chosen to be 0.06 λ_{eff} to reduce the total size [140]-[142]. Here, λ_{eff} is the effective wavelength given by

$$\lambda_{eff} = \frac{c}{f\sqrt{\varepsilon_{eff}}} \tag{6.7}$$

where c is the speed of light, f the design frequency and ε_{eff} is the effective dielectric constant given by [143]

$$\varepsilon_{eff} = \frac{\varepsilon_r + 1}{2} \tag{6.8}$$

ε_{eff} takes into account the waves travelling through air and also through the substrate. From equation 6.8, the InP dielectric constant ε_r of 12.56 results in an effective dielectric constant ε_{eff} of 6.78.
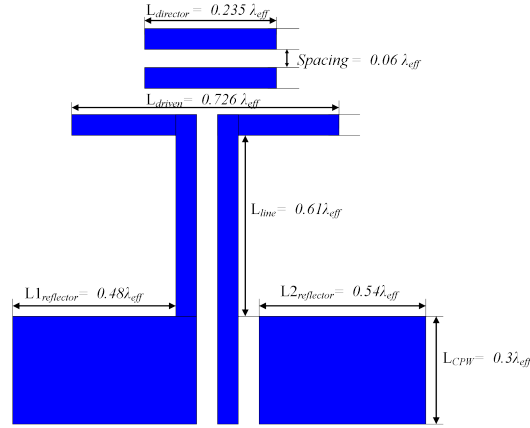
Figure 6.3: *Planar Yagi antenna geometry showing dimensions of elements.*

6.4   Experimental results

The dimensions for a planar Yagi antenna designed for the frequency of 200 GHz on InP substrate are shown in Figure 6.3. The calculated antenna dimensions are shown in Table 6.1. The 50Ω coplanar waveguide (CPW) feed-line has a length

of 558 μm. The signal line width is 20 μm with separation on either side of 13.8 μm from the ground planes.

Frequency (GHz)	Driven element $L_{driven}(\mu m)$	Director $L_{director}(\mu m)$	Reflector$_1$ $L_{1(reflector)}(\mu m)$	Reflector$_2$ $L_{2(reflector)}(\mu m)$
200	418	135	295	311

Table 6.1: Planar Yagi antenna dimensions for 200 GHz

As part of the project, the antenna was fabricated by Khalid Alharbi using electron beam lithography process implemented on 600 μm thick indium phosphide (InP) substrate with electrical resistivity of 8.6×10^7 Ωcm. Electron beam resist polymethyl methacrylate (PMMA) was used, which was spun in two layers on the InP sample and baked for 2 minutes at $143°C$ for each layer. Titanuim/Gold (Ti/Au), 20 nm/400 nm thick metal scheme was deposited using electron beam evaporator to pattern the antenna elements [141].

Figure 6.4 shows an optical micrograph of the fabricated Yagi antenna [144].
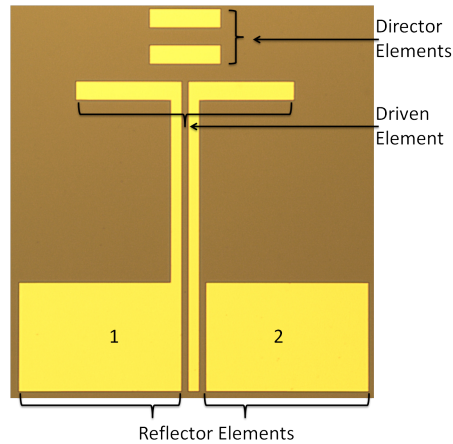
Figure 6.4: *Fabricated planar Yagi antenna showing the director elements, the driven elements and the reflector elements which is formed by the co-planar waveguide (CPW) transmission feed line ground planes [144].*

6.4.1 Antenna Return Loss

The return loss of an antenna, measured from one port scattering parameter (S_{11}) characterisation, is a measurement of how much power is reflected back (due to impedance mismatch) at the antenna port compared to the input power. It can be expressed simply as

$$Return\ Loss = -20Log_{10} \mid S_{11} \mid dB \qquad (6.9)$$

It gives an indication of the operating bandwidth. An input port reflection coefficient, S_{11} value under -10 dB is an accepted value for an antenna's return loss as this means less than 10 % of the input power to the antenna is reflected back and 90 % of the available power is transmitted. Figure 6.5a shows a block diagram of the measurement set-up used for the Yagi antenna S-parameter measurements.

The measurement was carried out using a Keysight E8364B network analyser with upper frequency limit of 50 GHz. This is connected to the OML Inc V05VNA2-T/R-A frequency extenders for 140-220 GHz frequency band through the Keysight N5260A millimetre head controller. The RF and local osillator (LO) frequencies needed to cover the band are provided by two E8257D analog signal generators from Keysight (each with frequency range of 250 kHz to 20 GHz). Two waveguide based coplanar probes are connected to the ports on the frequency extenders for measurements. Figure 6.5b shows a picture of the measurement set-up. The CPW feed line allows for radio frequency (RF) on wafer probing using narrow (50 μm) pitch ground-signal-ground (GSG) coplanar probes. Short-open-load-thru (SOLT) calibration to correct for errors and move the measurement reference plane to the tips of the probe was carried out before measurements using the GGB Industries Inc $CS-15$ impedance standard substrate, with -10 dBm power applied to the port.
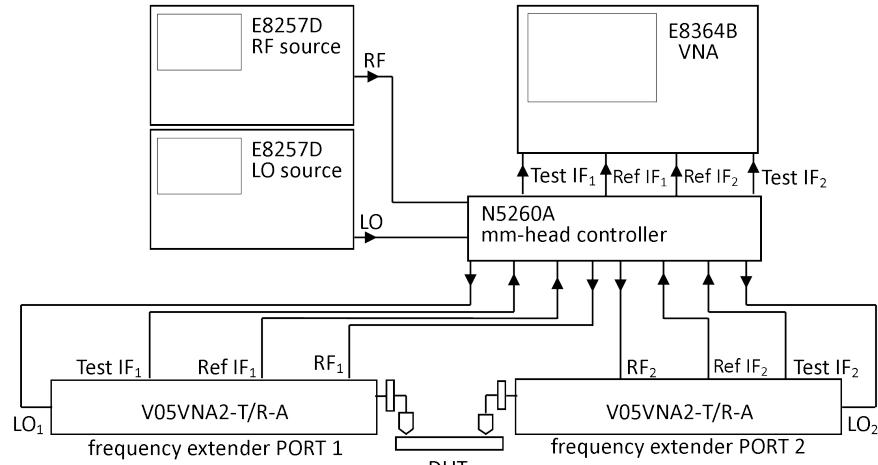
(a)
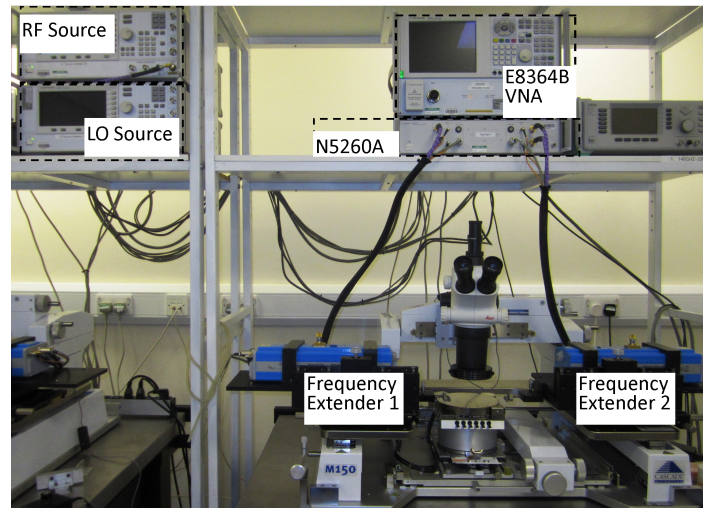
(b)

Figure 6.5: *S-parameter measurement system for 140 - 220 GHz. (a) Measurement block diagram. Mixers in the frequency extenders are utilized to cover the frequency range, with the LO and RF frequencies provided by the signal generators(adapted from [145]). (b) Picture of the measurement set-up.*

The measured S_{11} is presented in Figure 6.6 for the 140-220 GHz frequency band antenna along with the simulated results from the ANSYS HFSS. The HFSS simulator employs the finite element method based electromagnetic solver. A 3D geometry of the antenna dimensions including the InP substrate is created and the

parameters defined. A wave-port is used to excite the mode of the feed line at its input which excites the whole structure. An air box which extends to the far-field region is defined to model open space. This absorbs the incident radiation from the structure and thus, eliminate any reflections. The frequency analysis/sweep setup is defined for 140-220 GHz. The finite element method uses mathematical techniques to solve Maxwell's electromagnetic equations (see Appendix A.3) in the entire model by creating a volume based mesh and producing field solutions for the entire volume including the surrounding environment [146][147].

In Figure 6.6, the measured and simulated -10 dB bandwidth of the antenna designed at 200 GHz shows a 40 % operating bandwidth [144].
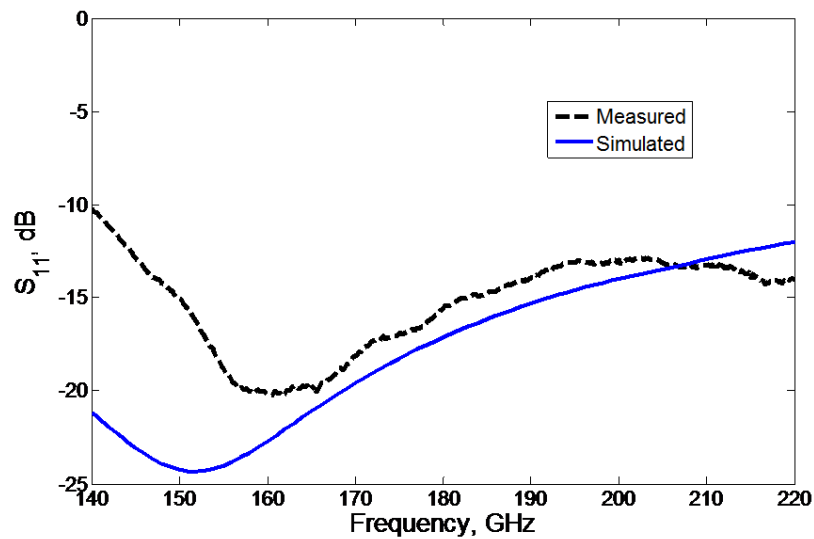
Figure 6.6: *Measured and simulated return loss of Yagi antenna at 140 GHz to 220 GHz frequency range [144].*

6.5   Antenna Radiation Pattern

Typically, radiation pattern measurements of antennas are carried out in a reflection free environment, usually an anechoic chamber. The anechoic chamber is usually filled with pyramid absorbers made from foam and coated with carbon. To be effective, the size of the pyramid must be at least one half wavelength long at the lowest frequency of interest [148]. The absorbing quality of the anechoic chamber is usually limited by the chamber's frequency range. Another restricting factor is the feed line type in the anechoic chamber which is usually co-axial. Also, antenna radiation pattern characterisation do employ a reference antenna and mechanical displacement of either or both of the reference antenna and the antenna under test [149]. Figure 6.7 shows an anechoic chamber for characterising antennas designed at frequencies from up to 18 GHz.

In Figure 6.7, the reference antenna is a dual-polarised log-periodic antenna that can operate between 500 MHz to 18 GHz mounted on a mechanical arm and it is connected to a VNA through a coaxial cable. The antenna under test (AUT) is a bow-tie antenna mounted on a rotating stage. The AUT is also connected using a coaxial cable to the VNA. The mechanical arm and rotating stage allows for the characterisation of the three dimensional radiation pattern of the AUT. The pyramid absorber is fabricated from urethane foam impregnated with conductive carbon and it has an absorbing frequency range from 500 MHz to 40 GHz [150]. However, above 110 GHz, coaxial connectors are no longer available and rigid air waveguide connectors are required. These factors make it difficult to characterise waveguide probe fed antennas at high frequencies.
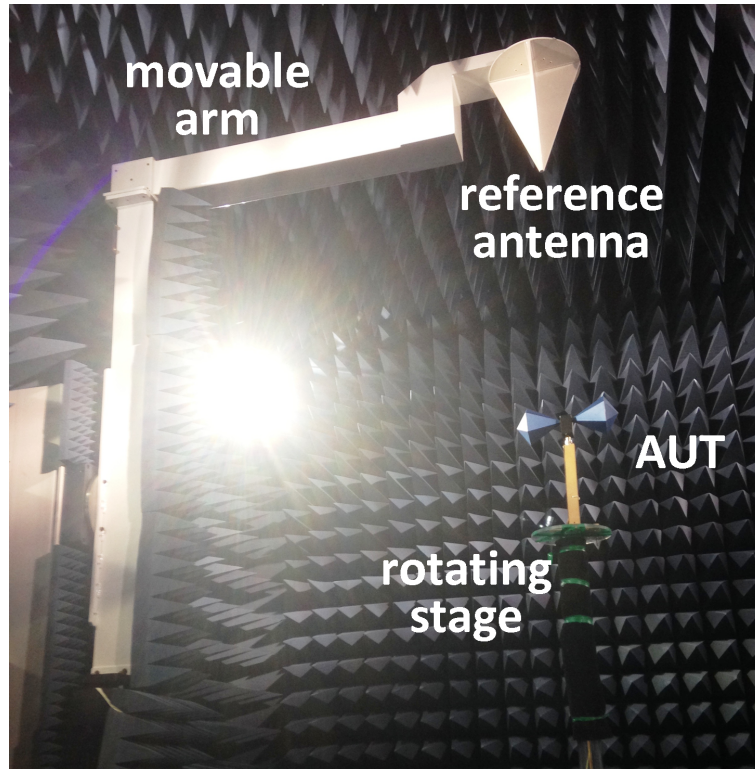
Figure 6.7: *Anechoic chamber designed for frequencies up to 18 GHz showing a reference antenna on a movable arm and the antenna under test (AUT) on a rotating stage.*

6.5.1 Two Dimensional Antenna Radiation Pattern Characterisation

Various set-ups have been used in several works to characterise the radiating fields of probe-fed antennas. In those set-ups, the antenna under test (AUT) is connected to a signal source and it is fixed while the receiving reference horn antenna is placed on a rotary arm which measures the radiation from the AUT at various angles. The reference antenna is connected to a spectrum analyser to measure the received power [151]-[154]. These set-ups, however, have only been used to characterise antennas under 110 GHz with available coaxial connectors which allows mechanical movement of the reference antenna. Above 110 GHz,

rigid waveguides which would allow connection to the reference antenna do not allow for such movement [155].

To avoid the need for mechanical displacement when using a waveguide feed-line, a compact $E-$plane on-wafer radiation pattern technique for on-wafer antennas at high frequency shown in Figure 6.8 was proposed and implemented [141] with a radiating/transmitting antenna and a number of receiving (Rx) antennas distributed around the radiating antenna covering angles from $-90°$ to $90°$ in $15°$ steps. At each angle and frequency, the magnitude of the S_{21} data is recorded to plot the radiation pattern. The S_{21} is the forward transmission gain. It is the ratio of received signal to the transmitted signal, and it gives a measure of the radiation intensity. Plotting the S_{21} with angular positions provides the radiation pattern of the antenna. The antennas are identical to the planar Yagi antenna designed at 200 GHz discussed above and are distributed angularly around a single identical antenna which is the antenna under test (AUT).
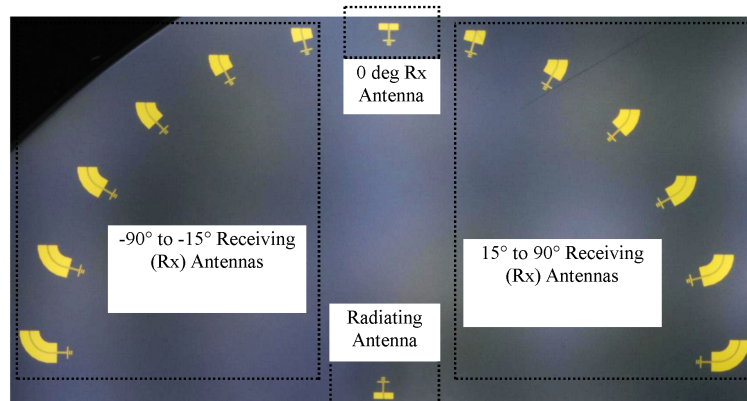
Figure 6.8: *Fabricated planar Yagi antennas for on wafer radiation pattern characterisation.*

The number and positions of the distributed antennas are chosen according to the angles at which the radiation pattern will be measured. The distance between the receiving antennas and the radiating antenna is kept at 11.4 *mm*. Also,

the distributed receiving antennas are positioned outside the radiating near field boundary of 1.9 mm to each other to minimise coupling between them. However, doing this reduces the number of angles at which the radiation pattern could be measured.

Since the waveguide probes on the measurement station used is fixed, the angular range of the distributed antennas from $-90°$ to $90°$ are achieved by extending the CPW-feed lines to the antennas with curves at $15°$ each. Figure 6.9 shows the de-embedding structures consisting of a straight CPW transmission line and a curved CPW line with two $15°$ curves fabricated on the same substrate. The S_{21} parameters of these curved lines are measured and used to account for the losses introduced by the extended lines.

(a)   (b)
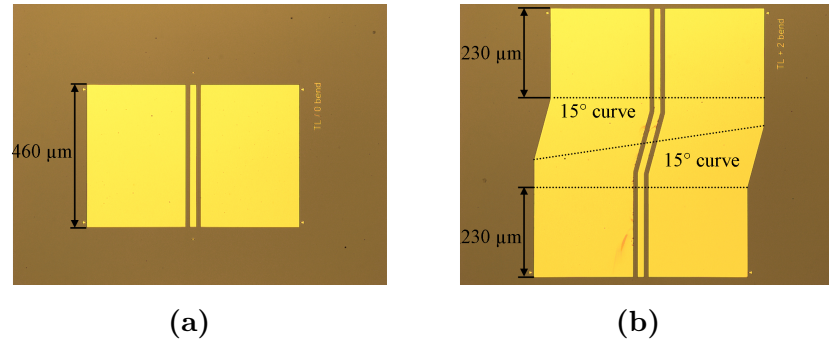
Figure 6.9: *De-embedding structures for extended CPW feed line loss correction, to achieve S_{21} parameters at desired angles. (a)Straight transmission line,(b) Transmission line with two $15°$ curves.*

The S_{21} parameters were measured using the same set-up for the return-loss measurements. The actual S_{21} parameters of the antenna under test at each angle is then determined by adding the losses introduced by the extended lines to the measured data. The corrected S_{21} parameter for each angle is determined by first getting the S_{21} parameter for a $15°$ curve. This is achieved from measuring a transmission line with no curve $S_{21(Tline)}$ in Figure 6.9a, along with that of

a transmission line with two 15° curves, $S_{21(Tline + 2\,curved\,sections)}$ in Figure 6.9b. The relationship for the S_{21} parameter of the transmission line with two curved sections is

$$S_{21(Tline + 2\,curved\,sections)} = S_{21(Tline)} \times S_{21(1\,curved\,section)} \times S_{21(1\,curved\,section)} \quad (6.10)$$

for a 15° curved section, $S_{21(1\,curved\,section)}$ this becomes

$$S_{21(1\,curved\,section)} = \sqrt{\frac{S_{21(Tline + 2\,curved\,sections)}}{S_{21(Tline)}}} \quad (6.11)$$

the actual S_{21} parameter for each pair of radiating/receiving antenna, $S_{21(actual\,\theta)}$ is then determined by

$$S_{21(actual\,\theta)} = \frac{S_{21(measured\,\theta)}}{\left[S_{21(1\,curved\,section)}\right]^{n}} \quad (6.12)$$

where n is the number of 15° angles that make up the curve. The average loss caused by the 202 μm long 15° curved transmission line section is $\sim 13\ dB$. The radiation pattern of the antenna at a given frequency is obtained by

$$20\ log_{10}\ (S_{21(actual\,\theta)}),\ dB \quad (6.13)$$

this is normalised at each angle with the maximum S_{21} at 0° for the frequency of interest to plot the normalised radiation pattern. Figures 6.10a and 6.10b shows the normalised measured and simulated radiation patterns plotted from the HFSS analysis at 199 GHz and 209.8 GHz respectively.

It can be seen that the patterns show similar directivity and field pattern in the measured and simulated radiation patterns. However, there are discrepancies
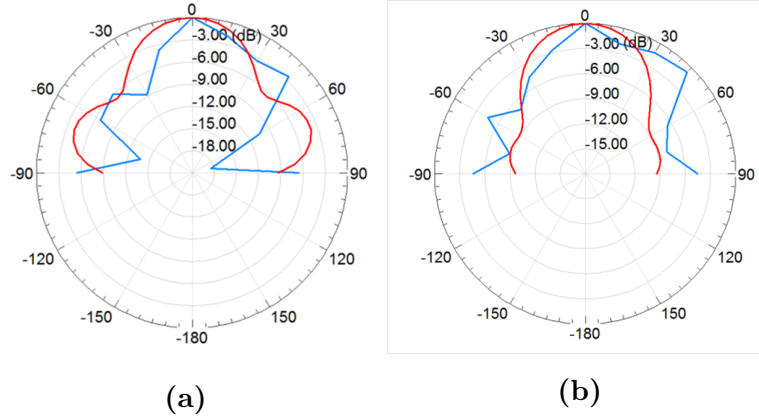
Figure 6.10: *(a) Measured (Blue) and simulated (Red) radiation pattern of fabricated Yagi antenna at 199 GHz, (b) At 209.8 GHz.*

at some angles. This may be caused by unwanted reflected signals from metal surrounding the probe station reaching the antennas which add constructively or destructively to the desired received signal.

6.5.2 Antenna Gain

The maximum gain of the antenna can be determined from the Friis transmission equation [132], Equation 6.14, by measuring the two antennas facing each other at 0°:

$$G_r G_t = G^2 = \left(\frac{P_r}{P_t} \right) \left(\frac{4\pi R}{\lambda_o} \right)^2 \tag{6.14}$$

where G_r and G_t are the power gain of the receiving and transmitting antenna respectively, P_r and P_t are the received and transmitted power respectively and λ_o is the free space wavelength. R is the distance between the transmitting and receiving antenna. For two identical antennas facing each other on the same

substrate, $G_r = G_t = G$ because the transmitting and receiving antenna are identical. Equation 6.15 can be re-written for this case as

$$G^2 = |S_{21}|^2 \left(\frac{4\pi R}{\lambda_o} \right)^2 \tag{6.15}$$

where S_{21} is the ratio of received power to the transmitted power for identical antennas. λ_{eff} is the effective wavelength for the antennas transmitting and receiving on the substrate. The antenna gain, G_{dB}, in decibels would be given by

$$G_{dB} = 10 Log_{10} G \tag{6.16}$$

The distance between the antennas, R is kept at 11.4 mm on the InP substrate. This keeps the transmitting and receiving antennas out of their far-field boundaries. The gain from the measured S_{21} parameter in the E-plane of the 140-220 GHz band antenna is 6.3 dB at 199 GHz and 6.7 dB at 209.8, when S_{21} is 0.043 and 0.047, respectively. The simulated gain for the antenna is 4.2 dB at 199 GHz and 5.3 dB at 209.8 GHz.

6.6   Summary

In this chapter, ultra-broadband planar antennas with moderate gain which can be implemented in the terahertz range for integrated circuits has been presented. Also, two dimensional radiation pattern characterisation method of probe fed antennas has been presented and the results show good agreement with simulated results. Also, a method that could be used to characterise the E-plane for any directive planar antenna has been described.

Chapter 7

Conclusions and Future Work

7.1   Conclusions

Devices with negative differential resistance such as Gunn diodes, tunnel diodes, impact ionisation avalanche transit-time (IMPATT) diodes and resonant tunneling diodes (RTDs) can be used in electronic oscillators to generate high frequency signals. Of these devices, resonant tunneling diodes (RTDs) are one of the most promising solid-state devices for terahertz generation at room temperature. RTDs are the fastest operating solid-state electronic devices, and the highest reported frequency of oscillation of RTD-based oscillator up till now is 1.55 THz with 0.4 μW of output power [46], and with a theoretical bandwidth of up to 2.5 THz [156]. Despite the achievable high frequencies, RTD oscillators are still limited by their low output power. Some of the other limitations of the resonant tunneling diodes are the bias oscillations associated with devices which makes it difficult to accurately determine the DC characteristics of the device in the negative differential resistance (NDR) region and therefore, a lack of accurate models which could help to optimize the RTD device for various applications.

The purpose of this PhD project was to address some of these limitations and the main results achieved are:

- Accurate and direct oscillation-free characterisation of a 1N3712 tunnel diode (TD) and a 0.75×0.75 μm^2 resonant tunneling diode (RTD) in the NDR region of the current-voltage (I-V) curve. This was done using pulsed DC measurements instead of a static DC bias. The dynamic nature of the pulsed DC method enables the defining of the pulse widths and rise times to compensate for different device peak currents and most importantly allows for the monitoring of the onset of bias oscillations and so taking the measurements in a stable region before the oscillations begin to occur. A physics-based analytical model of the RTD was extracted and accurately models the current density-voltage (J-V) characteristics of the device. The model can be used in circuit simulation using computer aided design (CAD) software.

- Radio frequency (RF) characterisation of a RTD was carried out from 10 MHz to 67 GHz at a bias point in the positive differential resistance (PDR) region and at some points in the NDR region. The S-parameter results were used to determine an accurate small-signal model of the device for the PDR region, but this was not possible in the NDR region due to the effects of the parasitic bias oscillations in the S-parameter measurement carried out in this region.

- A hybrid oscillator using commercially available 1N3717 tunnel diodes realised in micro-strip technology, employing a novel power combining method of two similar oscillators to improve the power output, was demonstrated. The design employed two oscillators decoupled and biased independently with the output powers from both taken at a single end. The oscillator had

a maximum measured output power of -6.72 dBm (0.21 mW) at 716.2 MHz compared to a single device oscillator of similar size which provided -9.09 dBm (0.12 mW) at 575.7 MHz, a more than 2 dB improvement.

- A planar Yagi antenna suitable for terahertz applications with ultra-broadband response for 140 - 220 GHz frequency range (-10 dB return-loss) was fabricated and characterised. A new method for two dimensional characterisation of the radiation patterns of on-wafer planar antennas was also presented. This characterisation method allows for on wafer radiation pattern characterisation without the need for mechanical displacement of the antenna and can be performed despite the unavailability of a suitably rated anechoic chamber. However, the limitations of this method are the number of angles at which measurements could be taken for a smoother radiation field plot. Also, the measurements can be carried out in only the $E-$field plane.

7.2 Future Work

7.2.1 Improved Oscillator Design

An accurate large signal model for an RTD can be developed with accurate DC characteristics and a reliable small-signal model which can be incorporated. This would help improved designs of RTD-based oscillators where the performance can accurately simulated before fabrication.

7.2.2   Higher Frequency Coupled RTD Oscillator

Higher power coupled oscillators using RTDs instead of tunnel diodes could be realised for oscillation at higher frequencies. This could be implemented as an integrated circuit for applications in the terahertz range.

7.2.3   Integrated Antenna Design

At terahertz frequencies, a way to extract the output power from the oscillator would require integrated antennas. Therefore, RTD oscillator designs with integrated antennas need to be developed in the future. This would require an antenna with high directivity due to the low oscillator output power in the THz range. One of the immediate applications for such design is high data-rate short range wireless communications.

Appendix A

Equations

A.1 Non-linear Least Squares Fitting

This is a mathematical procedure for finding the best fitting curve to a given set of points $(x_1, y_1 ... x_m, y_m)$ by minimizing the sum of the squares of the offsets of the points from the curve. Given a non-linear function $f(x)$, with n number of unknown parameters $(\beta_1 ... \beta_n)$ the curve fitting problem is expressed in the form [157] [158]

$$\min_x ||f(x)||_2^2 = \min_x \left(f(x_1)^2 + f(x_2)^2 .... f(x_m)^2 \right) \tag{A.1}$$

with optional boundaries on the component x. The minimiser is found by

$$F(x) = \min_x \frac{1}{2} ||f(x)||_2^2 = \min_x \frac{1}{2} \sum_{i=1}^{m} r_i(x)^2 \tag{A.2}$$

where r_i is the residual errors. The minimum value of $F(x)$ occurs when the gradient is zero, if gradient optimisation is used.

$$\frac{\partial F(x)}{\partial \beta_j} = \sum_{i=1}^{m} r_i(x) \frac{\partial r_i}{\partial \beta_j} \tag{A.3}$$

A.2   Antenna Directivity

To define an expression for directivity, first a definition for directive gain in a given direction which is the ratio of the radiation intensity in that direction to the radiation intensity of a reference antenna which is an isotropic source is needed, and it can be written as [132]

$$D_g = \frac{U}{U_{iso}} = \frac{4\pi U}{P_{rad}} \tag{A.4}$$

where D_g is the directive gain and it is dimensionless, U is the radiation intensity and U_{iso} the radiation intensity of an isotropic source both in W/unit solid angle. P_{rad} is the total radiated power obtained by integrating the radiation intensity over a solid angle of 4π, and can be expressed as

$$P_{rad} = \int_0^{2\pi} \int_0^{\pi} U_{iso} sin\theta d\theta d\phi \tag{A.5}$$

where for a solid angle $sin\theta d\theta d\phi = d\Omega$, Equation A.5 can be re-written as

$$P_{rad} = \int_0^{2\pi} \int_0^{\pi} U_{iso} d\Omega = 4\pi U_{iso} \tag{A.6}$$

The directivity of a non-isotropic source is equal to the ratio of the maximum radiation intensity to the radiation intensity of an isotropic source and can be written as

$$D_g = \frac{U_{max}}{U_{iso}} = \frac{4\pi U_{max}}{P_{rad}} \tag{A.7}$$

For a more general directivity expression, let the radiation intensity of an antenna be in the form of

$$U = B_0 F(\theta, \phi) \tag{A.8}$$

where $F(\theta, \phi)$ is the total field pattern and B_0 is a constant. the maximum value of Equation A.8 is given by

$$U_{max} = B_0 F_{max}(\theta, \phi) \tag{A.9}$$

and the total radiated power is given by

$$P_{rad} = B_0 \int_0^{2\pi} \int_0^{\pi} F(\theta, \phi) sin\theta d\theta d\phi \tag{A.10}$$

The general equation for directive gain and directivity can then be written from Equations A.4 and A.7 as

$$D_g(\theta, \phi) = 4\pi \frac{F(\theta, \phi)}{\int_0^{2\pi} \int_0^{\pi} F(\theta, \phi) sin\theta d\theta d\phi} \tag{A.11}$$

$$D = 4\pi \frac{F(\theta, \phi)|_{max}}{\int_0^{2\pi} \int_0^{\pi} F(\theta, \phi) sin\theta d\theta d\phi} \tag{A.12}$$

$$D = \frac{4\pi}{\left[\int_0^{2\pi} \int_0^{\pi} F(\theta, \phi) sin\theta d\theta d\phi \right] / F(\theta, \phi)|_{max}} \tag{A.13}$$

A.3 Maxwell's Equations

Maxwell's equations are a set of laws which describe how electric fields and magnetic fields propagate, interact and how they are influenced. They consist of Gauss's law for electricity, Gauss's law for magnetic field, Faraday's law and Ampere's law [159]-[161].

- Gauss's law states that the total electric field leaving a volume is equal to the total charge within the volume. It is expressed in differential form as

$$\nabla \cdot \mathbf{D} = \rho_v \tag{A.14}$$

  where ∇ is the divergence operator which is the measure of the vector out of a surface at a given point, $\mathbf{D}$ is the electric displacement field and it is related to the electric field by $\mathbf{D} = \varepsilon \mathbf{E}$. Here, ε is the permittivity of the material where the field is being measured and $\mathbf{E}$, is the electric field. ρ_v is the electric volume charge density in C/m^3. It is the ratio of the total electric charge, ρ to the total volume.

- Gauss's law for magnetic fields states that the net magnetic flux around any surface is zero. It is expressed as

$$\nabla \cdot \mathbf{B} = 0 \tag{A.15}$$

  where $\mathbf{B}$ is the magnetic flux density in Wb/m^2.

- Faraday's law of induction states that the induced electromotive force in any closed circuit is equal to the negative of the rate of change in time of the

magnetic flux enclosing the circuit. This means a time changing magnetic field results in a circulating electric field. It is expressed as

$$\nabla \times \mathbf{E} = -\frac{\partial \mathbf{B}}{\partial t} \tag{A.16}$$

- Ampere-Maxwell's law states that a flowing electric current through a wire gives rise to a magnetic field that circles the wire. Also, a time changing electric flux density gives rise to a magnetic field that circles it. It is expressed as

$$\nabla \times \mathbf{H} = \mathbf{J} + \frac{\partial \mathbf{D}}{\partial t} \tag{A.17}$$

where $\mathbf{H}$ is the magnetic field in A/m and $\mathbf{J}$, is the electric current density in A/m^2

Bibliography

[1] P. Siegel, "Terahertz technology," *IEEE Transactions on Microwave Theory and Techniques*, vol. 50, no. 3, pp. 910–928, 2002.

[2] Y.-S. Lee, "Principles of terahertz science and technology," *Springer, US. 1st Edition*, 2009.

[3] C. Armstrong, "The truth about terahertz," *Spectrum, IEEE*, vol. 49, pp. 36–41, September 2012.

[4] "IEEE Standards for safety levels with respect to human exposure to radio frequency electromagnetic fields, 3 kHz to 300 GHz," 2006.

[5] M. Shur, "Terahertz technology: devices and applications," *31st European Solid-State Circuits Conference (ESSCIRC)*, pp. 13–21, Sept 2005.

[6] M. Tonouchi, "Prospect of terahertz technology," *19th International Conference on Applied Electromagnetics and Communications (ICECom)*, pp. 1–4, Sept 2007.

[7] C. Sirtori, "Bridge for the thz gap," *Nature*, vol. 417, pp. 132–133, 9 May 2002.

[8] M. Cooke, "Filling the THz gap with new applications," *Semiconductor Today*, vol. 2, no. 1, pp. 39–43, February 2007.

[9] M. Tonouchi, "Cutting edge terahertz technology," *Nature Photonics*, vol. 1, pp. 97–106, 2007.

[10] A. Leuther, S. Koch, A. Tessmann, I. Kallfass, T. Merkle, H. Massler, R. Loesch, M. Schlechtweg, S. Saito, and O. Ambacher, "20 nm Metamorphic HEMT with 660 GHz f_T," *23rd International Conference on Indium Phosphide and Related Materials*, pp. 1–4, May 2011.

[11] D.-H. Kim and J. del Alamo, "30-nm InAs pHEMTs with $f_T = 644$ GHz and $f_{max} = 681$ GHz," *IEEE Electron Device Letters*, vol. 31, pp. 806–808, Aug 2010.

[12] M. Urteaga, R. Pierson, P. Rowell, V. Jain, E. Lobisser, and M. Rodwell, "130nm InP DHBTs with $f_T > 0.52$ THz and $f_{max} > 1.1$ THz," *69th Annual Device Research Conference (DRC)*, pp. 281–282, June 2011.

[13] M. Seo, M. Urteaga, J. Hacker, A. Young, Z. Griffith, V. Jain, R. Pierson, P. Rowell, A. Skalare, A. Peralta, R. Lin, D. Pukala, and M. Rodwell, "InP HBT IC technology for terahertz frequencies: Fundamental oscillators up to 0.57 THz," *IEEE Journal of Solid-State Circuits*, vol. 46, pp. 2203–2214, Oct 2011.

[14] S.-J. Yeon, M. Park, J. Choi, and K. Seo, "610 GHz InAlAs/In0.75GaAs metamorphic HEMTs with an ultra-short 15-nm-gate," *IEEE International Electron Devices Meeting*, pp. 613–616, Dec 2007.

[15] G. P. Gallerano and S. Biedron, "Overview of terahertz radiation sources," *26th International Free-Electron Laser Conference*, pp. 216–221, 2004.

[16] Y. Zhang, R. Han, Y. Kim, D. Y. Kim, H. Shichijo, S. Sankaran, C. Mao, E. Seok, D. Shim, and K. Kenneth, "Schottky diodes in CMOS for terahertz

circuits and systems," *13th Topical Meeting on Silicon Monolithic Integrated Circuits in RF Systems (SiRF)*, pp. 24–26, Jan 2013.

[17] J. Ward, E. Schlecht, G. Chattopadhyay, A. Maestrini, J. Gill, F. Maiwald, H. Javadi, and I. Mehdi, "Capability of THz sources based on Schottky diode frequency multiplier chains," *IEEE MTT-S International Microwave Symposium Digest*, vol. 3, pp. 1587–1590, June 2004.

[18] R. K. Gupta and C. G. Englefield, "Up-conversion in IMPATT amplifiers," *IEEE Transactions on Microwave theory and Techniques*, vol. 26, pp. 28–30, January 1978.

[19] J. Schaar, K. Vodopyanov, P. Kuo, M. Fejer, X. Yu, A. Lin, J. S. Harris, D. Bliss, C. Lynch, V. Kozlov, and W. Hurlbut, "Terahertz sources based on intracavity parametric down-conversion in quasi-phase-matched gallium arsenide," *IEEE Journal of Selected Topics in Quantum Electronics*, vol. 14, pp. 354–362, March 2008.

[20] B. Williams, S. Kumar, Q. Hu, and J. Reno, "Resonant-phonon terahertz quantum-cascade laser operating at 2.1THz ($\lambda \simeq 141\mu m$)," *IEEE Electronics Letters*, vol. 40, pp. 431–433, April 2004.

[21] V. Flyagin, A. Gaponov, M. Petelin, and V. Yulpatov, "The gyrotron," *IEEE Transactions on Microwave Theory and Techniques*, vol. 25, pp. 514–521, Jun 1977.

[22] M. Dunning, C. Hast, E. Hemsing, K. Jobe, D. McCormick, J. Nelson, T. O. Raubenheimer, K. Soong, Z. Szalata, D. Walz, S. Weathersby, and D. Xiang, "Generating periodic terahertz structures in a relativistic electron beam through frequency down-conversion of optical lasers," *Physical Review Letters*, vol. 109, pp. 074801–5, Aug 2012.

[23] D. Stanze, A. Deninger, A. Roggenbuck, S. Schindler, M. Schlak, and B. Sartorius, "Compact CW Terahertz Spectrometer Pumped at 1.5 μm Wavelength," *Journal of Infrared, Millimeter, and Terahertz Waves*, vol. 32, no. 2, pp. 225–232, 2011.

[24] Y. C. Shen, P. C. Upadhya, H. E. Beere, E. H. Linfield, A. G. Davies, I. S. Gregory, C. Baker, W. R. Tribe, and M. J. Evans, "Generation and detection of ultrabroadband terahertz radiation using photoconductive emitters and receivers," *Applied Physics Letters*, vol. 85, no. 2, pp. 164–166, 2004.

[25] A. Reklaitis, "Comparison of efficiencies of GaAs-based pulsed terahertz emitters," *Journal of Applied Physics*, vol. 101, no. 11, 2007.

[26] E. R. Brown, K. A. McIntosh, K. B. Nichols, and C. L. Dennis, "Photomixing up to 3.8 thz in low temperature grown GaAs," *Applied Physics Letters*, vol. 66, no. 3, pp. 285–287, 1995.

[27] N. Pala and A. N. Abbas, "Terahertz technology for nano applications, springer netherlands," *Encyclopedia of Nanotechnology*, pp. 2653–2667, 2012.

[28] F. Amir, C. Mitchell, and M. Missous, "Development of advanced gunn diodes and schottky multipliers for high power THz sources," *8th International Conference on Advanced Semiconductor Devices Microsystems (AS-DAM)*, pp. 29–32, Oct 2010.

[29] H. Wang, Z. Liang, and Z. Yang, "Interactions of electron beams with electromagnetic waves in cherenkov devices," *Nuclear Instruments and Methods in Physics Research Section A: Accelerators, Spectrometers, Detectors and Associated Equipment*, vol. 539, no. 12, pp. 37 – 43, 2005.

[30] http://www.bridge12.com/learn/gyrotron, "Bulletin:What is a Gyrotron? [February, 2015],"

[31] G. Gonzalez, "Microwave transistor amplifiers: Analysis and design," *Prentice Hall, Inc. 2nd Edition*, 1984.

[32] B. Bosch and R. W. H. Englemann, "Gunn-effect electronics," *Wiley*, 1975.

[33] Z. Gribnikov, R. Bashirov, and V. Mitin, "Negative effective mass mechanism of negative differential drift velocity and terahertz generation," *IEEE Journal of Selected Topics in Quantum Electronics*, vol. 7, no. 4, pp. 630–640, 2001.

[34] H. Eisele, A. Rydberg, and G. Haddad, "Recent advances in the performance of InP Gunn devices and GaAs TUNNETT diodes for the 100-300 GHz frequency range and above," *IEEE Transactions on Microwave Theory and Techniques*, vol. 48, pp. 626–631, Apr 2000.

[35] A. Khalid, C. Li, V. Papageogiou, G. Dunn, M. Steer, I. Thayne, M. Kuball, C. Oxley, M. Montes Bajo, A. Stephen, J. Glover, and D. Cumming, "$In_{0.53}Ga_{0.47}$As planar Gunn diodes operating at a fundamental frequency of 164 GHz," *IEEE Electron Device Letters*, vol. 34, pp. 39–41, Jan 2013.

[36] K. Chang, W. Thrower, and G. Hayashibara, "Millimeter-wave silicon IMPATT sources and combiners for the 110-260 GHz range," *IEEE Transactions on Microwave Theory and Techniques*, vol. 29, pp. 1278–1284, Dec 1981.

[37] M. Mukherjee and N. Mazumder, "Modeling of high power 0.3 THz IMPATT oscillator based on 3C-SiC and growth of 3C-SiC on Si (100) substrate for possible IMPATT fabrication," *International Conference on Mi-*

crowave and Millimeter Wave Technology (ICMMT), vol. 2, pp. 897–900, April 2008.

[38] R. Khazaka, E. Bahette, M. Portail, D. Alquier, and J.-F. Michaud, "Toward high-quality 3CSiC membrane on a 3CSiC pseudo-substrate," *Materials Letters*, vol. 160, pp. 28 – 30, 2015.

[39] C. O'Sullivan and J. Murphy, "Field guide to terahertz sources: Detectors,and optics," *SPIE Press*, 2012.

[40] J. Nishizawa, K. Motoya, and Y. Okuno, "GaAs TUNNETT Diodes," *IEEE Transactions on Microwave Theory and Techniques*, vol. 26, pp. 1029–1035, Dec 1978.

[41] J. Nishizawa, P. Plotka, H. Makabe, and T. Kurabayashi, "GaAs TUNNETT diodes oscillating at 430-655 GHz in CW fundamental mode," *IEEE Microwave and Wireless Components Letters*, vol. 15, pp. 597–599, Sept 2005.

[42] J. Nishizawa, P. Potka, T. Kurabayashi, and H. Makabe, "706-GHz GaAs CW fundamental-mode TUNNETT diodes fabricated with molecular layer epitaxy," *Physica Status Solidi(c)*, vol. 5, no. 9, pp. 2802–2804, 2008.

[43] J. P. Sun, G. Haddad, P. Mazumder, and J. Schulman, "Resonant tunneling diodes: models and properties," *Proceedings of the IEEE*, vol. 86, pp. 641–660, Apr 1998.

[44] M. Feiginov, C. Sydlo, O. Cojocari, and P. Meissner, "Resonant-tunnelling-diode oscillators operating at frequencies above 1.1THz," *Applied Physics Letters*, vol. 99, no. 23, 2011.

[45] M. Feiginov, H. Kanaya, S. Suzuki, and M. Asada, "1.46 THz RTD oscillators with strong back injection from collector," *39th International Conference on Infrared, Millimeter, and Terahertz Waves (IRMMW-THz)*, pp. 1–2, Sept 2014.

[46] T. Maekawa, H. Kanaya, S. Suzuki, and M. Asada, "Frequency increase in terahertz oscillation of resonant tunnelling diode up to 1.55 THz by reduced slot-antenna length," *Electronics Letters*, vol. 50, pp. 1214–1216, Aug 2014.

[47] J. Wang, K. Alharbi, A. Ofiare, H. Zhou, A. Khalid, D. Cumming, and E. Wasige, "High performance resonant tunneling diode oscillators for THz applications," *IEEE Compound Semiconductor IC Symposium*, October 2015.

[48] U. Pfeiffer and E. Ojefors, "A 600-GHz CMOS focal-plane array for terahertz imaging applications," *34th European Solid-State Circuits Conference (ESSCIRC)*, pp. 110–113, Sept 2008.

[49] R. Al Hadi, J. Grzyb, B. Heinemann, and U. Pfeiffer, "A terahertz detector array in a SiGe HBT technology," *IEEE Journal of Solid-State Circuits*, vol. 48, pp. 2002–2010, Sept 2013.

[50] K. Jacobs, N. Honingh, K. Jacobs, and N. Honingh, "Superconducting heterodyne detectors beyond 1 terahertz," *EAS Publications Series*, vol. 37, pp. 63–72, June 2009.

[51] X. Tu, L. Kang, X. Liu, Q. Mao, C. Wan, J. Chen, B. Jin, Z. Ji, W. Xu, and P. Wu, "Antenna-coupled microbolometer array for terahertz detection," *37th International Conference on Infrared, Millimeter, and Terahertz Waves (IRMMW-THz)*, pp. 1–1, Sept 2012.

[52] L. Fernandes, P. Kaufmann, R. Marcon, A. Kudaka, A. Marun, R. Godoy, E. Bortolucci, M. Zakia, and J. Diniz, "Photometry of THz radiation using golay cell detector," *XXXth URSI General Assembly and Scientific Symposium*, pp. 1–4, Aug 2011.

[53] J. Grzyb, H. Sherry, A. Cathelin, A. Kaiser, and U. Pfeiffer, "On the co-design between on-chip antennas and THz MOSFET direct detectors in CMOS technology," *37th International Conference on Infrared, Millimeter, and Terahertz Waves (IRMMW-THz)*, pp. 1–3, Sept 2012.

[54] E. Ojefors, U. Pfeiffer, A. Lisauskas, and H. Roskos, "A 0.65 THz focal-plane array in a quarter-micron CMOS process technology," *IEEE Journal of Solid-State Circuits*, vol. 44, pp. 1968–1976, July 2009.

[55] H. H. Truong Khang Nguyen, Thi Anh Ho and I. Park, "Numerical study of self-complementary antenna characteristics on substrate lenses at terahertz frequency," *Journal of Infrared, Millimeter, and Terahertz Waves*, vol. 33, pp. 1123–1137, July 2012.

[56] N. Llombart, C. Lee, M. Alonso-delPino, G. Chattopadhyay, C. Jung-Kubiak, L. Jofre, and I. Mehdi, "Silicon micromachined lens antenna for THz integrated heterodyne arrays," *IEEE Transactions on Terahertz Science and Technology*, vol. 3, pp. 515–523, Sept 2013.

[57] A. Neto, N. Llombart, J. Baselmans, A. Baryshev, and S. Yates, "THz leaky lens antenna integrated with kinetic inductance detectors," *International Workshop on Antenna Technology (iWAT)*, pp. 12–14, March 2013.

[58] X.-D. Deng, Y. Li, C. Liu, W. Wu, and Y.-Z. Xiong, "340 GHz on-chip 3-D antenna with 10 dBi gain and 80% radiation efficiency," *IEEE Transactions on Terahertz Science and Technology*, no. 99, pp. 1–9, 2015.

[59] W. Syed, G. Fiorentino, D. Cavallo, M. Spirito, P. Sarro, and A. Neto, "Design, fabrication, and measurements of a 0.3 THz on-chip double slot antenna enhanced by artificial dielectrics," *IEEE Transactions on Terahertz Science and Technology*, vol. 5, pp. 288–298, March 2015.

[60] E. R. Brown, A. W. M. Lee, B. S. Navi, and J. E. Bjarnason, "Characterization of a planar self-complementary square-spiral antenna in the THz region," *Microwave and Optical Technology Letters*, vol. 48, no. 3, pp. 524–529, 2006.

[61] L. Esaki, "New phenomenon in narrow germanium $p-n$ junctions," *Physical Review Letters*, vol. 109, pp. 603–604, Jan 1958.

[62] R. Tsu and L. Esaki, "Tunneling in a finite superlattice," *Applied Physics Letters*, vol. 22, no. 11, pp. 562–564, 1973.

[63] L. L. Chang, L. Esaki, and R. Tsu, "Resonant tunneling in semiconductor double barriers," *Applied Physics Letters*, vol. 24, no. 12, pp. 593–595, 1974.

[64] S. Sudirgo, D. Pawlik, S. Kurinec, P. Thompson, J. Daulton, S.-Y. Park, R. Yu, P. Berger, and S. Rommel, "NMOS/SiGe resonant interband tunneling diode static random access memory," *64th Device Research Conference*, pp. 265–266, June 2006.

[65] T. Oobo, R. Takemura, M. Suhara, Y. Miyamoto, and K. Furuya, "High peak-to-valley current ratio GaInAs/GaInP resonant tunneling diodes," *Japanese Journal of Applied Physics*, vol. 36, no. 8R, pp. 5079–5080, 1997.

[66] W. Wei, S. Hao, T. Teng, and S. Xiaowei, "High peak-to-valley current ratio $In_{0.53}Ga_{0.47}As$/AlAs resonant tunneling diode with a high doping emitter," *Journal of Semiconductors*, vol. 33, no. 12, pp. 124002–4, 2012.

[67] M. Oehme, D. Hhnel, J. Werner, M. Kaschel, O. Kirfel, E. Kasper, and J. Schulze, "Si esaki diodes with high peak to valley current ratios," *Applied Physics Letters*, vol. 95, no. 24, 2009.

[68] J. Wang, "Monolithic microwave/millimetrewave integrated circuit resonant tunnelling diode sources with around a milliwatt output power," *Ph.D. Thesis, University of Glasgow*, 2014.

[69] P. Nahin, "The science of radio: with matlab and electronics workbench demonstrations," *Springer-Verlag New York, Inc, 2nd edition*, pp. 83–94, 2001.

[70] C. Kim and A. Brandli, "High-frequency high-power operation of tunnel diodes," *IRE Transactions on Circuit Theory*, vol. 8, pp. 416–425, Dec 1961.

[71] L. Wang, "Reliable design of tunnel diode and resonant tunnelling diode based microwave and millimeterwave sources," *Ph.D. Thesis, University of Glasgow*, 2010.

[72] R. Hall, "Tunnel diodes," *IRE Transactions on Electron Devices*, vol. 7, pp. 1–9, Jan 1960.

[73] J. P. G.N. Roberts, "The design and construction of tunnel diodes," *Journal of the British Institution of Radio Engineers*, vol. 22, pp. 497–505(8), December 1961.

[74] K. K. Ng, "Complete guide to semiconductor devices," *John Wiley and Sons, Inc. Second edition*, 2002.

[75] T. A. Demassa and D. P. Knott, "The prediction of tunnel diode voltage-

current characteristics," *Solid-State Electronics*, vol. 13, no. 2, pp. 131 – 138, 1970.

[76] H. Mizuta and T. Tanoue, "The physics and applications of resonant tunnelling diodes," *Cambridge university press*, 1995.

[77] M. Adzhar, "Advanced $In_{0.8}Ga_{0.8}As/AlAs$ resonant tunneling diodes for applications in integrated mm-waves MMIC oscillators," *Ph.D. Thesis, University of Manchester*, 2015.

[78] M. Tsuchiya and H. Sakaki, "Dependence of resonant tunneling current on well widths in AlAs/GaAs/AlAs double barrier diode structures," *Applied Physics Letters*, vol. 49, no. 2, pp. 88–90, 1986.

[79] P. Roblin and H. Rohdin, "High-speed heterostructure devices: From device concept to circuit modeling," *Cambridge university press*, 2006.

[80] A. Seabaugh and R. Lake, "Tunnel diodes," *Encyclopedia of Applied Physics*, vol. 22, pp. 335–359, 1998.

[81] C. I. Huang, M. J. Paulus, C. A. Bozada, S. C. Dudley, K. R. Evans, C. E. Stutz, R. L. Jones, and M. E. Cheney, "AlGaAs/GaAs double barrier diodes with high peak-to-valley current ratio," *Applied Physics Letters*, vol. 51, no. 2, pp. 121–123, 1987.

[82] T. J. Shewchuk, P. C. Chapin, P. D. Coleman, W. Kopp, R. Fischer, and H. Morko, "Resonant tunneling oscillations in a GaAs/Al_xGa_{1-x}As heterostructure at room temperature," *Applied Physics Letters*, vol. 46, no. 5, pp. 508–510, 1985.

[83] J. Wang, L. Wang, C. Li, B. Romeira, and E. Wasige, "28 GHz MMIC reso-

nant tunnelling diode oscillator of around 1mW output power," *Electronics Letters*, vol. 49, pp. 816–818, June 2013.

[84] T. Inata, S. Muto, Y. Nakata, T. Fujii, H. Ohnishi, and S. Hiyamizu, "Excellent negative differential resistance of InAlAs/InGaAs resonant tunneling barrier structures grown by MBE," *Japanese Journal of Applied Physics*, vol. 25, no. 12A, p. L983.

[85] E. R. Brown, C. D. Parker, L. J. Mahoney, K. M. Molvar, and J. R. Soderstrom, "Oscillations up to 712 GHz in InAs/AlSb resonant-tunneling diodes," *Applied Physics Letters*, vol. 58, pp. 2291–2293, may 1991.

[86] M. Asada and S. Suzuki, "Compact THz oscillators with resonant tunneling diodes and application to high-capacity wireless communications," *21st International Conference on Applied Electromagnetics and Communications (ICECom)*, pp. 1–5, Oct 2013.

[87] http://www.ioffe.rssi.ru/SVA/NSM/Semicond/index.html, "Semiconductors on nsm, [1st august, 2015]," *Ioffe Institute*.

[88] S. M. Sze, "Physics of semiconductor devices," *Wiley-Interscience, 2nd Edition*, 1981.

[89] D. Paul, P. See, I. Zozoulenko, K.-F. Berggren, B. Hollnder, S. Mantl, N. Griffin, B. Coonan, G. Redmond, and G. Crean, "n-type Si/SiGe resonant tunnelling diodes," *Materials Science and Engineering: B*, vol. 89, no. 13, pp. 26 – 29, 2002.

[90] K. Wu, H. Cheng, K. Hung, and G. Sun, "Theoretical analysis of n-type Si-based resonant tunneling diodes deposited on either partially or fully relaxed SiGe buffer layers," *IEEE Transactions on Electron Devices*, vol. 60, pp. 1298–1301, April 2013.

[91] H. C. Liu, "Simulation of extrinsic bistability of resonant tunneling structures," *Applied Physics Letters*, vol. 53, no. 6, pp. 485–486, 1988.

[92] C. Y. Belhadj, K. P. Martin, S. Ben Amor, J. J. L. Rascol, R. J. Higgins, R. C. Potter, H. Hier, and E. Hempfling, "Bias circuit effects on the current-voltage characteristic of doublebarrier tunneling structures: Experimental and theoretical results," *Applied Physics Letters*, vol. 57, no. 1, pp. 58–60, 1990.

[93] J. F. Young, B. M. Wood, H. C. Liu, M. Buchanan, D. Landheer, A. J. SpringThorpe, and P. Mandeville, "Effect of circuit oscillations on the dc currentvoltage characteristics of double barrier resonant tunneling structures," *Applied Physics Letters*, vol. 52, no. 17, pp. 1398–1400, 1988.

[94] N. Jin, S.-Y. Chung, R. Yu, S. Di Giacomo, P. R. Berger, and P. E. Thompson, "RF performance and modeling of Si/SiGe resonant interband tunneling diodes," *IEEE Transactions on Electron Devices*, vol. 52, pp. 2129–2135, Oct 2005.

[95] M. Bao and K. Wang, "Accurately measuring current-voltage characteristics of tunnel diodes," *IEEE Transactions on Electron Devices*, vol. 53, pp. 2564–2568, Oct 2006.

[96] L. Wang, J. Figueiredo, C. Ironside, and E. Wasige, "Dc characterization of tunnel diodes under stable non-oscillatory circuit conditions," *IEEE Transactions on Electron Devices*, vol. 58, pp. 343–347, Feb 2011.

[97] M. Reddy, R. Yu, H. Kroemer, M. Rodwell, S. Martin, R. Muller, and R. Smith, "Bias stabilization for resonant tunnel diode oscillators," *IEEE Microwave and Guided Wave Letters*, vol. 5, pp. 219–221, Jul 1995.

[98] J. Wallmark and A. Dansky, "Nonlinear biasing resistors for microwave tunnel-diode oscillators," *IEEE Transactions on Microwave Theory and Techniques*, vol. 11, no. 4, pp. 260–262, 1963.

[99] L. Davidson, "Optimum stability criterion for tunnel diodes shunted by resistance and capacitance," *Proceedings of the IEEE*, vol. 51, pp. 1233–1233, Sept 1963.

[100] R. Driad, M. Krieg, N. Geldmacher, J. Ruster, and F. Benkhelifa, "Investigation of nicr thin film resistors for InP-based monolithic microwave integrated circuits (MMICs)," *Journal of The Electrochemical Society*, vol. 158, no. 5, pp. 561–564, 2011.

[101] S. Horst, S. Bhattacharya, S. Johnston, M. Tentzeris, and J. Papapolymerou, "Modeling and characterization of thin film broadband resistors on LCP for RF applications," *Proceedings of the 56th Electronic Components and Technology Conference*, pp. 1751–1755, 2006.

[102] E. Bloch, D. Mistele, R. Brener, C. Cytermann, A. Gavrilov, and D. Ritter, "NiCr thin film resistor integration with InP technology," *Semiconductor Science and Technology*, vol. 26, no. 10, p. 105004, 2011.

[103] http://www.rf-microwave.com/datasheets/4939 generic 1N3717 01.pdf, "Tunnel diode data sheet, [1 march, 2016],"

[104] http://www.americanmicrosemi.com/information/spec/ss pn 1n3712, "Tunnel diode data sheet, [1 march, 2016],"

[105] Y. Guo, X. Wei, J. Shu, B. Liu, J. Yin, C. Guan, Y. Han, S. Gao, and Q. Chen, "Charge trapping at the MoS2-SiO2 interface and its effects on the characteristics of MoS2 metal-oxide-semiconductor field effect transistors," *Applied Physics Letters*, vol. 106, no. 10, 2015.

[106] A. Zhao, C. D. Young, R. Choi, and B. H. Lee, "Pulsed characterization of charge-trapping behavior in high-k gate dielectrics," *www.Keithley.co.uk/data*, 2006.

[107] C. Baylis and L. Dunleavy, "Understanding pulsed IV measurement waveforms," *The 11th IEEE International Symposium on Electron Devices for Microwave and Optoelectronic Applications*, pp. 223–228, Nov 2003.

[108] http://cp.literature.agilent.com/litweb/pdf/B1530 90000.pdf, "Agilent B1530A Waveform Generator/Fast Measurement Unit-User's Guide [May, 2015],"

[109] A. Ofiare, A. Khalid, J. Wang, and E. Wasige, "Pulsed i-v and small signal characterisation and modelling of resonant tunneling diodes," *IEEE PhD Research in Microelectronics and Electronics (PRIME) Conference*, vol. 10, pp. 286–289, June 2015.

[110] J. N. Schulman, H. J. de Los Santos, and D. H. Chow, "Physics-based RTD current-voltage equation," *IEEE Electron Device Letters*, vol. 17, pp. 220–222, may 1996.

[111] P. Fay, J. Lu, Y. Xu, N. Dame, D. Chow, and J. Schulman, "Microwave performance and modeling of InAs/AlSb/GaSb resonant interband tunneling diodes," *IEEE Transactions on Electron Devices*, vol. 49, pp. 19–24, Jan 2002.

[112] S.-Y. Chung, R. Yu, N. Jin, S.-Y. Park, P. R. Berger, and P. Thompson, "Si/SiGe resonant interband tunnel diode with f_{r0} 20.2 GHz and peak current density 218 kA/cm2 for K-band mixed-signal applications," *IEEE Electron Device Letters*, vol. 27, pp. 364–367, May 2006.

[113] D. L. Woolard, F. A. Buot, D. L. Rhodes, X. J. Lu, R. A. Lux, and B. S. Perlman, "On the different physical roles of hysteresis and intrinsic oscillations in resonant tunneling structures," *Journal of Applied Physics*, vol. 79, no. 3, pp. 1515–1525, 1996.

[114] F. A. Buot and K. L. Jensen, "Intrinsic high-frequency oscillation and equivalent circuit model in the negative differntial resistance region of resonant tunneling devices," *The International Journal for Computational and Mathematics in Electrical and Electronic Engineering*, vol. 10, no. 4, pp. 241–253, 1991.

[115] J. M. Gering, D. A. Crim, D. G. Morgan, P. D. Coleman, W. Kopp, and H. Morko, "A small-signal equivalent circuit model for gaas-alxga1xas resonant tunneling heterostructures at microwave frequencies," *Journal of Applied Physics*, vol. 61, no. 1, pp. 271–276, 1987.

[116] E. R. Brown, C. D. Parker, and T. C. L. G. Sollner, "Effect of quasibound state lifetime on the oscillation power of resonant tunneling diodes," *Applied Physics Letters*, vol. 54, no. 10, pp. 934–936, 1989.

[117] T. Wei, S. Stapleton, and E. Berolo, "Equivalent circuit and capacitance of double barrier resonant tunneling diode," *Journal of Applied Physics*, vol. 73, no. 2, pp. 829–834, 1993.

[118] http://www.cascademicrotech.com/blog/2011/choosing-the-optimal-two-port-calibration method, "Choosing the Optimal Two-Port Calibration Method,[june, 2015],"

[119] M. Koolen, J. Geelen, and M. Versleijen, "An improved de-embedding technique for on-wafer high-frequency characterization," *Proceedings of the Bipolar Circuits and Technology Meeting*, pp. 188–191, Sep 1991.

[120] http://cp.literature.agilent.com/litweb/pdf/ads2008/optstat/ads2008/Summary of Optimizers.html, "Summary of optimizers, [june, 2015],"

[121] R. Miles, G. Millington, R. Pollard, D. Steenson, J. Chamberlain, and M. Henini, "Accurate equivalent circuit model of resonant tunnelling diodes," *Electronics Letters*, vol. 27, pp. 427–428, Feb 1991.

[122] T. Wei, S. Stapleton, and O. Berolo, "Scattering parameter measurements of resonant tunneling diodes up to 40 ghz," *IEEE Transactions on Electron Devices*, vol. 42, pp. 1378–1380, July 1995.

[123] C. Kidner, I. Mehdi, J. R. East, and G. I. Haddad, "Bias circuit instabilities and their effect on the DC current-voltage characteristics of double-barrier resonant tunneling diodes," *Solid-State Electronics*, vol. 34, pp. 149–156, Feb 1991.

[124] S. S. M. Asada and N. Kishimoto, "Resonant tunnelling diodes for sub-terahertz and terahertz oscillators," *Japanese Journal of Applied Physics*, vol. 47, no. 6, pp. 4375–4384, 2008.

[125] A. Ofiare, J. Wang, K. Alharbi, A. Khalid, E. Wasige, and L. Wang, "Novel tunnel diode oscillator power combining circuit topology based on synchro-nisation," *Asia Pacific Microwave Conference (APMC)*, vol. 3, pp. 1–3, December 2015.

[126] D. M. Pozar, "Microwave engineering," *John Wiley and sons, Inc. 2nd Edition*, 1998.

[127] http://www.datasheets360.com/pdf/ 1977714464416072863, "Germanium power devices corp. tunnel diodes specifications, [12 november, 2015],"

[128] Hewlett and Packard, "Phase noise characterisation of microwave oscillators," *HP Product Note 11729C-2*.

[129] D. Scherer, "The 'Art' of Phase Noise Measurements," *HP RF Microwave Symposium*, October 1984.

[130] D. Titz, F. Ferrero, C. Luxey, P. Brachat, and G. Jacquemod, "Radiation pattern characterization of antennas at millimeter-wave frequencies," *IEEE International Workshop on Antenna Technology (iWAT)*, pp. 311–314, 2012.

[131] J. D. Kraus, "Antennas," *McGraw-Hill Book Company*, 1950.

[132] C. A. Balanis, "Antenna theory: Analysis and design," *John Wiley and Sons, Inc*, 1982.

[133] S. Uda, "On the wireless beam of short electric waves," *Journal of the Institute of electrical engineers of Japan*, 1927.

[134] W. Deal, N. Kaneda, J. Sor, Y. Qian, and T. Itoh, "A new quasi-Yagi antenna for planar active antenna arrays," *IEEE Transactions on Microwave Theory and Techniques*, vol. 48, no. 6, pp. 910–918, 2000.

[135] Y. Sun, H. Zhang, G. Wen, and P. Wang, "Research progress in Yagi antennas," *Procedia Engineering: International Workshop on Information and Electronics Engineering*, vol. 29, pp. 2116–2121, 2012.

[136] H. Kan, R. Waterhouse, A. Abbosh, and M. Bialkowski, "Simple broadband planar CPW-fed quasi-Yagi antenna," *IEEE Antennas and Wireless Propagation Letters*, vol. 6, pp. 18–20, 2007.

[137] J. Sor, Y. Qian, and T. Itoh, "Coplanar waveguide fed quasi-Yagi antenna," *Electronics Letters*, vol. 36, pp. 1–2, Jan 2000.

[138] G. Zheng, A. Kishk, A. Glisson, and A. Yakovlev, "Simplified feed for modified printed Yagi antenna," *Electronics Letters*, vol. 40, pp. 464–466, April 2004.

[139] A. Yusuf, "Design and fabrication of a thz planar yagi-uda antenna," *MSc Poster Session*, 2014.

[140] A. Ofiare, K. Alharbi, A. Khalid, J. Wang, D. Cumming, and E. Wasige, "Wideband planar Yagi antennas for millimetre wave frequency applications," *7 th European/UK-China Workshop on Millimeter Waves and Terahertz Technologies (UCMMT)*, 2014.

[141] K. Alharbi, A. Ofiare, J. Wang, A. Khalid, D. Cumming, and E. Wasige, "Radiation pattern characterisation setup for G-band planar Yagi antennas," *2nd IET Annual Active and Passive RF Devices Seminar*, pp. 1–3, Oct 2014.

[142] S. Lim and H. Ling, "Design of a planar, closely spaced yagi antenna," *Antennas and Propagation Society International Symposium*, pp. 5997–6000, June 2007.

[143] J. Laskar, S. Chakraborty, F. Bien, M. Tanzeris, and A. Pham, "Advanced integrated communication micosystems," *John Wiley and Sons, Inc.*, 2009.

[144] A. Ofiare, K. Alharbi, J. Wang, A. Khalid, D. Cumming, and E. Wasige, "Wideband planar yagi antenna for millimetre-wave frequency applications," *European/UK-China Workshop on Millimeter Waves and Terahertz Technologies (UCMMT)*, October 2014.

[145] www.omlinc.com/images/pdf/Library/ApplicationNotes/41130823HowtoI MD.pdf, "How to imd, [30 september, 2015],"

[146] http://www.ansys.com/staticassets/ANSYS/staticassets/resourcelibrary/ techbrief/abansyshfssforantennasimulation.pdf, "ANSYS HFSS for antenna simulation, [1 december, 2015],"

[147] http://www.ansys.com/Products/SimulationTechnology/Electronics/Sign alIntegrity/ANSYSHFSS, "Ansys hfss, [25 september, 2015],"

[148] http://glendash.com/DashofEMC/AnechoicChambers/AnechoicChambers .pdf, "Anechoic chambers, [july, 2015],"

[149] Y. Huang and K. Boyle, "Antennas: From theory to practice," *John Wiley and Sons, Inc. 1st Edition*, 2008.

[150] http://www.ets lindgren.com/all/EHPMicrowaveAbsorber, "Microwave pyramidal absorber, [1 march, 2016],"

[151] S. Beer and T. Zwick, "Probe based radiation pattern measurements for highly integrated millimeter-wave antennas," *Proceedings of the Fourth European Conference on Antennas and Propagation (EuCAP)*, pp. 1–5, April 2010.

[152] A. Bisognin, D. Titz, F. Ferrero, G. Jacquemod, R. Pilard, F. Gianesello, D. Gloria, C. Laporte, H. Ezzeddine, D. Lugara, and C. Luxey, "Probe-fed measurement system for f-band antennas," *Proceedings of the 8th European Conference on Antennas and Propagation (EuCAP)*, pp. 722–726, April 2014.

[153] D. Titz, M. Kyr, F. Ferrero, S. Ranvier, C. Luxey, P. Brachat, G. Jacquemod, and P. Vainikainen, "Measurement setup and associated calibration methodology for 3d radiation pattern of probe-fed millimeter-wave antennas," *Antennas and Propagation Conference (LAPC)*, pp. 1–5, Nov 2011.

[154] S. Ranvier, M. Kyr, C. Icheln, C. Luxey, R. Staraj, and P. Vainikainen, "Compact 3-D on-wafer radiation pattern measurement system for 60 GHz antennas," *Microwave and Optical Technology Letters*, vol. 51, no. 2, pp. 319–324, 2009.

[155] K. Fujii, T. Tosaka, Y. Matsumoto, and A. Kasamatsu, "Calibration of standard gain horn antennas in the frequency range from 220 to 325 GHz," *38th International Conference on Infrared, Millimeter, and Terahertz Waves (IRMMW-THz)*, pp. 1–2, Sept 2013.

[156] T. C. L. G. Sollner, W. D. Goodhue, P. E. Tannenwald, C. D. Parker, and D. D. Peck, "Resonant tunneling through quantum wells at frequencies up to 2.5 THz," *Applied Physics Letters*, vol. 43, no. 6, pp. 588–590, 1983.

[157] http://uk.mathworks.com/help/optim/ug/lsqnonlin.html, "lsqnonlin, [august, 2015],"

[158] E. Kreyszig, "Advanced engineering mathematics," *John Wiley and Sons, Inc. 9th Edition*, 2006.

[159] R. Collin, "Foundations for microwave engineering," *IEEE Press Series on Electromagnetic Wave Theory, 2nd Edition*, 2001.

[160] http://www.maxwells equations.com/, "Maxwell's equations, [25 september, 2015],"

[161] A. Taflove and S. C. Hagness, "Computational electrodynamics: The finite-difference time domain method," *Artech House, Inc. 3rd Edition*, 2005.